SCUOLA DI DOTTORATO
UNIVERSITÀ DEGLI STUDI DI MILANO-BICOCCA

Dipartimento di Fisica

Dottorato di Ricerca in Fisica e Astronomia Ciclo XXIX

Cosmological measurements and models of galaxy clustering and redshift-space distortions using galaxy redshift surveys

Cognome : Pezzotta

Nome : Andrea

Matricola 718224

Supervisore : Prof. Luigi Guzzo

Tutore : Dott. Benjamin R. Granett

ANNO ACCADEMICO 2016/2017

Contents

Abstract

One of the major achievements of observational cosmology in the 20th century has been the detailed reconstruction of the large-scale structure of what is now called the *local Universe* ($z \leq 0.2$). This has been possible thanks to collection of huge redshift samples, such as the ones provided by the SDSS (York et al. 2000; Abazajian et al. 2009) and the 2dFGRS (Colless et al. 2001, 2003).

Galaxy clustering on large scales is one of the most important relics of the initial conditions that shaped our Universe, and the observed shape of the power spectrum $P(k)$ of density fluctuations [or of its Fourier transform, the correlation function $\xi(r)$] indicates that we live in a low-density Universe in which only $\sim 30\%$ of the mass-energy density is provided by (mostly dark) matter.

Observations of Type Ia Supernovae (Riess et al. 1998; Perlmutter et al. 1999) combined with the anisotropies of the Cosmic Microwave Background (Efstathiou et al. 1990) have reinforced the conclusion that the remaining 70% of the energetic component is dominated by a repulsive *dark energy* capable of driving the observed accelerated expansion. Unfortunately this scenario is highly degenerate with the more radical breakdown of General Relativity on cosmological scales; in this case, for a precise choice of parameters, modified gravity is able to predict the same expansion history $H(z)$ as for a ΛCDM (dark energy + GR).

In principle, this degeneracy can be lifted by measuring the growth rate of structure, which depends on the specific theory describing gravity. One of the most reliable probe for the growth of structures are *redshift-space distortions* (Kaiser 1987). These arise when measured redshifts are used as distance proxy, since they contain also the contribution of galaxy peculiar velocities, that in turn, are directly correlated to gravity. The anisotropy of statistical measurements like the two-point correlation function is proportional to the growth rate of cosmic structure $f(z)$, which is a trademark of the gravity theory: if GR holds, we expect to measure a growth rate $f(z) = [\Omega_m(z)]^{0.55}$ (Peebles 1980; Lahav et al. 1991); otherwise different forms are predicted (see

e.g. Dvali et al. 2000; Linder & Cahn 2007).

Unfortunately, extracting the linear RSD signal from galaxy redshift surveys is non-trivial, because much of the RSD signal lies on quasi-linear and non-linear scales. A simple and widely-used extension of the linear Kaiser model is the *dispersion model* (Peacock & Dodds 1994), which accounts for radial convolution by a random velocity dispersion plus non-linear corrections to the real-space power spectrum. This model was successfully applied to several galaxy surveys in the past (Peacock et al. 2001; Guzzo et al. 2008), but is insufficiently accurate to be trusted when the precision allowed by the data goes below 10% (Okumura & Jing 2011; Bianchi et al. 2012; Wilson et al. 2017). There have been a number of attempts to derive improved RSD models. As shown by Scoccimarro (2004), the dispersion model is a simplification of the original *streaming model* (Peebles 1980; Fisher 1995), in which the full redshift-space correlation function is obtained by convolution with a proper scale-dependent pairwise velocity distribution. But predicting this distribution function is hard (e.g. Bianchi et al. 2015b; Uhlemann et al. 2015), and typical applications simplify the problem by adopting a (scale-dependent) Gaussian pairwise distribution function (e.g. Reid et al. 2012). Scoccimarro (2004) proposed an influential alternative, in which the linear Kaiser term is generalised by including the velocity and velocity-density power spectra. This concept was extended by the TNS model (Taruya et al. 2010), which takes better into account the non-linear coupling between the density and the velocity field. This model is currently considered as one of the best descriptions of RSD down to the quasi-linear regime.

In this work we present measurements of the growth rate of cosmological structure from the modelling of the anisotropic galaxy clustering measured in the final data release of the VIPERS survey. The survey has collected about 100000 redshifts of multiple sources (galaxies and AGNs) over an incredibly extended redshift range, $0.4 < z < 1.2$, probing the clustering of galaxies down to an age when the Universe was only half of its current age.

The analysis is carried out in configuration space and based on measurements of the first two even multipole moments of the anisotropic galaxy autocorrelation function, in two redshift bins spanning the range $0.5 < z < 0.7$ and $0.7 < z < 1.2$. We provide robust and cosmology-independent corrections for the VIPERS angular selection function, allowing recovery of the underlying clustering amplitude at the percent level down to the Mpc scale. In detail, we derive appropriate angular weights that have to be applied to each target in order to provide an unbiased measurement of both monopole and quadrupole over the separation range that we use later in the fit of the growth rate.

On a more theoretical ground, we discuss several improvements on the

non-linear modelling of redshift-space distortions (RSD) and perform detailed tests of a variety of approaches against a set of realistic VIPERS-like mock realisations (we test on them the previously describe RSD models). This includes using novel fitting functions to describe the velocity divergence and density power spectra $P_{\theta\theta}$ and $P_{\delta\theta}$ that appear in RSD models. These tests show that we are able to measure the growth rate with negligible bias down to separations of $5\,h^{-1}$Mpc. Interestingly, the application to real data shows a weaker sensitivity to the details of non-linear RSD corrections compared to mock results.

We obtain consistent values for the growth rate times the matter power spectrum normalisation parameter of $f\sigma_8 = 0.55 \pm 0.12$ and 0.40 ± 0.11 at effective redshifts of $z = 0.60$ and $z = 0.86$ respectively. Independent measurements of the same quantity exploiting different cosmological probes all provide a coherent value of $f\sigma_8$, with a deviation that is less than 1-σ from the value obtained in this work. All these results are in agreement with standard cosmology predictions assuming Einstein gravity in a ΛCDM background. At the same time, they do not exclude a variety of cosmological models assuming the modification of gravity on cosmic scales. The full potential of RSD in constraining the underlying cosmological model will be achievable only with next-generation galaxy surveys, that will collect redshift catalogues one order of magnitude larger than current ones.

Chapter 1

INTRODUCTION

1.1 Cosmology: some basic concepts

Cosmology is that branch of physical astronomy that deals with the origin, the evolution and the ultimate fate of the Universe. It also takes over the theory of the large-scale structure and the dynamics of the Universe we live in. In this sense, it is essential not to confuse this discipline with astrophysics, since the latter is mainly interested in the physical processes contributing to the birth and evolution of isolated objects, like stars, galaxies and eventually clusters of galaxies.

Cosmology is based upon the so-called *cosmological principle*, according to which the distribution of matter in the Universe is homogeneous and isotropic above an approximated scale of 150 Mpc. This notion comes out quite intuitively, given that the four fundamental interactions (electromagnetic, nuclear, weak and gravitational) are expected to act uniformly throughout the space-time, producing no observable irregularities in its geometrical configuration, when smoothed on sufficiently large scales. A first version of the cosmological principle can be found inside the work by Isaac Newton, *Philosopiæ Naturalis Principia Mathematica* (1687), in which for one of the first time in history, Earth is no longer considered to rest at the center of the Universe, but is rather dislocated in a perfectly random position of the Universe.

As a matter of fact, the birth of modern astronomy dates back to the the 16th century, when mathematicians and astronomers like Copernicus, Galileo, Kepler and Newton himself set the stage for further studies on the morphology and the dynamics of the solar system. Nevertheless, it is just from the twentieth century that we shall talk about cosmology as the investigation of the Universe as a whole. Indeed, this period was marked by the

rapid enhancement of astronomical instrumentation for direct sky observation, and this allowed the first large collections of galaxy spectra and images, leading to improved astronomical and cosmological analysis. At the same time, the conception of the new revolutionary theory of gravity by Einstein (*General Relativity*) pushed the development of self-consistent models for the structure of the Universe also on a theoretical ground.

The fundamental breakthrough occurred in 1929, after the conclusion of the Great Debate concerning the dimension of the Milky Way and the nature of nebular objects. Using galaxy redshifts and supernovae Ia respectively as proxies for their velocities and radial distances, Hubble showed that galaxies are following a recessional motion, which is caused by the expansion of the Universe itself (Hubble 1936, 1937). Furthermore, the recessional velocities v of galaxies are linearly related (see Figure 1.1) to their distances r from us via the well-known Hubble's law,

$$v = H_0\, r, \tag{1.1}$$

where, in time, the numerical constant H_0 has assumed the name of *Hubble constant*. Something that must be closely kept in mind is that this relation holds true only within the local Universe, in the limit of $z \ll 1$. At higher redshifts, different cosmological models predict different trends for the shape of this relation (see Hogg (1999) for some reviews on the distance-redshift relation). In any case, the Hubble's law has to be regarded as one of the most important discovery ever made in cosmological ground, marking the beginning of modern observational cosmology throughout the whole century. Not only, it has also thrown the basis for the development of models about the evolution of an expanding fluid slowed down by its self-gravity, something that finds its full expression in the renowned Friedmann equations (Friedmann 1922, 1924).

Motivations for an expanding Universe were easily provided by a Hot Big Bang scenario (Alpher & Herman 1988; Weinberg 1993). According to this theory, the earliest stages of life of the Universe are characterised by an extremely hot and dense fluid made up by radiation and matter, the latter basically consisting of free elementary particles like protons, neutrons and electrons. These conditions are ideal for the establishment of a cosmological nucleosynthesis, that can trigger the production of heavier nuclei to some extent. Eventually, the primordial fluid cools down because of the expansion of the Universe and in this mechanism, two important period can be highlighted: the epoch of equivalence, when the matter and radiation energy densities are comparable, and the epoch of recombination, when photons decouple from matter and the Universe become neutral.

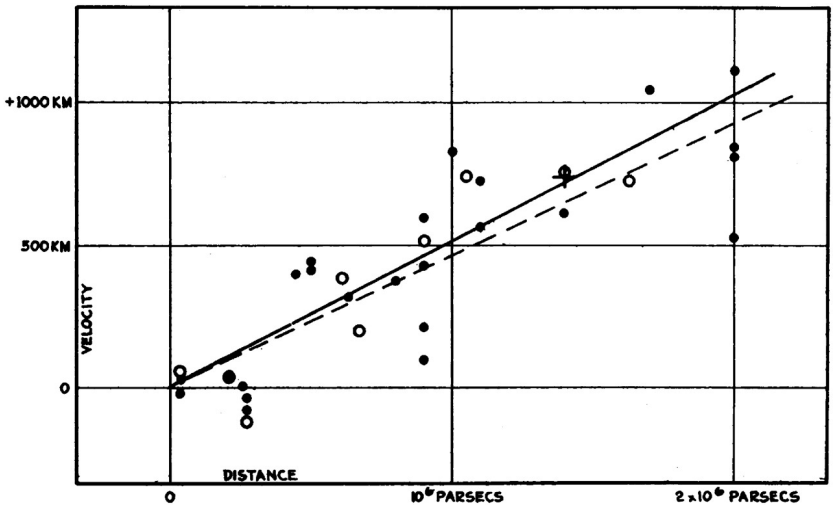

Figure 1.1: Original galaxy velocity-distance relation firstly obtained in Hubble (1929). Radial velocities, corrected for solar motion, are plotted against distances estimated from involved stars and mean luminosities of nebulae in a cluster. The black discs and full line represent the solution for solar motion using the nebulae individually; the circles and broken line represent the solution combining the nebulae into groups; the cross represents the mean velocity corresponding to the mean distance of 22 nebulae whose distances could not be estimated individually.

In contrast with the Hot Big Bang theory, cosmologists like Hoyle, Bond and Gold proposed an alternative scenario, that has become known as Steady State model (Bondi & Gold 1948; Hoyle 1948). The latter is based on an extension of the cosmological principle (the perfect cosmological principle). This extension asserts that although the Universe is undergoing a phase of expansion, its appearance remains constant over time. The last sentence can be recast saying that there is no privileged position in space but also in time (and this goes against the leading assumption of the Big Bang theory). This requires that matter be continually created in order to keep the density of the Universe constant over time.

While the Steady State enjoyed some popularity during the mid-20th century, it was almost completely rejected in 1964, with the discovery by Penzias and Wilson of the Cosmic Microwave Background (Penzias & Wilson 1965). The CMB was soon recognised as the relic of the primordial photon fluid permeating the Universe since its very early origins. This radiation - characterised by a black-body spectrum at a temperature $T_{\rm CMB} \sim 2.725$K - finds a quick explanation if we assume a Hot Big Bang model for the thermal history of the Universe.

A concept already established at the time was that of dark matter. This non-baryonic component was initially suggested in 1932, independently by

(Oort 1932) and Zwicky (1933), in the light of discrepancies between the mass of large astronomical objects as determined from their gravitational effects, and their luminous matter (stars, gas, and dust). Subsequently, many other observations indicated the presence of dark matter in the Universe, including galaxy rotation curves, gravitational lensing of background objects by galaxy clusters, the temperature distribution of hot gas in galaxies and clusters of galaxies and, more recently, the pattern of anisotropies in the cosmic microwave background (Hinshaw et al. 2012; Planck Collaboration et al. 2015). The existence of dark matter is of extreme importance, since it contributes to almost 90% of the total matter energy density. Models for the description and the evolution of the large-scale structure, that do not account for this contribution, are necessarily intended to fail in reproducing the current spatial distribution of matter across the Universe. For this reason, the struggling search for a particle embodying the global properties of this component has become one of the major efforts in particle physics today.

In 1998, published observations of Type Ia supernovae suggested that the expansion of the Universe is accelerating, a discovery that awarded with the 2011 Nobel Prize in Physics the leaders of this project (Riess et al. 1998; Perlmutter et al. 1999). The most accepted theory able to explain these observations is that the Universe is permeated by an unknown form of energy, usually referred to as dark energy, that tends to accelerate the expansion of the Universe itself. The best current measurements indicate that dark energy contributes to most of the total energy density ($\sim 69\%$), with dark and luminous matter representing only a very small fraction of the total mass-energy in the Universe (respectively $\sim 27\%$ and $\sim 4\%$). In its simplest realisation, dark energy assumes the features of the so-called *cosmological constant*, a constant energy density permeating space homogeneously, that can be related to the energy of void (see e.g. Weinberg et al. (2013) for some history and a review of current constraints). The use of this constant was first employed by Einstein to justify the idea of a static Universe, prior to direct evidences of an expanding Universe provided by Hubble observations in the local Universe. However, the original idea of Einstein was that this constant should have speeded up the expansion rather than stopping it. An alternative realisation of dark energy is the one generated starting from a space-time filling scalar field such as quintessence, a dynamic quantity whose energy density can vary in time and space.

Although this simple idea, of having an additional component to the fluid that permeates the cosmos, provides extremely positive results when compared to observations, the accelerated expansion can be justified also invoking a modification of General Relativity on cosmological scales (Carroll et al. 2004; Jain & Khoury 2010; Clifton 2011). This has led to the

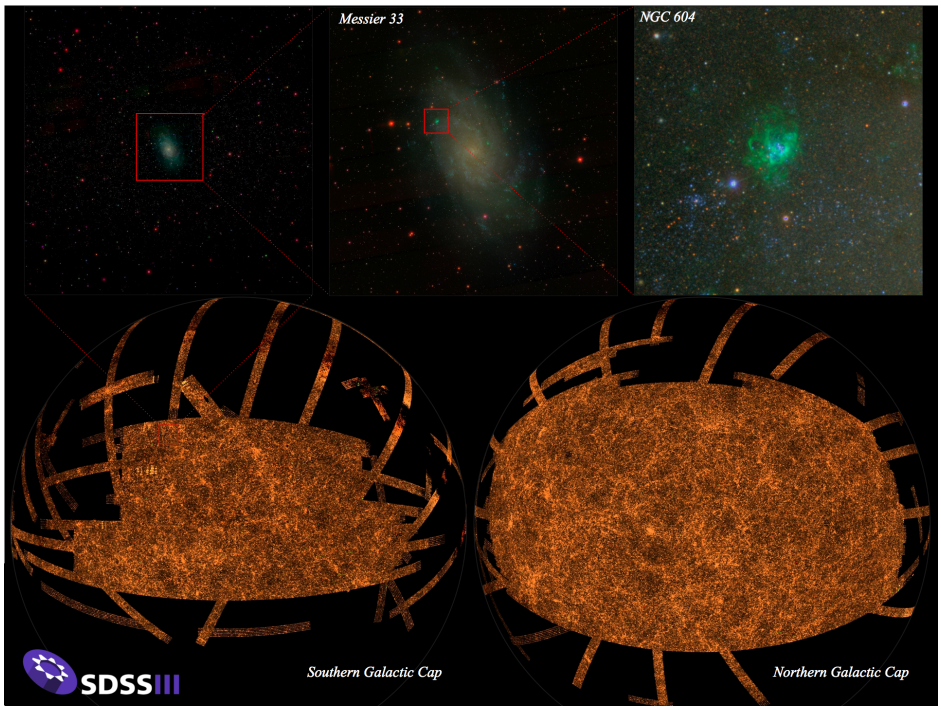

Figure 1.2: Picture of the ongoing mapping of the local Universe made by the Sloan Digital Sky Survey. SDSS imaging has covered slightly more than 1/3 of the sky divided in the northern and southern galactic cup. It is important to emphasize the high resolution of the instruments used for this project, which has carried out the most detailed digital pictures ever made. For instance, the sequence of zoom in the upper panel shows the star forming nebula NGC604 in the nearby galaxy M33.

birth of a full branch of different gravitational theories, the most renowned of, $f(R)$ gravity and brane world cosmologies such as the one proposed by Dvali, Gabadadze and Porrati (DGP). More recently, Guzzo et al. (2008) and Zhang et al. (2007) have independently pointed out that the degeneracy between dark energy and modified gravity could be lifted exploiting clustering measurements from large redshift surveys. Indeed, the patches and filamentary structures formed by galaxies in the Universe (the cosmic web) represent a direct probe of the underlying model of gravity, and a precise measurement of the rate at which structures grow in time will eventually make a particular theory of gravity to triumph over different models.

In the last decades, the need for accurate and precise measurements of the spatial distribution of matter in the Universe has pushed the improvement of astronomical instrumentation and the realisation of huge redshift surveys. These programmes have collected samples of hundreds of thousands redshifts, with the goal of mapping the large scale distribution of galaxies up to very

high redshifts. This has been well-achieved in the local Universe (see Figure 1.2) by the solid and continuous work of many galaxy surveys such as the Sloan Digital Sky Survey (SDSS) and the 2-degree Field Galaxy Redshift Survey (2dFGRS). Next-generation surveys, like Euclid and the Dark Energy Spectroscopic Instrument (DESI) are designed to collect sample of millions of redshifts, and represent an important step in understanding the nature of the cosmos and the properties of the elements that fill our Universe. Indeed, with modern telescopes (e.g. HST, Keck telescopes), we can target objects out to redshifts beyond 6, making it possible for us to probe the galaxy population back to a time when the Universe was only about 10% of its current age.

1.2 Phenomenology of galaxies

The most relevant luminous tracers of the dark matter density field, its structure and its evolution in time, are galaxies. Galaxies are dynamically bound systems, made up by stars, stellar remnants, an interstellar medium composed of gas and dust, and are surrounded by halos of non-baryonic matter. In this sense, galaxies are well-defined objects, since almost each star in the Universe belongs to a galactic system, the dimension of these structures being several hundred time smaller than their mean intergalactic separation (see Mo et al. (2010) for a detailed review on galaxy morphology and evolution).

The galaxy population is definitely various, ranging widely both in sizes and morphologies. Pointing a telescope towards the night sky, one can recognise bright objects like the Milky Way, containing up to 10^{12} stars and reaching linear dimensions of about 20 Kpc, in contrast with irregular dwarf galaxies that are about 10^3 times smaller. In any case, one of the most useful criterion to divide galaxies in morphological classes is based on the tuning fork diagram (see Figure 1.4), a classification scheme proposed by Hubble in 1926. Galaxies comes essentially in two different flavours:

1) **Elliptical galaxies** They show an elliptical appearance, mainly due to a smooth featureless light profiles. The dynamics in the internal region of these structures is mainly supported by random motions of stars around the common center of mass. Elliptical systems have a poor amount of interstellar medium, and thus do not have much fuel for star formation processes. Their colour is typically red. In the Hubble diagram, these objects are denoted with the letter "E" followed by an integer representing the degree of ellipticity. Given their position in the tuning fork, they are referred to as *early type* galaxies. A picture of IC2006, a giant elliptical galaxy, can be found in the right panel of Figure 1.3.

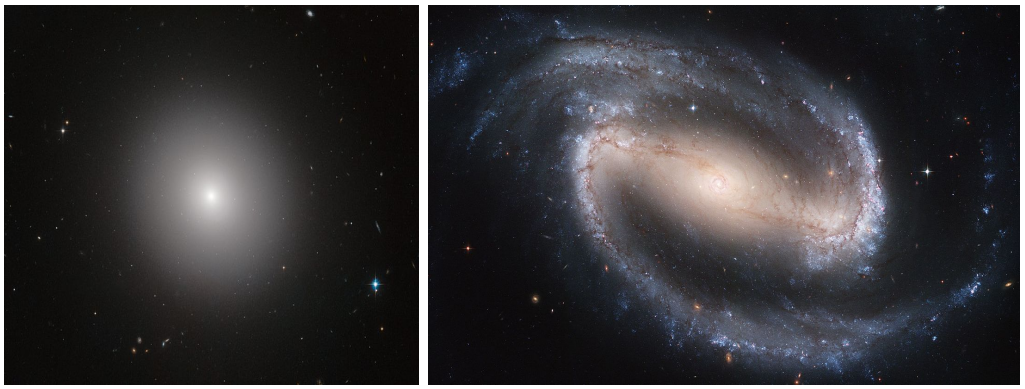

Figure 1.3: On the left: giant elliptical galaxy IC2006, still located in the constellation Eridanus. On the right: barred spiral galaxy NGC1300 (classified as SBbc), located in the constellation Eridanus, about 61 million light years from the Milky Way.

2) **Spiral galaxies** They present flattened discs, with an almost spherical inner region called *bulge*, and their light distribution is well-represented by an exponential profile. Starting from the outer regions of the bulge, a spiral pattern branches off across the area occupied by the disk. Here, the large amount of atomic hydrogen HI is responsible for driving an intense star formation. They usually come with blue colours. Spiral galaxies are further subdivided in two different branches, according to whether the spiral arms start from the spherical bulge or a barred structure. These classes are represented with the letters "S/Sb", followed by another letter describing the degree of aperture of the spiral arms and the relative dimension of the bulge with respect to the disk. They are commonly referred to as "late type" galaxies. A picture of NGC1300, a barred spiral galaxy, can be found in the left panel of Figure 1.3.

It is important to stress how this subdivision is not complete, since there exist galaxies that cannot be put so easily in one of these two categories. The most remarkable example is the one of lenticular galaxies, that exhibits a disc shape with no spiral arms, and that can be regarded as the linking class between spirals and ellipticals. Moreover, irregular dwarf galaxies are hard to be inserted in any of the described categories as they do not show any precise feature that could help in their classification. With the accomplishment of new standards in the modern imaging techniques, the Hubble tuning fork has been partially put aside, as astronomers have developed improved selection criteria, based on more quantitative analysis that leave less freedom to human interpretation.

As anticipated in the previous section, the real interest of cosmologists in galaxies is that their spatial distribution must in some way follow the one

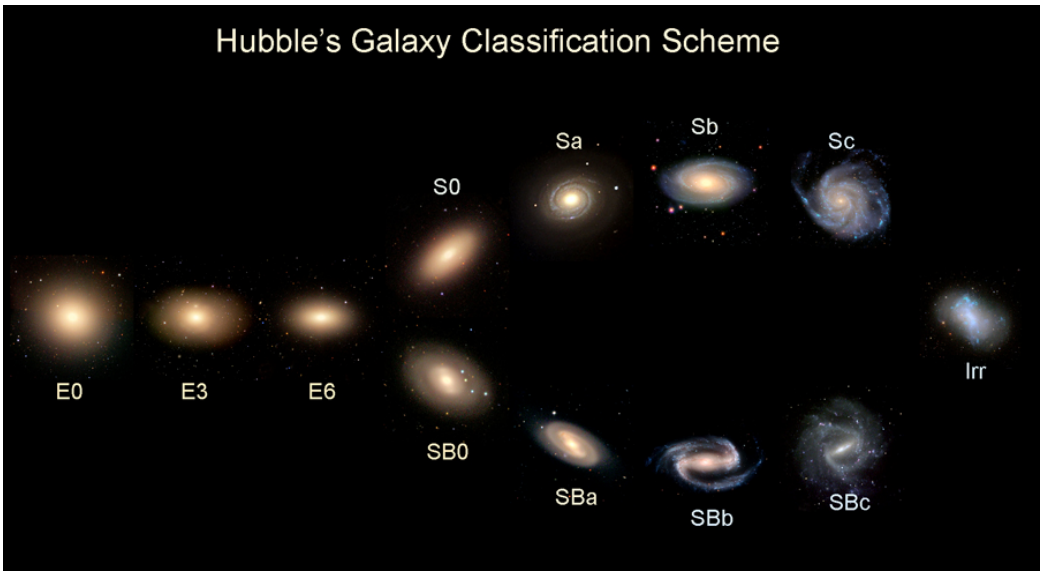

Figure 1.4: Hubble diagram for the morphological classification of galaxies. The peculiar shape of this diagram lead to the nickname of tuning fork. Starting from the left side, we can progressively notice elliptical galaxies (E0, E3, E6), lenticular galaxies (S0, S0b), spiral galaxies (Sa, Sb, Sc, SBa, SBb, SBc) and irregular galaxies (Irr).

of dark matter. In this sense, galaxies can be interpreted as a proxy for the underlying matter density field. Galaxy redshift surveys have played an essential role in the description of the large-scale structure. We know that the Universe is rich of large and almost empty regions called voids, surrounded by elongated filaments and thin sheets made up by galaxies. In the regions connecting two or more filaments, the galaxy number density rises up to values of $10^3\,\mathrm{Mpc}^{-3}$, giving birth to clusters of galaxies. These structures have a typical dimension of $1\,\mathrm{Mpc}^3$, can contain thousands of galaxies and are permeated by a hot intergalactic medium. The X-ray emission of this gas constitutes, along with gravitational lensing, one of the best proxy for the amount of matter inside clusters of galaxies (and thus can be used to give constraints on the matter density parameter, as it is explained in the next section). The resulting galaxy distribution can be interpreted as a web-like structure, as it is shown in Figure 1.5.

From a theoretical point of view, large N-body simulations seem to suggest that the most valid theory for the assembly of dark matter halos on cosmic scales is the hierarchical formation. According to this scenario, small perturbations in the dark matter density field are the first ones to collapse, giving birth to bound structures, and eventually they can merge to produce larger halos. This scenario strongly requires dark matter particles to be

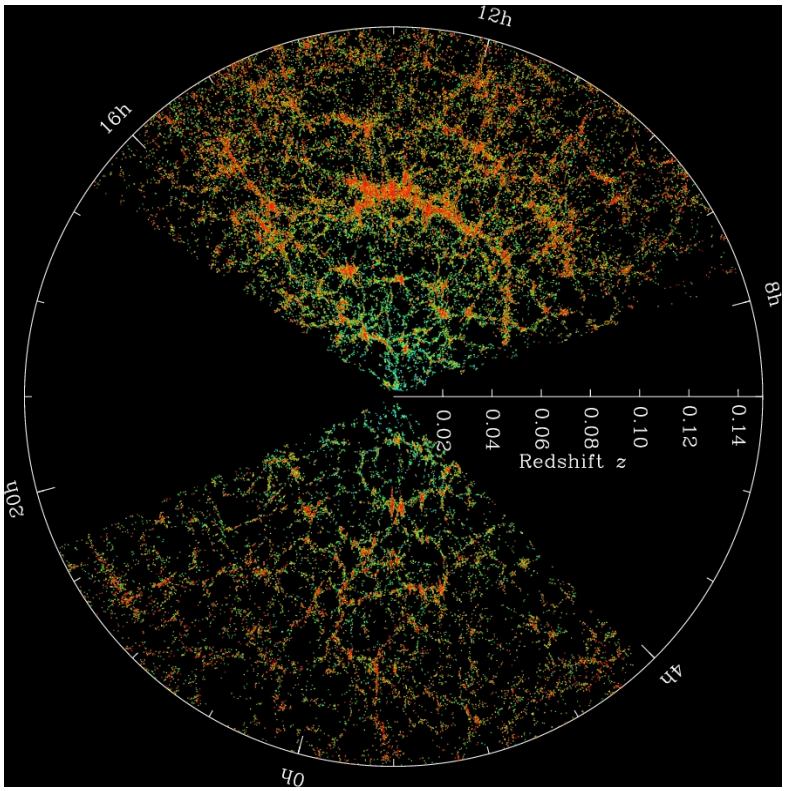

Figure 1.5: Spatial distribution of galaxies in the local Universe as observed by the Sloan Digital Sky Survey. The lightcones are projected along the DEC direction in order to get a 2d image, as a funtion of only redshift and right ascension. The web-like structures, consisting in filament, sheets, clusters and voids, emerges clearly from the plot, as overdense regions in which most of the galactic component is confined.

non relativistic at very high redshifts, so that small-scale fluctuations have enough time to grow and eventually collapse. An alternative model of structure formation is represented by the so-called top-down theories. In this case, large-scale fluctuations (i.e. supercluster sized structures) are the first one to collapse, with subsequent fragmentations to form smaller structures such as galaxies. Top-down structure formation is favoured by hot dark matter, that unfortunately fails in reproducing the current density contrast of galaxies with respect to the cosmic background. Given the complex relation between the assembly of dark matter and the physical processes involved during galaxy formation, it is fair to assume cold dark matter to be the bulk of the matter content in the Universe (and thus hierarchical formation), with the relation between dark matter haloes and galaxies being described by empirical relations such as the Halo Occupation Distribution (see e.g. Yang et al. (2012) for a practical example of the dar matter-galaxy relation

through cosmic time).

One of the morphological aspect, in which cosmologists are mostly interested, is the dependence of the galaxy population from the environment. In the present-day Universe, a significant fraction of the galaxy population is clustered inside large structures like clusters and superclusters, with a characteristic proportion between early and late type galaxies. Indeed, the fraction of ellipticals in clusters with respect to the isolated ones is about 70:30, whereas the values are reversed for spiral galaxies. Therefore, early type galaxies are much more likely to be found inside virialised structures than late type galaxies. This peculiar feature represents an observational demonstration of the morphological evolution of galaxies, that is largely affected by the surrounding environment. Current models for galaxy formation and evolution set an initial stage made up by an irregular gas plenty nebula. During the gravitational collapse, the nebula undergoes a process of fragmentation, setting the stage for star formation, and, in the case it has a non-zero angular momentum, it assumes a spiral configuration. Eventually the galaxy interacts gravitationally with the environment and, if it is close enough to a large mass overdensity like a cluster of galaxies, it moves towards this region. During this motion, ram pressure effects are responsible for stripping off the interstellar medium, leading to an elliptical configuration. This scenario gives a nice description of the observed galaxy distribution at $z \sim 0$. At the same distance, several observations have improved our understanding of the morphological segregation of galaxies as a function of their intrinsic luminosity. Indeed, it seems that more luminous galaxies have also redder colours, and thus more ellipsoidal shapes. On the contrary, irregular galaxies are essentially faint dwarf objects, that show a high star formation rate. Figure 1.6 reproduces the colour distribution (Haines et al. 2016) obtained from the VIPERS and the SDSS-DR7 galaxy samples. The morphological dependence on mass and luminosity is clearly recognisable, as the *red sequence* and the *blue cloud* represent two well-defined feature of the diagram. An intermediate class can be defined between the previous two categories, which can be fitted as an additional gaussian feature between the previously described classes. The latter is typically referred to as *green valley*.

These are the main results achieved by observational astronomy in the local Universe, but more generally down to $z = 1$. In a pure cosmological sense, galaxies are bound structures, that formed out from the initial density perturbations permeating the Universe since its very first time. They are completely separated by the Hubble flow and thus a formalism for the formation of structures is required (Chapter 2 will be mostly focused on this topic). On the other hand, the next section focuses on the theory of the smooth cosmic expansion, introducing many quantities that will be useful in

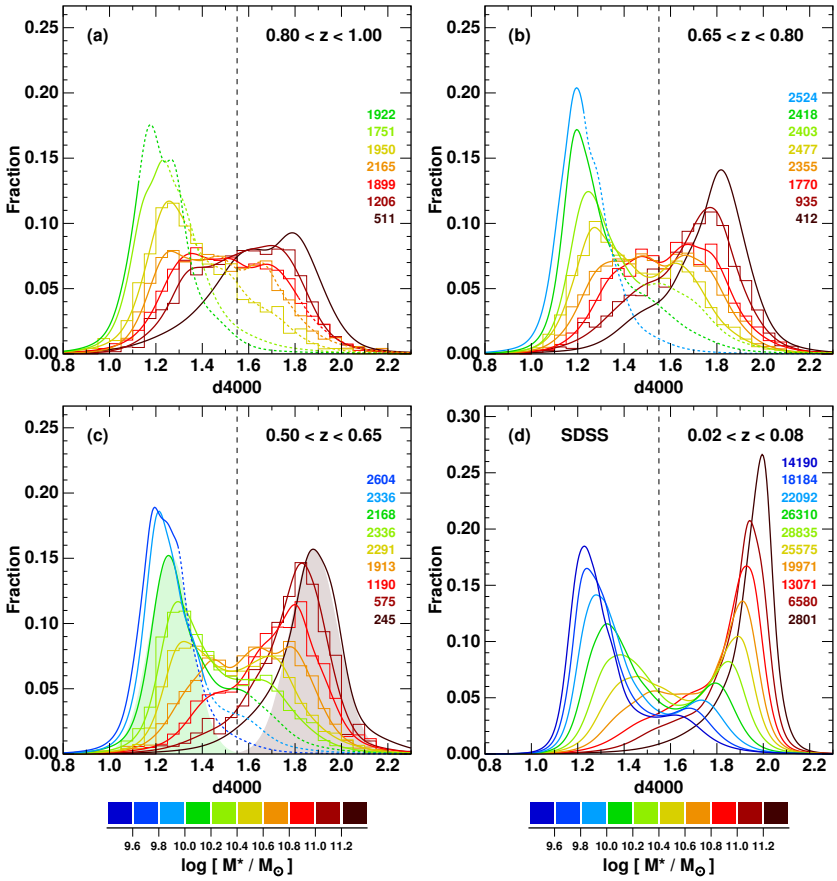

Figure 1.6: The bimodal d4000 distribution of galaxies as a function of stellar mass and redshift, as derived by Haines et al. (2016). Panels from a) to c) show the distribution of VIPERS galaxies in 0.2 dex wide bins of stellar mass (coloured curves), colour coded as indicated, for three redshift bins, as labelled on top of the panels. Panel d) does the same, but for galaxies at $0.02z < 0.08$ taken from SDSS-DR7. The curves become dotted in regions of parameter space below the stellar mass completeness limits of the VIPERS survey. For some stellar mass bins, the d4000 distributions are also shown via histograms with bins of width 0.05 in d4000. The coloured numbers down the right-hand side indicate the number of galaxies in each stellar mass bin. The vertical dashed line indicates the d4000=1.55 limit used to separate the blue cloud and red sequence galaxy populations.

the rest of this work.

1.3 The Standard Model

The Standard Model of cosmology is a parametrization of the Big Bang model in which the Universe is spatially flat, contains dark energy in the form of a cosmological constant Λ, and cold dark matter as the main contribution

to the total matter density. Given this introduction, the theory is mainly known as ΛCDM model. By cold, we mean a particular kind of dark matter whose particles move slowly compared to the speed of light since the Universe was approximately one year old. This implies those particles must be massive and weakly-interacting (WIMPs), although a non-negligible fraction of dark matter could be embodied by the underlying cosmological neutrino background. The Standard Model assumes that general relativity represents the correct theory of gravity also on cosmological scales, and currently it is the most successful interpretation of most cosmological observables (see Longair (2008) and Mo et al. (2010) for the detailed description of a ΛCDM universe; in this section I will provide a brief recap of its most salient features).

Assuming GR, the space-time metric turns into the renowned Friedmann-Lematre-Robertson-Walker (FLRW) metric. This is an exact solution of Einstein's field equations and describes a homogeneous, isotropic, expanding or contracting Universe. The metric can be written as it follows,

$$ds^2 = c^2dt^2 - a^2(t)\left[\frac{dr^2}{1-kr^2} + r^2(d\theta^2 + \sin^2\theta\, d\phi^2)\right], \tag{1.2}$$

where r, θ, ϕ are the spherical coordinates, k is the scalar curvature of the space-time, and $a(t)$ is a time-evolving scale factor that represents the expansion of the Universe. The latter is defined as

$$a(t) = \frac{d_p(t)}{d_p(t_0)}, \tag{1.3}$$

where d_p is the proper distance from a given object and a subscript 0 means that quantity is evaluated at the present time. The set (r, θ, ϕ) is made of comoving coordinates, that is, coordinates that factor out the expansion of the Universe, giving a distance that does not change in time due to the expansion of space. Then, the relation between proper d_p and comoving distance r is the following one,

$$d_p(t) = a(t)\, r, \tag{1.4}$$

where in this case we have explicitly written the dependence of the proper distance on time only through the scale factor. Actually, although the comoving distance of an object is insensitive to the stretching of space (by definition), it may eventually change due to gravitational interactions with the local environment, giving birth to peculiar motions that are completely uncorrelated to the Hubble flow. Nevertheless, this topic will be addressed more concretely in Section 2.4.

In place of the cosmic time t, the conformal time τ is usually defined as $d\tau \equiv dt/a(t)$, so that the scale factor can be factorised out from the previous expression. In this case the FLRW metric turns into

$$ds^2 = a^2(\tau)\left[c^2 d\tau^2 - \frac{dr^2}{1-kr^2} + r^2(d\theta^2 + \sin^2\theta\, d\phi^2)\right]. \tag{1.5}$$

Depending on the sign of k, the space-time becomes respectively flat ($k = 0$), positively curved ($k > 0$) or negatively curved ($k < 0$). Figure 1.7 sketches these three possible configurations using a two-dimensional surface (though in reality we have to deal with a 3D space). The labelled Ω next to the three geometrical realisations is a density parameter that will be defined shortly. As already suggested in the introduction of this section, there are multiple evidences supporting a model with zero curvature. Therefore the reference ΛCDM model is based on a flat universe, where the scalar curvature is zero. This implies that a light path ($ds = 0$) that travels along a radial direction ($d\theta = d\phi = 0$) must satisfy the relation $dr = c\,dt/a(t)$. Integrating the previous expression between the emission time t_e and the current time t_0, we get a useful relation between the scale factor $a(t)$ and the observed redshift of a luminous source,

$$1 + z = \frac{1}{a(t_e)}. \tag{1.6}$$

Equation 1.6 explicitly shows that redshift and scale factor can be mutually interchanged, and that any time-dependent quantity can be expressed as a function of both of them. On the contrary, their dependence on cosmic (and conformal) time relies strongly upon the chosen cosmological model. These considerations are valid also in different cosmological models (for instance in modified gravity), as long as the scalar curvature is null.

The FLRW space-time metric has the role of describing the geometrical properties of the space-time, that according to General Relativity are intimately connected to the matter-energy content of the Universe via Einstein's field equations,

$$R_{\mu\nu} - \frac{1}{2}g_{\mu\nu}R + \Lambda g_{\mu\nu} = \frac{8\pi G}{c^4}T_{\mu\nu}. \tag{1.7}$$

Here $R_{\mu\nu}$ is the Ricci tensor, R is the scalar curvature (the trace of $R_{\mu\nu}$), $g_{\mu\nu}$ is the space-time metric, and $T_{\mu\nu}$ is the stress-energy tensor that describes the distribution of energy and momentum across the Universe. By moving the dark energy term to the right member of Equation 1.7, it becomes straightforward to notice how the energy content of the Universe (right member) defines the geometry of the space-time (left member), and how the latter contributes in generating the total gravitational field. Actually, Equation 1.7 represents the relativistic analogue of Poisson's equation.

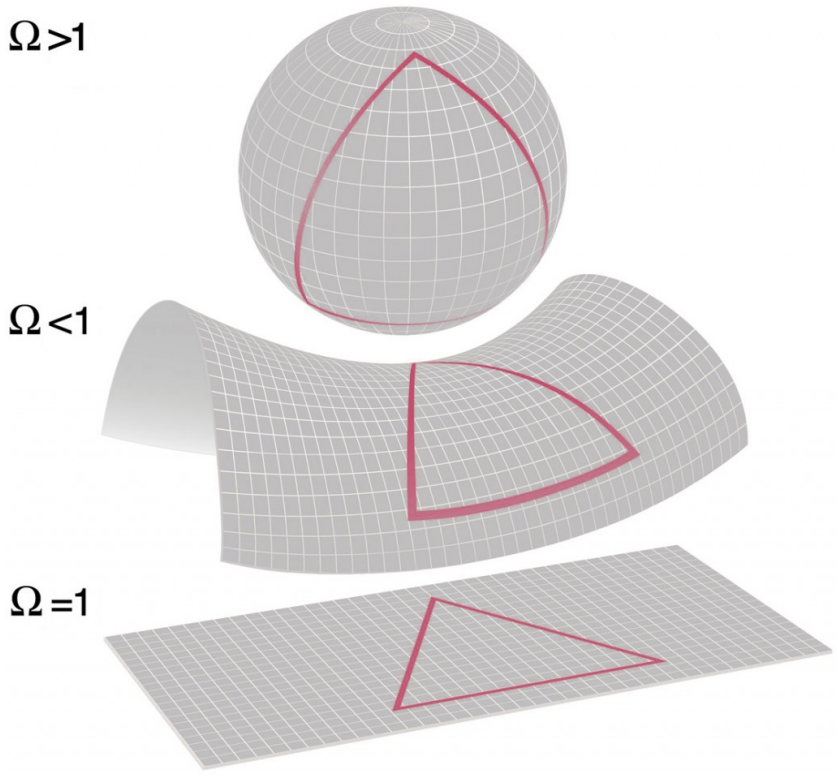

Figure 1.7: Example of the three possible configuration in which a universe described by the FLRW metric can experience. In detail, we have a positively curved (spherical surface), a negatively curved (hyperbolic surface) and a flat (plane) universe. The *Omega* term in the labels represent the total density parameter, and its definition can be found in Equation 1.11.

Combining Equations 1.2 and 1.7, we derive a set of equations that governs the expansion of space in a homogeneous and isotropic Universe within the context of general relativity. These equations are known respectively as the first and second Friedmann equation, by the name of the Russian physicist that firstly derived them in 1922. They can be expressed in the following way,

$$\frac{\dot{a}^2 + kc^2}{a^2} = \frac{8\pi G\rho + \Lambda c^2}{3} \tag{1.8}$$

$$\frac{\ddot{a}}{a} = -\frac{4\pi G}{3}\left(\rho + \frac{3P}{c^2}\right) + \frac{\Lambda c^2}{3}, \tag{1.9}$$

with ρ and P being respectively the density and the pressure of the fluid permeating the Universe. Note that in this case, for the sake of completeness, we have not suppressed the curvature term. These equations are of outstanding importance: indeed, the first one states that the variation of the scale factor

as a function of the cosmic time is dictated by the total amount of energy contained in the fluid (matter, radiation, curvature and, in a ΛCDM, dark energy), whereas the second one gives a mathematical formalism for the cosmic acceleration, that is produced by the balance between the energy density and the self-pressure of the fluid.

The term $\dot{a}/a$ is usually referred to as the expansion history of the Universe and is denoted by H (the Hubble constant H_0 is just the expansion history evaluated at the present time). In the same spirit of the conformal time τ, it is possible to define a conformal Hubble parameter as

$$\mathcal{H} = \frac{1}{a}\frac{da}{d\tau} = \frac{da}{dt} = aH. \tag{1.10}$$

Cosmological quantities are typically expressed in units of the reduced Hubble constant, $h = H_0/(100\,\mathrm{Km\,s^{-1}\,Mpc^{-1}})$, in order to factor out the uncertainty on the value of H_0 from the measurements. In the same way, the energy density of the fluid is recast in a more efficient notation, that is

$$\Omega(t) = \frac{\rho(t)}{\rho_c(t)} = \frac{8\pi G\rho(t)}{3H^2(t)}, \tag{1.11}$$

with the quantity $8\pi G/3H^2 \equiv \rho_c$ defined as the critical density for a flat Universe. Indeed, it can be proved that the curvature of the space-time is directly related to Ω, so that $k > 0$, $k = 0$, $k < 0$ respectively for $\Omega > 1$, $\Omega = 1$ and $\Omega < 1$. In addition, each fluid component evolves differently with time (something that can be obtained using the first law of thermodynamics), such that

$$\rho_w = \rho_0 a^{-3(1+w)}, \tag{1.12}$$

where w is defined in the state equation (1.14) and assumes different values according to the particular component ($w = 0$ for non-relativistic matter, $w = 1/3$ for radiation and $w = -1$ for the cosmological constant).
Exploiting the full information listed above, it is possible to rewrite the first Friedmann equation in a more compact format,

$$\frac{H^2}{H_0^2} = \frac{\Omega_{m,0}}{a^3} + \frac{\Omega_{r,0}}{a^4} + \frac{\Omega_{k,0}}{a^2} + \Omega_{\Lambda,0}, \tag{1.13}$$

where, once again, it is clear how the dynamics experienced by the Universe is generated by the combination of different time-evolving energy component. In this case, the cosmological constant is simply regarded as a component with energy density $\rho_\Lambda = \Lambda c^2/8\pi G$.
For each individual component we can now introduce the state equation,

$$P_w/c^2 = w\rho_w, \tag{1.14}$$

$H_0\,[\mathrm{Km\,s^{-1}\,Mpc^{-1}}]$	67.3 ± 1.2
$\Omega_c h^2$	0.1197 ± 0.0022
$\Omega_b h^2$	0.02222 ± 0.00023
Ω_m	0.315 ± 0.013
Ω_Λ	0.685 ± 0.013

Table 1.1: 2015 Planck measurements of the Hubble constant and density parameters from the CMB temperature-temperature spectrum. Subscripts c and b correspond respectively to cold dark matter and baryons. For simplicity, we are not expliciting the subscript 0 to the density parameters.

in order to reduce by one degree of freedom the second Friedmann equation. Indeed, substituting the pressure term in Equation 1.9 with the previous expression, it is possible to characterise each component according to its impact on the cosmic acceleration: if $P > -\rho c^2/3$ (matter and radiation), the expansion is slowed down, otherwise, if $P < -\rho c^2/3$ (cosmological constant), the expansion is speeded up. For this reason, dark energy can be considered as a negative-pressured fluid that drives out the acceleration of the Universe, contrasting the collapse that matter and radiation would cause by themselves. One of the possible interpretation of dark energy is the energy of void, although recent calculations have shown that there are several missing order of magnitudes between the predicted and the observed energy density.

We refer to the next chapter for the 2015 Planck CMB measurements of the cosmological parameters in the context of a ΛCDM (unless explicitly stated, we use these parameters as our reference ΛCDM). In this section, we are mostly interested in the values of the density parameters and the Hubble constant, that are listed in Table 1.1. Dark energy is the dominant component in the Universe (it corresponds to about the 70% of the total energy density), whereas non relativistic matter corresponds just to a 30% fraction. Furthermore, of this fraction, only about 1/10 corresponds to luminous matter (stars, gas, dust). This is one of the strongest reason that makes the understanding of physics on cosmological scales a strenuous task: we have direct access only to 5% of the total amount of matter-energy in the Universe. Today, radiation (in the form of CMB photons and cosmic neutrinos) represents only a small fraction of the total energy density ($\Omega_{r,0} \sim 9 \cdot 10^{-5}$), though in the early Universe it was the dominant factor. Using Equation 1.13, it is possible to derive the relation between cosmic time and redshift, as

$$H_0 t = \int_z^\infty \frac{dz'}{(1+z')^2[\Omega_{m,0}(1+z')^3 + \Omega_{r_0}(1+z')^4 + \Omega_{k,0}(1+z')^2 + \Omega_{\Lambda,0}]^{1/2}}. \tag{1.15}$$

This equation is valid in a ΛCDM model, and has no analytical solutions, thus we need to rely on numerical methods.

The current age of the Universe is derived setting to 0 the lower bound of the integral, leading to a value of $t_0 = 13.5\,\mathrm{Gyr}$. In the history of the Universe, we can highlight three different epochs, a radiation-, matter- and Λ-dominated era. Radiation determines the dynamics of the Universe down to $z_{\mathrm{eq}} \sim 3600$ ($a_{\mathrm{eq}} = \Omega_{r,0}/\Omega_{m,0} = 2.8 \cdot 10^{-4}$), when non-relativistic matter starts to dominate. This period goes under the name of *equivalence*, since the radiation and matter density parameters have the same amplitude, and occurs at a time $t_{\mathrm{eq}} = 4.7 \cdot 10^4\,\mathrm{yr}$ after the Big Bang. Matter, in turn, gives way to dark energy when the scale factor is $a = (\Omega_{m,0}/\Omega_{\Lambda,0})^{1/3} = 0.75$, that corresponds to a time $t = 9.8\,\mathrm{Gyr}$. Thus, our Universe has entered the Λ-dominated epoch since a relatively small time. Figure 1.8 sketches in a naive way the time evolution of the energy density of different components as a function of the scale factor. In a similar way of reasoning, it is possible to compute the comoving distance from a luminous source using Equation 1.8. This yields

$$r(z) = \frac{c}{H_0} \int_0^z \frac{dz}{[\Omega_{m,0}(1+z)^3 + \Omega_{r_0}(1+z)^4 + \Omega_{k,0}(1+z)^2 + \Omega_{\Lambda,0}]^{1/2}}, \quad (1.16)$$

and by additionally multiplying for the corresponding scale factor, it is possible to get the proper distance from the object at the current time. Given that in most of the current cosmological models the age of the Universe is finite, a hypothetical photon emitted at the beginning of time can travel at most up to finite distance, that is usually defined as the horizon radius. This means that we cannot observe objects that are outside the horizon, since light has not had enough time to reach us. In the limit $z \to \infty$, it is possible to obtain an estimate of this distance, that in the ΛCDM corresponds to $r_{\mathrm{hor}} \sim 14000\,\mathrm{Mpc}$.

It is important to stress how the ΛCDM is not the only possible realisation of a Universe dominated by dark energy. Indeed, an alternative scenario is represented by quintessence models, in which the cosmological constant is substituted by a time-evolving scalar field that is able to produce the accelerated expansion of the Universe. In this case the state equation for dark energy is no more constant with time, and new degrees of freedom are introduced in the parameter fit. Nevertheless, even allowing for these new parameters, it has been found that the evolutionary behaviour does not deviate highly from the simpler case of a non-evolving equation of state.

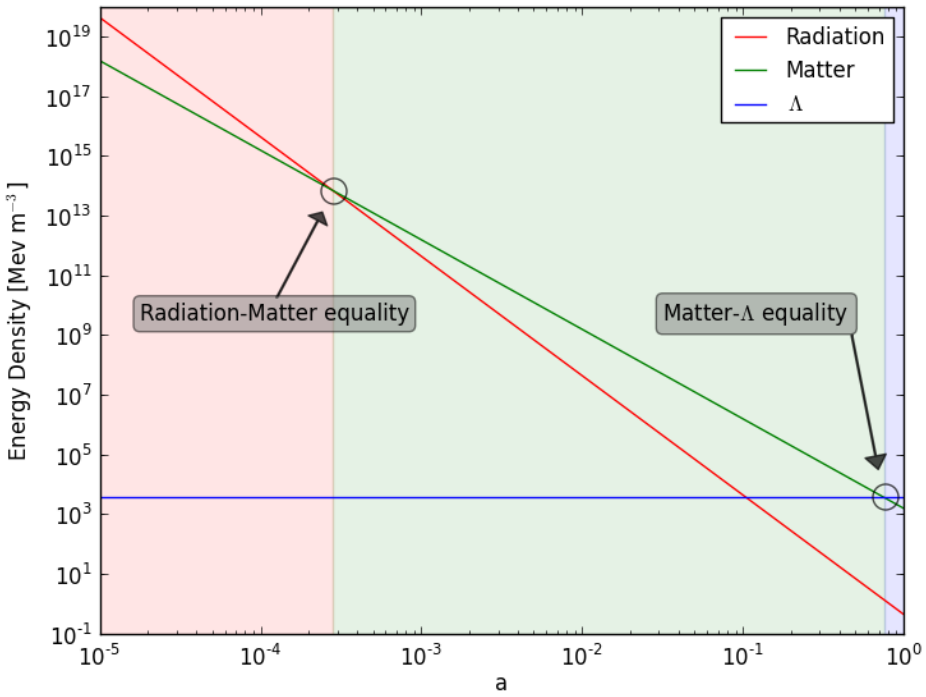

Figure 1.8: Evolution for the energy density of different component of the Universe, according to a ΛCDM model. Given that in this scenario the value of w_Λ is unity, the contribution of Λ to the total energy density is constant throughout time. The latter becomes dominant at a relatively recent time. Shaded regions corresponds to different epochs (respectively red to radiation-, green to matter-, and blue to Λ−dominated epoch).

1.3.1 Thermal history of the Universe

Extrapolation of the expansion of the Universe backwards in time using general relativity yields an infinite density and temperature at a finite time in the past. This singularity signals the breakdown of general relativity and of all the laws of physics. After $\sim 10^{-11}$ s, the typical particle energy drops to values that can be attained by current particle physics experiments, and therefore the evolution of the Universe after this time become less speculative.

At about 10^{-6} s, the Universe is filled with an extremely hot and dense fluid made up by photons and ionized hydrogen. These elements are tightly coupled together via Thompson scattering, and since cold dark matter interacts with the environment only gravitationally, it takes no part in the initial evolution of the baryon-photon fluid. During the expansion of space, the internal properties of the fluid are shaped according to the first law of

thermodynamics, in a way that its temperature scales as

$$T \propto a^{-1}. \tag{1.17}$$

Photoionization occurs with high efficiency as long as the temperature and the density of the fluid is high enough, but soon after the Big Bang, these quantities reach values that allows free protons to combine and form heavier nuclei, like deuterium, helium and lithium. This process goes under the name of *Big Bang nucleosynthesis*, it takes place in the first minutes after the start of the evolution, and its validity is largely proved by the current abundance of light elements in the solar system. From an energetic point of view, the primordial production of elements is very inefficient, given that most of the baryonic matter inside the Universe is still in the form of hydrogen and helium. In order to explain the presence of heavier nuclei, the most valid theory is that they are produced much later by stellar nucleosynthesis in evolving stars and are scattered throughout the Universe during supernova explosions.

During and after these processes, the evolution is mainly driven by radiation that represents the bulk of the total energy density. As soon as the Universe becomes approximately 10^4 times smaller its current size (the time of equivalence), it enters the matter-dominated epoch, and with time flowing, it is possible to recognize a well-defined moment at which the baryon-photon fluid undergoes a radical transformation, known as the epoch of *recombination*. Recombination occurs about 378000 yr after the Big Bang (at $z = 1100$) and refers to the epoch at which charged electrons and protons first become bound to form electrically neutral hydrogen atoms. This happens as a natural consequence of the continuous density drop of the baryon-photon fluid, leading to a typical mean free path for photons that becomes comparable to the horizon scale. The decoupling of photons occurs abruptly when the rate of Compton scattering Γ is approximately equal to the rate of expansion of the Universe H. After photons have performed their last scatter with baryons, they are finally able to stream freely, producing the cosmic microwave background as we know it, and the Universe becomes transparent and neutral. This epoch marks an important change in the internal composition of the Universe. Indeed, before photon decoupling, there exists a single photon-baryon fluid in thermal equilibrium, with photons damping out matter perturbations. After the decoupling, the fluid separates into two different gases, and, while photons proceed their motions undisturbed, baryons are free to collapse under their own self-gravity but most of all under the strong gravitational field generated by dark matter (that meanwhile has already started to collapse into non-linear structures).

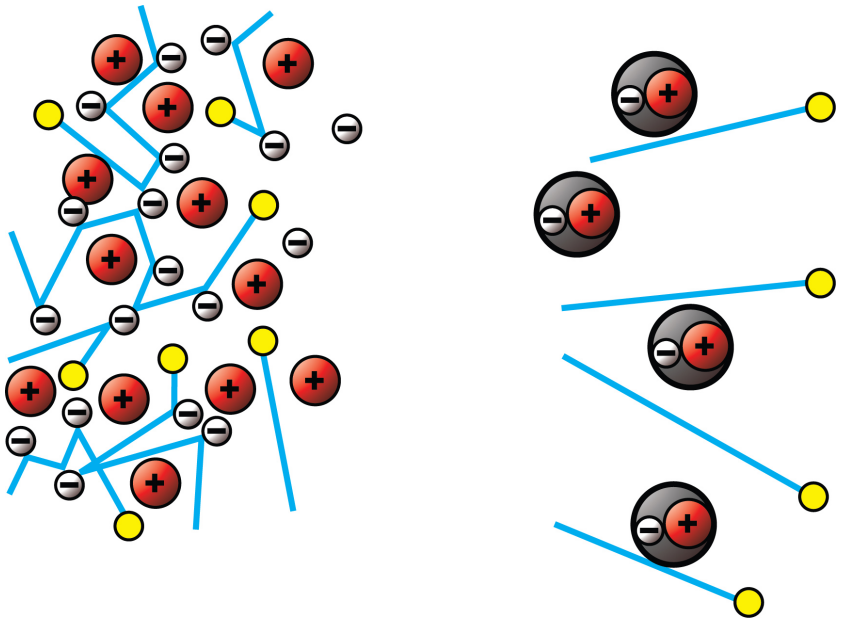

Figure 1.9: Sketch of the most direct consequence of the recombination between protons and electrons. Before this transition (left), photons are closely coupled with baryons, given that they experience continuous Thompson scatters with the electrons. On the contrary, as long as the temperature become low enough to prompt the recombination of the baryonic component, photons can freely cross electrons unperturbed.

As soon as the photons are decoupled, the only radiation emitted is the 21 cm spin line of neutral hydrogen. The Dark Ages are currently thought to have lasted between 150 million to 800 million years after the Big Bang, until the very first stars are born from gravitational collapse, ignite and start to produce light. This electromagnetic radiation is capable of photoionize neutral hydrogen, and for this reason the Universe reverts from being neutral, to once again being an ionized plasma. This second phase change of hydrogen in the Universe (after recombination) is known as *reionization* and it is thought to happen at $5 < z < 20$. At that time, matter has been diffused by the expansion of the Universe, and the scattering interactions of photons and electrons are much less frequent than before electron-proton recombination. Thus, a Universe full of low density ionized hydrogen remains transparent, as it is in our Universe today.

The growth of structures (baryonic and non) goes on as if the Universe is completely dominated by matter for most of the following time. During this phase, the behaviour of the actual Universe can be well-approximated with the one described by an Einstein-de Sitter cosmology ($\Omega_m = 1$, $\Omega_\Lambda = \Omega_r = \Omega_k = 0$). This model corresponds to a flat universe which expands forever

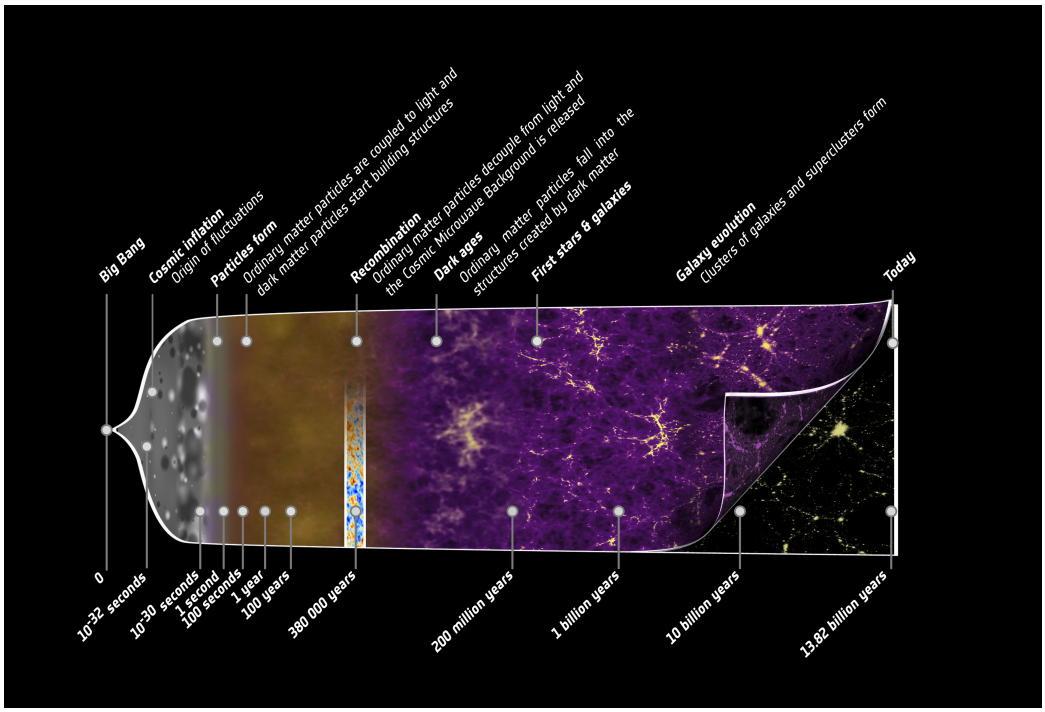

Figure 1.10: Sketch of the history of our Universe realised by the Planck collaboration. The main processes and epochs are explicitly displayed on top of the figure.

with a negative acceleration, with an energy budget sufficient to make it escape the gravitational collapse at the infinity. This choice is particularly interesting, since the Standard Model predicts the Universe to remain in the matter-dominated era for most of its lifespan. That is the reason for mentioning this particular cosmology, and using it as a benchmark model in the following chapter. In a more recent time ($z \sim 0.3$), dark energy becomes the main contribution to the energy content in the Universe, leading to an accelerated expansion like the one we observe today. In this case, the approximation used during the matter-dominated epoch is no longer valid, and one has to include the effects of dark energy in the analysis.

1.3.2 Cosmic inflation

Although it provides an outstanding agreement with observational data coming from multiple probes, the Standard Model of cosmology has three important issues that are not easily explained using the theory illustrated so far. These problems arise from the observation that, in order to look like it does today, the Universe has to start from very finely tuned initial conditions

at the epoch of the Big Bang.

1) **Flatness problem:** It is known since the 1960s that the density of matter in the Universe is comparable to the critical density necessary for a flat Universe, and this gives strong constraints to the value of the total density parameter, $\Omega_0 = 1$. This knowledge throws away any speculation about our Universe being spherically or hyperbolically curved (non-Euclidean geometries). Extrapolating $\Omega(z)$ backward in time, its closeness to unity becomes even tighter. For instance, at the Planck time, $t_P \approx 5 \cdot 10^{-44}\,\mathrm{s}$, the density parameter has to satisfy the relation $|1 - \Omega(t_P)| \leq 10^{-60}$, and a coincidence of one part over 10^{60} is very unlikely. This problem is exacerbated by recent observations of the cosmic microwave background that have demonstrated that the Universe is flat to the accuracy of a few percent. It would be much more appreciable if we could find a physical process responsible for the flattening of the Universe in its very early ages.

2) **Horizon problem:** The horizon problem is the problem of determining why the Universe appears statistically homogeneous and isotropic in accordance with the cosmological principle. Indeed, the anisotropies of the cosmic microwave background have an amplitude of just $\delta T/T \approx 10^{-5}$, as measured from Planck and previous CMB based projects. However this scenario is hardly explainable in a simple Big Bang model, because gravitational expansion does not give the early Universe enough time to reach thermal equilibrium. The size of the horizon at the epoch of recombination is approximately a half of the distance separating two antipodal points on the last scattering surface. This means that two widely separated regions of the observable Universe cannot have come into causal contact because they move apart from each other faster than the speed of light. This fact is even more flooring if we consider the angular separation of two points at the last scattering surface separated by a horizon distance, something that is close to 2°. Planck CMB temperature spectrum (Figure **??**)shows that on the contrary temperature fluctuations on scales above 2° are extremely small. In the early Universe, it is not possible to send a light signal between the two regions, and given that they have no interactions, it is difficult to explain why they have the same temperature.

3) **Magnetic monopoles problem:** The magnetic monopole problem says that if the early Universe was hot like the one proposed by the Big Bang model, a large number of heavy, stable magnetic monopoles would be produced. This problem is mostly related to Grand Unified Theories, which propose that at high temperatures the electromagnetic, strong, and weak

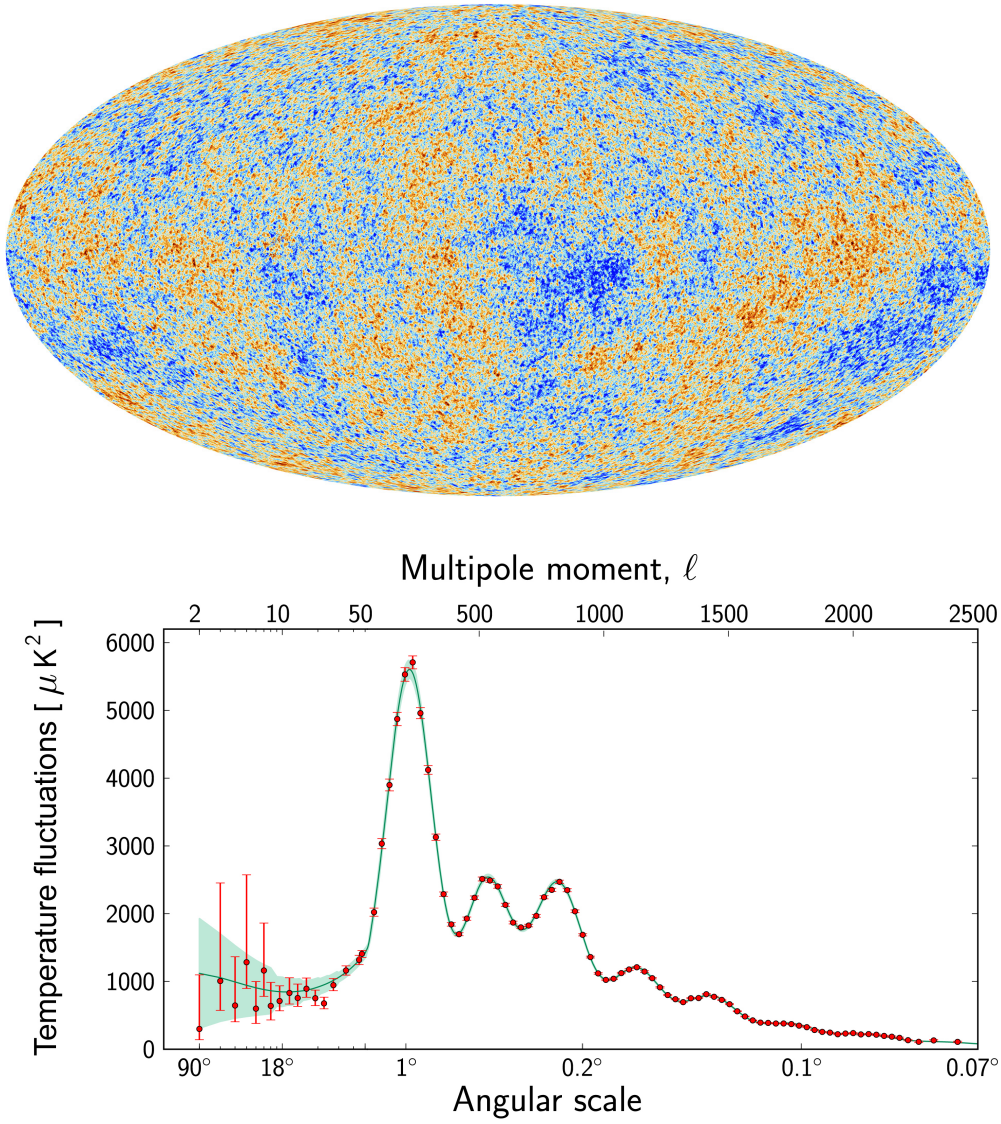

Figure 1.11: Top: 2015 Planck temperature map of the sky, showing the anisotropies of the Cosmic Microwave Background. The picture shows tiny temperature fluctuations that correspond to regions of slightly different densities, representing the seeds of all future structure. Bottom: the angular power spectrum of temperature fluctuations of the cosmic microwave background, detected by Planck, as a function of the angular separation on the sky. Measurements are shown as red circles, while the best ΛCDM fit is represented by the green line. At large angular separations, cosmic variance starts to be significant, producing larger errorbars.

nuclear forces are not actually fundamental forces but arise due to spontaneous symmetry breaking from a single gauge theory. These monopoles are expected to be copiously produced in the early ages of the Universe and they should have persisted to the present day. Nevertheless, all searches for them have failed, placing stringent limits on the density of relic magnetic monopoles in the Universe.

One of the most successfull theory trying to solve the above problems in the context of a ΛCDM is the inflationary solution, developed in the early 1980s, but whose principal formalisation can be attributed to the combined work of Guth, Linde and Steinhardt in 2002. In theoretical physics and cosmology, inflation can be defined as the hypothesis that there was a period, early in the history of our Universe, when the expansion of space was dominated by a cosmological constant Λ_I, and thus it was accelerating outward. The inflationary epoch lasts from 10^{-36} s seconds after the Big Bang to some time between 10^{-33} and 10^{-32} s. Following the inflationary period, the Universe continues to expand, but at a less accelerated rate. As for the concept of dark energy, while the detailed particle physics mechanism responsible for inflation is not known, the basic picture makes a number of predictions that have been confirmed by observations. Inflation is able to give a theoretical framework in which the previous paradigms are easily explained. Indeed, the observable Universe is but a causal patch of a much larger unobservable Universe, with the edge of this separation represented by the cosmological horizon. If the early Universe is dominated by a cosmological constant Λ_I, then equation 1.8 turns into

$$\left(\frac{\dot{a}}{a}\right)^2 = \frac{\Lambda_I}{3}. \tag{1.18}$$

More effectively, if the exponential expansion starts at a time t_i and lasts until some later time t_f, then the evolution of the scale factor can be represented in the following way,

$$a(t) = \begin{cases} a_i(t/t_i)^{1/2} & t < t_i \\ a_i \exp[H_I(t-t_i)] & t_i < t < t_f \\ a_i \exp[H_I(t_f-t_i)](t/t_f)^{1/2} & t > t_f \end{cases} \tag{1.19}$$

where $H_I = (\Lambda_I/3)^{1/2}$ is the value of the Hubble constant during the carrying out of inflation. The results is that the scale factor grows by a factor

$$\frac{a(t_f)}{a(t_i)} = \exp[H_I(t_f - t_i)], \tag{1.20}$$

and if the duration of inflation is long enough compared to the Hubble time H_I^{-1}, then the expansion becomes abrupt, while the cosmological horizon stays put. With exponentially expanding space, two nearby observers are separated very quickly, so that the distance between them eventually exceeds the size of the horizon. As the inflationary field slowly relaxes to the vacuum, the cosmological constant goes to zero and space begins to expand normally. The new regions that come into view during the normal expansion phase are exactly the same regions that are pushed out of the horizon during inflation, and this explains why they have approximately the same temperature. Furthermore, the evolution of the density parameter turns into

$$|1 - \Omega(t)| \propto \exp(-2H_I t), \tag{1.21}$$

and even if the inflation lasts for a short period, the quick stretching of space produces a Universe with a final curvature almost null. At last, the apparent absence of magnetic monopoles can be explained assuming that during inflation the number density of these particles falls down to values that prevent us from observing them today.

The hypothetical mechanisms responsible for the establishment of inflation are multiple. The most considered scenario is that of a space-time dependent scalar field $\phi(\vec{r}, t)$ with a potential $V(\phi)$ like the one shown in Figure 1.12. For a precise range of values, the scalar field satisfies the relation

$$\left(\frac{dV}{d\phi}\right)^2 \ll \frac{v_0^2}{E_P^2}, \tag{1.22}$$

where V_0 is the value of the potential in the plateau and E_P is the Planck energy. In this way, if the inflation field is nudged from $\phi = 0$ to $\phi = +d\phi$, it slowly falls down along a metastable state until it reaches the true minimum at $\phi = \phi_0$. Given that the state parameter w can be expressed as

$$w = \frac{\frac{1}{2}\dot{\phi}^2 - V(\phi)}{\frac{1}{2}\dot{\phi}^2 + V(\phi)}, \tag{1.23}$$

and that along the plateau the slope of the curve is significantly flat, we end up with an effective cosmological constant ($w = -1$) driving inflation until the minimum of the potential is reached. During the transition, the expansion of space becomes exponential and inflation can freely occur. Eventually, once the scalar field reaches the potential well, the expansion turns back into a power law.

Since its first introduction, the inflationary paradigm has become widely accepted, although many physicists have voiced criticisms, claiming untestable

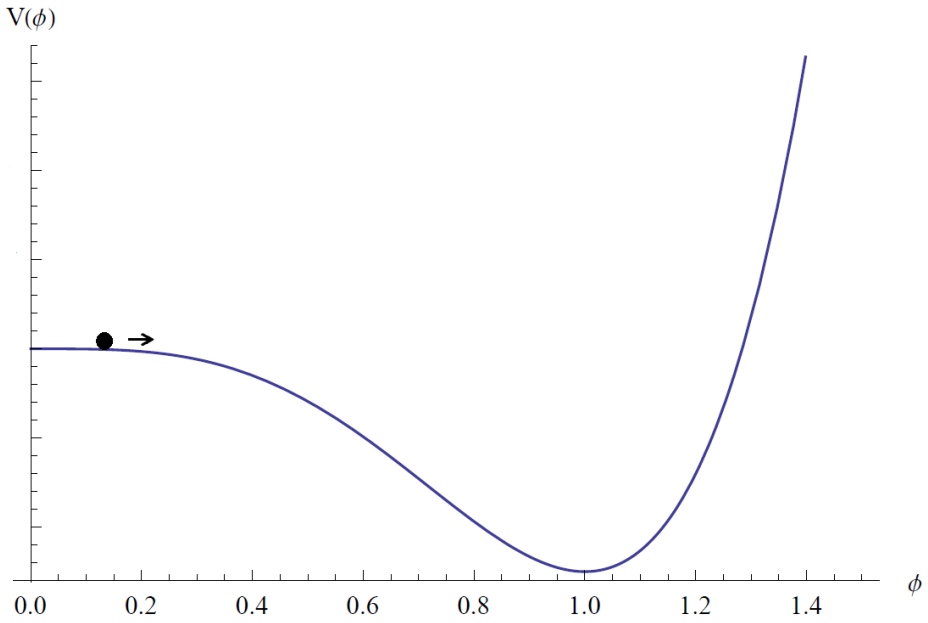

Figure 1.12: A possible realisation of a scalar field ϕ that gives rise to an inflationary epoch. The scalar field starts on the left part of the plot and slowly falls down along the plateau because of the potential minimum on the right. During the slide, the expansion of space becomes exponential.

predictions and a lack of serious empirical support. A recurrent criticism of inflation is that the invoked inflation field does not correspond to any known physical field, and that its potential energy curve seems to be an ad hoc contrivance to accommodate almost any of the current data. Nevertheless, as for today, it is one of the most accepted theory related to the early Universe, back to a time that we cannot directly probe. For an introductory review on cosmic inflation we redirect the reader to Liddle (1999).

Chapter 2

GALAXY CLUSTERING

Throughout Section 1.3, we have considered the Universe as an isotropic box, filled with a perfectly homogeneous fluid made up by matter, radiation and dark energy. However, observations of the local Universe performed by multiple photometric and spectroscopic surveys have proved how naive is this representation of the cosmos respect to its true appearance. As a matter of fact, today we can see bound structures on an extremely large scale range, from stars and planets to galaxies and, on even larger scales, galaxy clusters and sheet-like structures of galaxies separated by enormous voids (the latter having such a small number densities to be considered almost as empty) (see Figure 1.5).

The theory of structure formation attempts to model how these structures formed out from gravitational instability of small early density ripples. According to the theory behind inflation, these density perturbations are the direct output of small quantum fluctuations featuring the very early Universe. As long as inflation takes place, these small overdensities are stretched and brought over scales larger than the horizon radius. At this point, gravitational instabilities become the main driver of the formations of structures and of the consequent evolution of the density field. Once the baryonic component has finally decoupled from radiation, it starts falling towards the dark matter overdensities, that in the meantime have accreted to form the first pattern of haloes and voids. Today, we have evidences of these gravitational processes both in the large-scale structure of the Universe, but also in the presence of baryonic structures such as galaxies and stars. We refer to Longair (2008) and Mo et al. (2010) for a comprehensive and detailed description of the large-scale structure of the Universe as observed from galaxy surveys.

Focusing on cosmological scales, it is important to stress how gravity is the only engine driving its growth and evolution: indeed, the Universe can be regarded as electromagnetically neutral on large enough scales, and the

remaining fundamental interactions are close-ranged forces, that show no significant impact on the formation of structures.

The modern ΛCDM model is successful not only at predicting the observed expansion history $H(z)$, but also the observed large-scale distribution of galaxies, clusters and voids. Though, more exotic cosmological models suggesting the modification of gravity on cosmic scales are also able to predict $H(z)$. The aspect that really can discriminate between different gravity models is not the current distribution of galaxies but rather its time evolution, since as already stated gravity is the only engine working on cosmological scales. This motivates the use of a theory of structure formation, whose basic principles are the main topic of this chapter.

2.1 Perturbation theory

In physical cosmology, the theory of cosmological perturbation is the theory by which the evolution of structure is understood and subsequently modelled. From a general point of view, it employs classical mathematical methods that consist in splitting the solution of a problem into a solvable and a perturbative term. Focusing in particular on its cosmological aspect, it uses general relativity to compute the gravitational forces causing small perturbations to grow and eventually seed the formation of stars, quasars, galaxies and clusters. Nevertheless, its reliability in describing the formation of structures can be considered good enough only on the largest scales, while on smaller scales it is common practice to rely on cosmological N-body particle simulations.

2.1.1 Linear perturbation theory

The handy aspect of working with the assumptions of linear regime is that the equations describing the growth of matter perturbations can be solved analytically. This provides an useful insight to how matter clusters at very large separations, on scales where such assumptions are reasonable, but also gives some hints for the portrayal of the full non-linear theory.

An useful and common approach is to consider dark matter as a pressureless non-relativistic fluid, an hypothesis that is valid as long as the velocity dispersion of dark matter particles is sufficiently small, so to prevent particle diffusion out of the region of interest. If this is the case, then the description

of the matter density field must obey the fluid equations,

$$\frac{\partial \rho}{\partial t} + \boldsymbol{\nabla}_{\boldsymbol{r}} \cdot (\rho \boldsymbol{v}) = 0 \qquad \text{(Continuity equation)} \tag{2.1}$$

$$\frac{\partial \boldsymbol{v}}{\partial t} + (\boldsymbol{v} \cdot \boldsymbol{\nabla}_{\boldsymbol{r}})\boldsymbol{v} = -\frac{\boldsymbol{\nabla}_{\boldsymbol{r}} P}{\rho} - \boldsymbol{\nabla}_{\boldsymbol{r}} \phi \qquad \text{(Euler equation)} \tag{2.2}$$

$$\nabla^2_{\boldsymbol{r}} \phi = 4\pi G \rho \qquad \text{(Poisson equation)} \tag{2.3}$$

where $\rho(\boldsymbol{r}, t)$ is the density field, $\boldsymbol{v}(\boldsymbol{r}, t)$ is the velocity field, $P(\boldsymbol{r}, t)$ is the self-pressure and $\phi(\boldsymbol{r}, t)$ is the total gravitational field generated by the fluid itself. It is remarkable how the dynamics of such fluid is completely described by its internal properties, density and pressure, and by its self-generated gravity. Clearly, a Newtonian approach like the one above is valid only in the limit where all the perturbations that are considered are well inside the horizon scale, $k \gg H$. Looking for perturbative solutions in the comoving frame (where the new spatial variable is $\boldsymbol{x} = \boldsymbol{r}/a$), and substituting the cosmic quantities (t, H) with their corresponding conformal quantities $(\tau, \mathcal{H})$, it is possible to rewrite the previous set of equations in a more elegant and compact form,

$$\frac{\partial \delta}{\partial \tau} + \boldsymbol{\nabla} \cdot \big[(1+\delta)\boldsymbol{u}\big] = 0 \tag{2.4}$$

$$\frac{\partial \boldsymbol{u}}{\partial \tau} + \mathcal{H}\boldsymbol{u} + (\boldsymbol{u} \cdot \boldsymbol{\nabla})\boldsymbol{u} = -\frac{\boldsymbol{\nabla} P}{\rho} - \boldsymbol{\nabla}\Phi \tag{2.5}$$

$$\nabla^2 \Phi = \frac{3}{2}\mathcal{H}^2 \Omega_m \delta, \tag{2.6}$$

where now $\rho(\boldsymbol{x}, \tau) = \bar{\rho}(\tau)[1 + \delta(\boldsymbol{x}, \tau)]$ defines the density contrast $\delta(\boldsymbol{x}, \tau)$, while $\boldsymbol{u}(\boldsymbol{x}, \tau)$ and $\Phi(\boldsymbol{x}, \tau)$ are respectively the peculiar velocity and gravitational field (the residuals after having subtracted the contribution of the Hubble flow to the total velocity and gravitational field).

Although the previous equations completely describe the time-evolution of the fluid at each wavelength, they are definitely hard to handle, given the presence of non-linear terms (like the one in the Euler equation). Nevertheless, the linear regime is defined only if the conditions $\|\boldsymbol{u}\| \ll c$ and $\delta \ll 1$ are satisfied, so let's assume these conditions. In this case, the fluid equations can be recast as

$$\frac{\partial \delta}{\partial \tau} + \boldsymbol{\nabla} \cdot \boldsymbol{u} = 0 \tag{2.7}$$

$$\frac{\partial \boldsymbol{u}}{\partial \tau} + \mathcal{H}\boldsymbol{u} = -\boldsymbol{\nabla}\Phi \tag{2.8}$$

$$\nabla^2 \Phi = \frac{3}{2}\mathcal{H}^2 \Omega_m \delta. \tag{2.9}$$

Note that here we have finally removed the pressure term in the Euler equation, since our first assumption was to consider a fluid made up exclusively by dark matter particles, for which $P = 0$. It is useful to express the velocity field $\boldsymbol{u}$ as the combination of a scalar and a vectorial field, $\psi_{\boldsymbol{u}}$ and $\boldsymbol{A_u}$, stately

$$\boldsymbol{u} = \boldsymbol{\nabla}\, \psi_{\boldsymbol{u}+\boldsymbol{\nabla}\times\boldsymbol{A_u}}, \tag{2.10}$$

so that $\psi_{\boldsymbol{u}}$ and $\boldsymbol{A_u}$ are responsible respectively for the coherent and chaotic motions. Indeed, invoking vector calculus identities, we can define the divergence and the vorticity of the velocity field as

$$\theta = \boldsymbol{\nabla} \cdot \boldsymbol{u} = \nabla^2 \psi_{\boldsymbol{u}} \tag{2.11}$$

$$\boldsymbol{w} = \boldsymbol{\nabla} \times \boldsymbol{u} = -\nabla^2 \boldsymbol{A_u} + \nabla(\nabla \cdot \boldsymbol{A_u}). \tag{2.12}$$

At large separations, well inside the linear regime, the velocity field is mainly irrotational. For this reason, it follows that

$$\frac{\partial \delta}{\partial \tau} + \theta = 0 \tag{2.13}$$

$$\frac{\partial \theta}{\partial \tau} + \mathcal{H}\theta = -\nabla^2 \Phi \tag{2.14}$$

$$\nabla^2 \Phi = \frac{3}{2}\mathcal{H}^2 \Omega_m \delta. \tag{2.15}$$

where now the second equation has been replaced by its divergence. Combining together the three equations, we finally get to a second order differential equation that describes the growth of density fluctuations with time,

$$\frac{\partial^2 \delta}{\partial \tau^2} + \mathcal{H}\frac{\partial \delta}{\partial \tau} - \frac{3}{2}\mathcal{H}^2 \Omega_m \delta = 0. \tag{2.16}$$

As one can immediately recognize, the growth of a density perturbation is described by the dynamical balance between a gravitational source (third term in Equation (2.16)) and a friction induced by the stretching of the space-time (second term in Equation (2.16)).

As it was remarked at the beginning of this section, the advantage of assuming linear theory is that this equation can be solved analytically (under precise conditions; in this work only when assuming an EdS universe). In detail, it is possible to look for factorised solutions, $\delta(\boldsymbol{x}, \tau) = D(\tau)A(\boldsymbol{x})$, where D is commonly referred to as the linear growth factor. Thus, Equation (2.16) turns into

$$\frac{d^2 D}{d\tau^2} + \mathcal{H}\frac{dD}{d\tau} - \frac{3}{2}\mathcal{H}^2 \Omega_m D = 0. \tag{2.17}$$

a) Einstein-de Sitter cosmology

As a reference case, we can assume an Einstein-de Sitter cosmology ($\Omega_m = 1$, $\Omega_\Lambda = \Omega_k = \Omega_\gamma = 0$). Actually, structures evolve for most of the time during the matter-dominated era, and thus, this approximation defines an optimal configuration for the description of the background cosmology. In this case, Equation (2.17) turns into

$$\frac{d^2D}{d\tau^2} + \mathcal{H}\frac{dD}{d\tau} - \frac{3}{2}\mathcal{H}^2 D = 0. \tag{2.18}$$

We search solutions with a power-law dependence on the scale factor, namely $D(a) = a^n$. Inserting this expression inside equation (2.18), we can find two different solutions, and more precisely

$$D_+(a) \propto a, \tag{2.19}$$
$$D_-(a) \propto a^{-3/2}. \tag{2.20}$$

Therefore we can write the general solution for the density contrast as a combination of the growing and decaying mode, D_+ and D_-,

$$\delta(\boldsymbol{x}, \tau) = A(\boldsymbol{x})a + B(\boldsymbol{x})a^{-3/2}. \tag{2.21}$$

Note that in an EdS universe, the growing mode D_+ goes like the scale factor a. The global effect of the expansion of the Universe is that density fluctuations do not grow exponentially with time but only as a power of the scale factor. We can rewrite this solution in a more compact form, that has the strong advantage of being valid also for the velocity divergence field. In detail, combining Equations (2.13), (2.14) and (2.15), we get to the following equations,

$$\frac{\partial\delta}{\partial\tau} + \theta = 0, \tag{2.22}$$
$$\frac{\partial\theta}{\partial\tau} + \mathcal{H}\theta = -\frac{3}{2}\mathcal{H}^2\delta. \tag{2.23}$$

Making the substitution $\theta = -\mathcal{H}\Theta$ and $\eta = \log a$ (for which it turns out that $\partial/\partial\tau = \mathcal{H}\partial/\partial\eta$), it follows that

$$\frac{\partial\delta}{\partial\eta} - \Theta = 0, \tag{2.24}$$
$$\frac{\partial\Theta}{\partial\eta} + \frac{1}{2}\Theta - \frac{3}{2}\delta = 0. \tag{2.25}$$

Now, we can define a new variable ψ that plays the role of both fields,

$$\psi_a = \begin{pmatrix} \delta \\ \Theta \end{pmatrix} \qquad a = 1, 2 \tag{2.26}$$

so that $\psi_1 = \delta$ and $\psi_2 = \Theta$. The previous set of equations can be recast in a single vectorial equation,

$$\frac{\partial \psi_a}{\partial \eta} + \Omega_{ab}\psi_b = 0, \tag{2.27}$$

with

$$\Omega_{ab} = \begin{pmatrix} 0 & -1 \\ -\frac{3}{2} & \frac{1}{2} \end{pmatrix}. \tag{2.28}$$

We remind here the definitions of direct and inverse Laplace transform respectively of a real- and complex-valued function,

$$\mathcal{L}[\psi(t)] = \tilde{\psi}(w) = \int_0^\infty e^{-wt}\psi(t)dt, \tag{2.29}$$

$$\mathcal{L}^{-1}[\tilde{\psi}(w)] = \psi(t) = \oint_{c-i\infty}^{c+i\infty} \frac{dw}{2\pi i} e^{wt}\tilde{\psi}(w). \tag{2.30}$$

Given that we want to apply these transformations to the vector equation in (2.27), we also need to know the transform of the derivative of a function, something that can be easily be proven (integral by parts) to yield

$$\mathcal{L}[\partial_t \psi(t)] = w\tilde{\psi}(w) - \phi, \tag{2.31}$$

where $\phi = \psi(t = 0)$ are the initial conditions of the system. We finally get to

$$w\tilde{\psi}_a(w) - \phi_a + \Omega_{ab}\tilde{\psi}_b(w) = 0, \tag{2.32}$$

that can be rewritten as

$$(w\delta_{ab} + \Omega_{ab})\tilde{\psi}_b(w) = \phi_a, \tag{2.33}$$

where δ_{ab} is the Kronecker delta function. The terms inside the round brackets in the previous equation is a matrix,

$$\sigma^{-1}_{ab}(w) = \begin{pmatrix} w & -1 \\ -\frac{3}{2} & \frac{1}{2} + w \end{pmatrix}, \tag{2.34}$$

that can be inverted as

$$\sigma_{ab}(w) = \frac{1}{(2w+3)(w-1)} \begin{pmatrix} 2w+1 & 2 \\ 3 & 2w \end{pmatrix}, \tag{2.35}$$

so that

$$\tilde{\psi}_a(w) = \sigma_{ab}(w)\phi_b. \tag{2.36}$$

We can switch from frequencies to time using Equation (2.30), and get to

$$\begin{aligned}\psi_a(\eta) &= \oint_{c-i\infty}^{c+i\infty} \frac{dw}{2\pi i} \frac{e^{wt}}{(2w+3)(w-1)} \begin{pmatrix} 2w+1 & 2 \\ 3 & 2w \end{pmatrix} \phi_b = \\ &= \left[\frac{e^{\eta}}{5} \begin{pmatrix} 3 & 2 \\ 3 & 2 \end{pmatrix} - \frac{e^{-3\eta/2}}{5} \begin{pmatrix} -2 & 2 \\ 3 & -3 \end{pmatrix} \right]_{ab} \phi_b, \end{aligned} \tag{2.37}$$

where the quantity inside the square brackets is named linear propagator and is denoted as $g_{ab}(a)$. In the end, we have that the linear solution for the density and velocity divergence field can be written simply as

$$\psi_a(a) = g_{ab}(a)\phi_b. \tag{2.38}$$

In this way, we can select the growing and decaying mode just by selecting some particular initial conditions, respectively $\binom{1}{1}$ and $\binom{1}{-3/2}$ or a combination of the two terms.

b) Flat ΛCDM cosmology

Now, we can briefly analyse the case of a flat ΛCDM universe with $\Omega_m < 1$ and $\Omega_m + \Omega_\Lambda = 1$. The growing and decaying modes now become

$$D_+(a) \sim \frac{5}{2} H_0^2 \Omega_{m,0} H(a) \int_0^a \frac{d\tilde{a}}{[\tilde{a}H(\tilde{a})]^3}, \tag{2.39}$$

$$D_-(a) \sim H(a), \tag{2.40}$$

and by consequence it is possible to obtain also in this case an expression of $\psi_a(\eta)$, although it is definitely more complex.

An important aspect of Equation (2.17), is that it can also be expressed in terms of the logarithmic derivative of the growing mode D_+, explicitly

$$f = \frac{d \log D_+}{d\eta}. \tag{2.41}$$

This quantity is referred to as the linear growth rate, and substituting this parameter inside Equation (2.17), it follows that

$$\frac{d^2 f}{d\eta^2} + \left[2 - \frac{9}{2}\Omega_m \right] \frac{d f}{d\eta} = 0. \tag{2.42}$$

Measuring the growth rate from a galaxy sample is essential to give constraint on gravity, and by consequence also on the underlying cosmological model.

We must remember that these results are valid only at very large separations, where the assumption of linear regime is reasonable enough. At intermediate and non-linear scales, the full power of non-linear perturbation theory must be invoked, still with no perfect outcomes. Nevertheless a linear approach is useful in the understanding of the basic equations to deal with, and also, set the stage for the introduction of the basic quantities that are commonly used in perturbation theory, like the linear growth factor D and the linear growth rate f.

2.1.2 Non-linear perturbation theory

In the previous section, we have assumed both the density contrast δ and the velocity divergence θ to be small, but we also have specified that this assumption is bound to fail as soon as we move to small scales and low redshifts. The general solution of the fluid equations, considering also the appearance of non-linear terms, can be expressed as

$$\delta_{NL} = \delta^{(1)} + \delta^{(2)} + \delta^{(3)} + ..., \tag{2.43}$$

where $\delta^{(k)} \sim \delta_L^k$ is a power of the linear solution obtained in the previous section.

In an Einstein-de Sitter cosmology, the new form of Equations (2.24) and (2.25), considering non-linear terms that now cannot be neglected, is as it follows,

$$\frac{\partial \delta}{\partial \eta} - \Theta = \nabla \cdot \big[\delta \boldsymbol{v}\big], \tag{2.44}$$

$$\frac{\partial \Theta}{\partial \eta} + \frac{1}{2}\Theta - \frac{3}{2}\delta = \nabla \cdot \big[(\boldsymbol{v} \cdot \nabla)\boldsymbol{v}\big], \tag{2.45}$$

where we have defined $\boldsymbol{v} = -\boldsymbol{u}/\mathcal{H}$. We can notice that the only difference with their linear counterparts is the appearance of quadratic terms at the right member of the equations. Now, it is more practical to work in Fourier space once non-linearities are taken into account. Using the definition of Fourier transform $\mathcal{F}$, and applying it to the right members of the previous equations, it can be proved that

$$\mathcal{F}\Big[\nabla \cdot \big[\delta \boldsymbol{v}\big]\Big] = \int d^3\boldsymbol{k}_1\, d^3\boldsymbol{k}_2\, \delta_D(\boldsymbol{k}_{12} - \boldsymbol{k}) \frac{\boldsymbol{k}_{12} \cdot \boldsymbol{k}_2}{k_2^2} \delta_{\boldsymbol{k}_1} \Theta_{\boldsymbol{k}_2} \tag{2.46}$$

$$\mathcal{F}\Big[\nabla \cdot \big[(\boldsymbol{v} \cdot \nabla)\boldsymbol{v}\big]\Big] = \int d^3\boldsymbol{k}_1\, d^3\boldsymbol{k}_2\, \delta_D(\boldsymbol{k}_{12} - \boldsymbol{k}) \frac{\boldsymbol{k}_1 \cdot \boldsymbol{k}_2}{2k_1^2 k_2^2} k_{12}^2 \Theta_{\boldsymbol{k}_1} \Theta_{\boldsymbol{k}_2}, \tag{2.47}$$

where $\delta_{\boldsymbol{k}}$ and $\Theta_{\boldsymbol{k}}$ are the Fourier transform of $\delta(\boldsymbol{x})$ and $\Theta(\boldsymbol{x})$, $\delta_D(\boldsymbol{k})$ is the Dirac delta centred in 0, and $\boldsymbol{k}_{12} = \boldsymbol{k}_1 + \boldsymbol{k}_2$ is the vectorial sum in Fourier space of $\boldsymbol{k}_1$ and $\boldsymbol{k}_2$.

Then, the equivalent of Equation (2.27) for the non-linear case can be written as

$$\frac{\partial \psi_a}{\partial \eta} + \Omega_{ab}\psi_b = \int d^3\boldsymbol{k}_1\, d^3\boldsymbol{k}_2\, \gamma_{abc}(\boldsymbol{k}, \boldsymbol{k}_1, \boldsymbol{k}_2)\psi_b(\boldsymbol{k}_1)\psi_c(\boldsymbol{k}_2), \tag{2.48}$$

where the only two non-zero elements γ_{abc} can be expressed as

$$\gamma_{112}(\boldsymbol{k}, \boldsymbol{k}_1, \boldsymbol{k}_2) = \frac{\boldsymbol{k}\cdot\boldsymbol{k_2}}{k_2^2}\delta_D(\boldsymbol{k} - \boldsymbol{k}_{12}), \tag{2.49}$$

$$\gamma_{222}(\boldsymbol{k}, \boldsymbol{k}_1, \boldsymbol{k}_2) = \frac{1}{2}\frac{k^2(\boldsymbol{k_1}\cdot\boldsymbol{k_2})}{k_1^2 k_2^2}\delta_D(\boldsymbol{k} - \boldsymbol{k}_{12}). \tag{2.50}$$

For the sake of clarity, we shall call

$$\alpha(\boldsymbol{k}_1, \boldsymbol{k}_2) = \frac{\boldsymbol{k}_{12}\cdot\boldsymbol{k_2}}{k_2^2}, \tag{2.51}$$

$$\beta(\boldsymbol{k}_1, \boldsymbol{k}_2) = \frac{1}{2}\frac{k_{12}^2(\boldsymbol{k_1}\cdot\boldsymbol{k_2})}{k_1^2 k_2^2}, \tag{2.52}$$

so that $\gamma_{112} = \alpha\delta_D$ and $\gamma_{222} = \beta\delta_D$. We look for solution of Equation (2.48) that can be written as

$$\psi_a(\boldsymbol{k}, \eta) = \sum_{n=1}^{\infty} a^n \psi_a^{(n)}(\boldsymbol{k}). \tag{2.53}$$

Inserting this expression inside Equation (2.48), and remembering that $\partial_\eta \psi_a = \sum_{n=1}^{\infty} n a^n \psi_a^{(n)}$, it follows that

$$\sum_{n=1}^{\infty} a^n \psi_a^{(n)}(n\delta_{ab} + \Omega_{ab}) = \int d^3\boldsymbol{k}_1\, d^3\boldsymbol{k}_2\, \gamma_{abc} \sum_{n=1}^{\infty} a^n \sum_{m=1}^{n-1} \psi_b^{(n-m)}\psi_c^{(m)}, \tag{2.54}$$

where the term inside the round brackets at the left member of the equation is the matrix already known as σ_{ab}^{-1}. We can freely separate the previous equation, since different orders on the left side corresponds to different orders on the right side, so that for a given order it follows

$$\psi_a^{(n)}(\boldsymbol{k}) = \sigma_{ab}(n) \int d^3\boldsymbol{k}_1\, d^3\boldsymbol{k}_2\, \gamma_{bcd}(\boldsymbol{k}, \boldsymbol{k}_1, \boldsymbol{k}_2) \sum_{m=1}^{(n-m)} \psi_c^{(n-m)}(\boldsymbol{k}_1)\psi_d^{(m)}(\boldsymbol{k}_2). \tag{2.55}$$

The most famous derivation is the one with $n = 2$, that clearly goes under the name of second order perturbation theory (2LPT). In this case, Equation (2.55) turns into

$$\psi_a^{(2)}(\boldsymbol{k}) = \sigma_{ab}(2) \int d^3\boldsymbol{k}_1\, d^3\boldsymbol{k}_2\, \gamma_{bcd}(\boldsymbol{k}, \boldsymbol{k}_1, \boldsymbol{k}_2)\psi_c^{(1)}(\boldsymbol{k}_1)\psi_d^{(1)}(\boldsymbol{k}_2), \tag{2.56}$$

where

$$\sigma_{ab}(2) = \frac{1}{7}\begin{pmatrix} 5 & 2 \\ 3 & 4 \end{pmatrix}. \tag{2.57}$$

It can be proved simply with calculations that, taking only the growing mode as initial conditions, the solution of this equation has the following form,

$$\psi_a^{(2)}(\boldsymbol{k}) = \int d^3\mathrm{k}_1\, d^3\boldsymbol{k}_2\, \delta_D(\boldsymbol{k} - \boldsymbol{k}_{12}) \begin{pmatrix} F_2(\boldsymbol{k}_1, \boldsymbol{k}_2) \\ G_2(\boldsymbol{k}_1, \boldsymbol{k}_2) \end{pmatrix} \delta_L(\boldsymbol{k}_1)\delta_L(\boldsymbol{k}_2), \tag{2.58}$$

where

$$F_2(\boldsymbol{k}_1, \boldsymbol{k}_2) = \frac{5}{7} + \frac{1}{2}\frac{\boldsymbol{k}_1 \cdot \boldsymbol{k}_2}{k_1 k_2}\left(\frac{k_1}{k_2} + \frac{k_2}{k_1}\right) + \frac{2}{7}\frac{(\boldsymbol{k}_1 \cdot \boldsymbol{k}_2)^2}{k_1^2 k_2^2}, \tag{2.59}$$

$$G_2(\boldsymbol{k}_1, \boldsymbol{k}_2) = \frac{3}{7} + \frac{1}{2}\frac{\boldsymbol{k}_1 \cdot \boldsymbol{k}_2}{k_1 k_2}\left(\frac{k_1}{k_2} + \frac{k_2}{k_1}\right) + \frac{4}{7}\frac{(\boldsymbol{k}_1 \cdot \boldsymbol{k}_2)^2}{k_1^2 k_2^2}, \tag{2.60}$$

are the second order kernels. The reason for having substituted Θ_L inside the integral with δ_L is easy: indeed, combining the definition of $\Theta = -\theta/\mathcal{H}$ with the continuity equation, it follows that $\Theta = \partial\delta/\partial(\log a) = a\delta_L = \delta$, and so the two quantities can be freely interchanged.

If instead of the growing mode only, we take a combination between growing and decaying modes, we obtain a solution that involves the linear propagator as for the linear case. For a ΛCDM cosmology, the kernels $F_2(\boldsymbol{k}_1, \boldsymbol{k}_2, \eta)$ and $G_2(\boldsymbol{k}_1, \boldsymbol{k}_2, \eta)$ become time-dependent and things get definitely more complex. In any case, it is still possible to obtain a compact solution as for the Einstein-de Sitter case, although in this case the corrections introduced respect to the linear theory are very small.

We do not explicitly show here results from higher order non-linear perturbation theory, given that the second order example can be considered a reference for all of them.

In addiction to the scheme depicted in this section, that commonly goes under the name of Eulerian perturbation theory, it is possible to make predictions on the growth of cosmological structures using the so-called Lagrangian perturbation theory. The main difference between the two approaches consists in the different quantity used to model the problem: in the first case,

we make use of scalar and vectorial fields (density, velocity, gravitational potential) and evaluate such fields at each points in the space-time; in the second case instead, we track the particle trajectories defining a quantity $\psi(\boldsymbol{q}, \tau)$ called displacement that identifies the position of the considered particle (whose initial position is $\boldsymbol{q}$) at the time τ.

2.2 Statistical description of the galaxy density field

The statistical description of the spatial distribution of galaxies can be achieved by considering the galaxy field as a stochastic process occurring in a three-dimensional space. This random field can be fully characterised employing multiple statistics able to catch the spatial correlations among its internal elements.

In this context, one of the most important statistics is provided by the two-point correlation function (2PCF), that is the autocovariance of the density field,

$$\xi(r) = \langle \delta(\boldsymbol{x}) \delta(\boldsymbol{x} + \boldsymbol{r}) \rangle, \tag{2.61}$$

where δ represents the density field of a generic proxy for the matter density field (matter particles, haloes, galaxies, clusters). In other words, the 2PCF can be defined as the excess probability of finding galaxy pairs at a given separation with respect to a random distribution (in this case $\xi(r) = 0$ by definition). Note how in Equation 2.61 the argument of the 2PCF is only the module r of the separation vector $\boldsymbol{r}$. This follows directly from the underlying assumption that the Universe is a homogeneous and isotropic random field.

Measuring the 2PCF can be a hard task, in particular using data collected within an irregular and pierced volume such in the case of the present galaxy surveys. For this reason, several estimators of the 2PCF have been realised during the years, that make the estimation of the two-point statistics more accessible. By definition, the 2PCF can be expressed as

$$\hat{\xi}_N(r) = \frac{GG(r)}{RR(r)} - 1. \tag{2.62}$$

Here, $GG(r)$ is the number of galaxy pairs separated by distance between $r - \Delta r$ and $r + \Delta r$, whereas $RR(r)$ is the number of pairs that would be expected if galaxies were randomly distributed in space (thus for a Poissonian distribution). The estimator in Equation (2.62) is commonly known as the *natural estimator*, since it comes out directly from the definition of the correlation function. Nowadays, more sophisticated estimators can be found

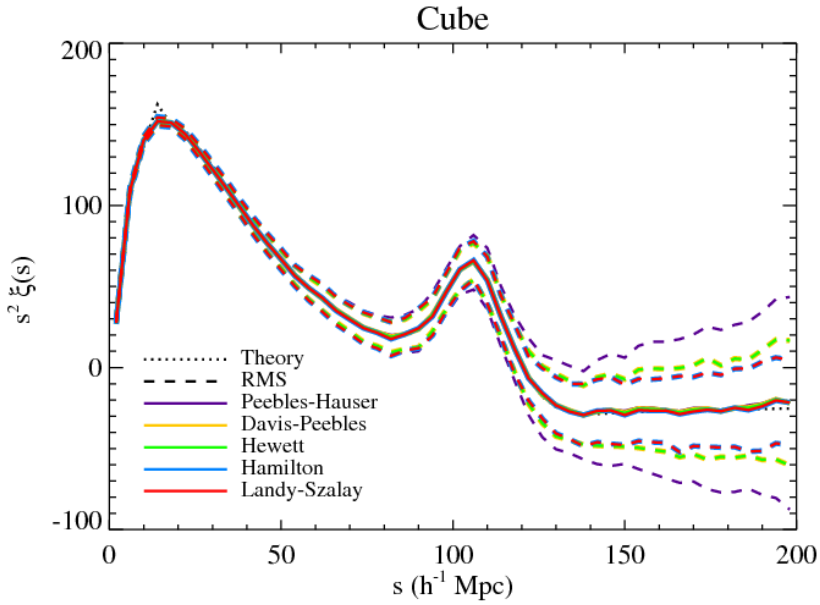

Figure 2.1: Comparison between the recovered correlation function using different estimators (solid lines), as found out in Vargas-Magaña et al. (2013). The fiducial signal is marked with a dotted line. Dashed lines show the rms for each kind of estimator.

in literature, that present both a higher accuracy and a smaller dependency on the random samples used for the estimation of $\xi(r)$. Below we propose a list of the most successful ones,

$$\text{Davis \& Peebles} \qquad \hat{\xi}_{DP}(r) = \frac{GG(r)}{GR(r)} - 1, \tag{2.63}$$

$$\text{Hewlett} \qquad \hat{\xi}_{He}(r) = \frac{GG(r) - GR(r)}{RR(r)}, \tag{2.64}$$

$$\text{Hamilton} \qquad \hat{\xi}_{Ha}(r) = \frac{GG(r)RR(r)}{GR^2(r)} - 1, \tag{2.65}$$

$$\text{Landy \& Szalay} \qquad \hat{\xi}_{LS}(r) = \frac{GG(r) - 2GR(r) + RR(r)}{RR(r)}. \tag{2.66}$$

Each of these estimators features the cross pairs $GR(r)$, thus reducing the dependency on the particular random sample used for the estimation of $\xi(r)$. In addiction, it has been proved (Kerscher et al. 2000; Vargas-Magaña et al. 2013) that the Landy-Szalay estimator is the one that minimizes the variance of the recovered correlation function nearly to the Poisson limit (the case when the only contribution to the total noise is given by the Poisson

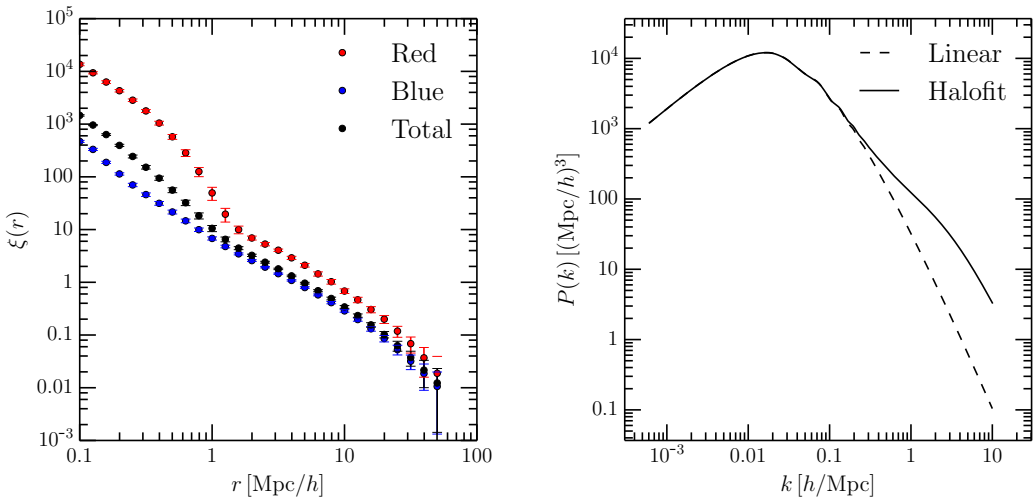

Figure 2.2: On the left: galaxy two-point correlation function extracted by the mean over 26 independent mock realizations of the VIPERS survey (W1 only in this case). Errorbars correspond to the errors on a single realization. Different colours represent different tracer, respectively red for red galaxies, blue for blue galaxies and black for the combined sample. On the right: prediction for the matter power spectrum at $z = 0.735$ computed with the Code for Anisotropies in the Microwave Background (CAMB). The dashed lines shows results for the linear theory, whereas the continuous line does shows the prediction from Halofit (empirical formula to add non-linearities).

component). This is the reason for why we are going to use this estimator rather than other ones during our analysis.

From a physical point of view, the two-point correlation function represents how large is the clustering amplitude of galaxies as a function of the comoving/physical scale: the higher the value of $\xi(r)$, the higher the probability of finding pairs and thus the intensity of the clustering. The left plot in Figure (2.2) shows an example of the two-point correlation function extracted from 26 mock realizations of the VIPERS galaxy sample, for different galaxy samples (red and blue galaxies). For historical reasons, it is common practice to describe the correlation function on scales below $10h^{-1}$Mpc with a power law,

$$\xi(r) = \left(\frac{r}{r_0}\right)^{-\gamma}, \tag{2.67}$$

with spectral index $\gamma \sim 2$ and correlation length $r_0 \approx 5\,h^{-1}\,\mathrm{Mpc}$. These values have to be taken carefully, since they are completely sensitive to the properties of the galaxy sample under examination (typically redder and brighter galaxies are more clustered than their bluer and fainter counterpart,

and therefore r_0 is higher for this class). The left plot of Figure (2.2) shows how much different γ and r_0 can be when measured using different tracer. In any case, the behaviour of the correlation function on scales above $10h^{-1}$Mpc diverges from the one of a power law, in the sense that it goes to 0 more rapidly than what Equation (2.67) would predict, and therefore, a power law description is considered as an echo from the past.

A definitely more robust method of describing the shape of the 2PCF is the so-called *halo model*. This theory posits that every galaxies form within a dark matter halo, and thus the clustering of galaxies must be a combination between the clustering of haloes themselves (which depends on the value of the cosmological parameters), and the way galaxies populate haloes, which depends on galaxy formation and evolution physics. The basic statistical variable of the halo model is the halo occupation number, that is the number of galaxies that are brighter than a given threshold hosted by an halo of a given mass. Galaxies inside a common halo are distributed in a central galaxy, lying at the center of the halo, and in satellite galaxies that trace the dark matter radial mass distribution. The latter follows with large accuracy a NFW profile (Navarro et al. 1997). In this model, the clustering of galaxies on scales larger than a typical halo ($\sim 1\,h^{-1}\,$Mpc) results from pairs of galaxies living in different haloes (two-halo term), whereas the clustering on smaller scales is due to pairs of galaxies within the same halo (one-halo term). In Figure 2.3, we show the fit of the SDSS measured correlation function using the halo fit model.

In order to obtain a good estimate of the two-point correlation function, one needs a reliable measurement of the spatial position of galaxies, that is, of their angular coordinates and redshifts. The latter cannot be easily measured but in spectroscopic redshift surveys (photometric surveys produce an error Δz_{phot} which is not negligible). Nevertheless, it is still possible to obtain constraints on the clustering of galaxies using only the angular distribution of galaxies on the sky (without considering the depth of the objects). The angular correlation function is defined as the excess probability of finding galaxy pairs with a given angular separation with respect to a random distribution, thus

$$w(\theta) = \frac{DD(\theta)}{RR(\theta)} - 1. \tag{2.68}$$

It can be found analytically that, if we assume $\xi(r)$ to be shaped as a power law, like in Equation (2.67), then the corresponding angular correlation function shall assume the following form,

$$w(\theta) = \left(\frac{\theta}{\theta_0}\right)^{-(\gamma-1)}. \tag{2.69}$$

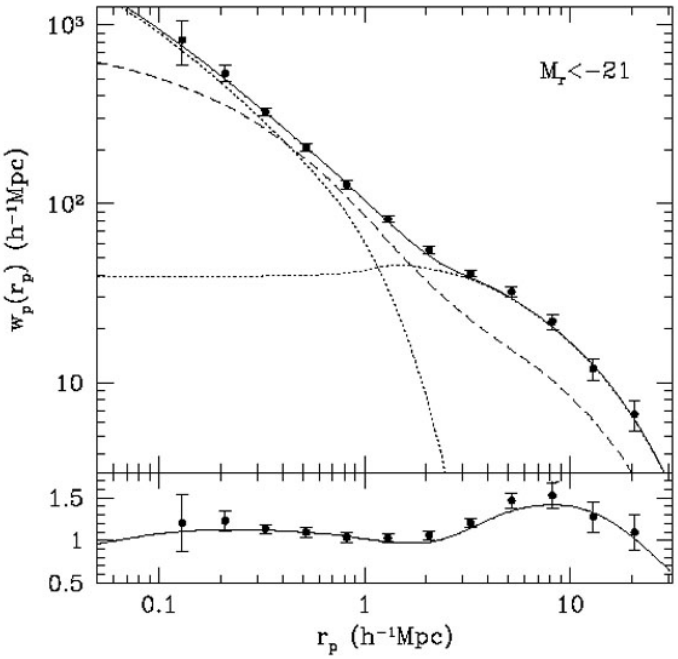

Figure 2.3: Example of the halo model fit of the projected 2PCF for a set of SDSS galaxies with $M_r < -21$ (Zehavi et al. 2004). The top panel shows data points with their relative errorbars, along with three different lines marking the assumed underlying matter 2PCF (dashed line) and the one- and two-halo term (dotted lines). The bottom panel shows the deviation of data points and best halo model fit from the best power law fit.

An other equivalent instrument used to quantify the clustering of galaxies and matter at different scales is the power spectrum of density fluctuations. Differently from the 2PCF, this object is defined in Fourier space (and therefore it is a function of the wave number k) as the autocovariance of the Fourier transforms of the density field. This yields

$$P(k) = \langle |\delta_{\mathbf{k}}|^2 \rangle, \tag{2.70}$$

where $\delta_{\mathbf{k}}$ is the Fourier transform of $\delta(\mathbf{x})$. From Equations (2.61) and (2.70), it follows that $\xi(r)$ and $P(k)$ are just a pair of Fourier conjugates, such that

$$\xi(r) = \frac{1}{(2\pi)^3} \int P(k) e^{i\mathbf{k}\cdot\mathbf{r}} d^3\mathbf{k}. \tag{2.71}$$

By expanding the scalar product at the exponent of Equation (2.71), it follows that

$$\xi(r) = \frac{1}{2\pi^2} \int_0^\infty k^3 P(k) \frac{\sin(kr)}{kr} d\log k = \int_0^\infty \Delta^2(k) \frac{\sin(kr)}{kr} d\log k, \tag{2.72}$$

where

$$\Delta^2(k) \equiv \frac{k^3}{2\pi^2} P(k) \tag{2.73}$$

is the dimensionless power spectrum. The right panel of Figure (2.2) shows the example of a matter power spectrum computed by a Boltzmann code (CAMB in this case) assuming a Planck-like ΛCDM cosmology. The dashed and continuous line represent respectively the linear and Halofit (non-linear, based on fits to simulations) prediction of $P(k)$.

The shape of the linear power spectrum features two power laws respectively below and above a particular scale, intuitively called *turnaround*, that corresponds to the horizon scale at the time of the equivalence between radiation and matter. This happens because of the combined effect generated by non baryonic matter and radiative pressure, that prevents fluctuations on scales smaller than the horizon to freely grow to form bound structures. At the equivalence, matter starts to dominate the energetic budget of the Universe, and baryons can finally fall within the potential wells that dark matter has created in the meantime. Before this epoch, baryons feel the attraction of dark matter, but at the same time, being electromagnetically coupled to photons, feel also the pressure generated by photons. This combined effect make baryonic matter to experience oscillations, that are called *baryon acoustic oscillations* (BAO) (see Figure (2.5)). The trace of these oscillations can be found both in the power spectrum (as periodic oscillations above the turnaround scale) and in the 2PCF (as a sharp peak at $\sim 100\,h^{-1}\,\mathrm{Mpc}$). The resulting linear solution for a ΛCDM cosmology assumes the following shape,

$$P(k,z) \propto A_s \frac{D^2(z)}{H_0^4 \Omega_{m,0}^2} k \left(\frac{k}{k_p}\right)^{n_s - 1} T^2(k), \tag{2.74}$$

where A_s is the scalar amplitude, $D(z)$ is the linear growth factor, $\Omega_{m,0}$ is the matter density parameter, n_s is the spectral tilt and $T(k)$ is the linear transfer function. From this equation, it is clear how the linear spectrum evolves differently not only as a function of time (through $D(z)$) but also differently at different wave number k (through the transfer function). The spectral tilt n_s is slightly smaller than 1, a result that is predicted if one assumes a phase of inflationary expansion in the very early stages of the Universe. With the exception of this term and of the transfer function, the only dependence of the linear spectrum on k is just

$$P(k) \propto k, \tag{2.75}$$

something that should describe quite well the shape of the spectrum right after inflation, and the left branch of the current spectrum. The spectrum written in this way is usually referred to as the Harrison-Zel'dovich spectrum.

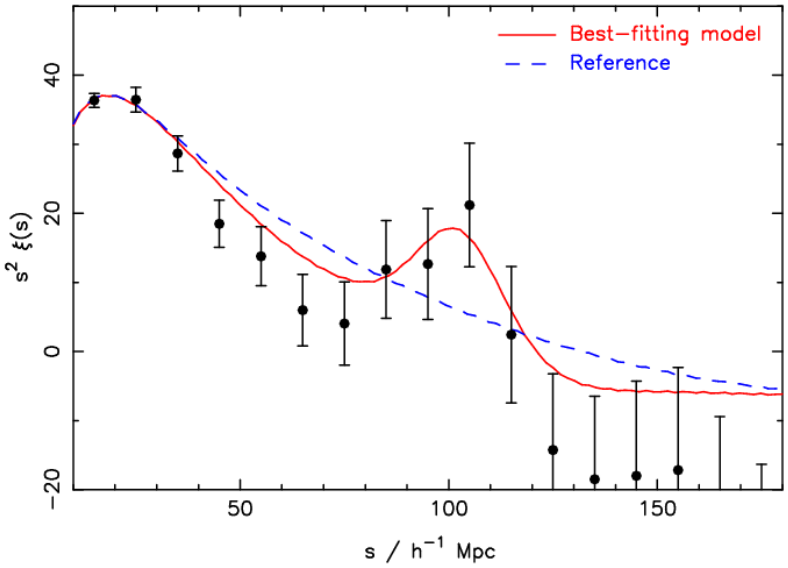

Figure 2.4: Measurement of the two-point correlation function from the WiggleZ survey (Blake et al. 2011). Data points are compared with the best-fitting model including baryon acoustic oscillations (red curve), that are represented by the sharp peak at $s \sim 100\mathrm{Mpc}/h$. The dashed blue curve represents a baryon free reference model.

The non-linear power spectrum can be approximated with the linear spectrum on sufficiently large scales, but starts to deviate significantly from the linear solution as long as it enters the non-linear regime. A precise description of the non-linear regime cannot be fulfilled, but with the support of N-body simulations. However, current predictions of perturbation theory can provide a sufficiently accurate prediction of the non-linear matter power spectrum up to $k_{max} \sim 0.3h/\mathrm{Mpc}$. Adding galaxies clearly makes everything more difficult, since we also must consider the relation between the matter and the galaxy density field (see next section).

A fundamental quantity used in cosmology is the variance of the density field, defined as

$$\sigma^2(R) \equiv \langle \delta^2(\boldsymbol{r}, R) \rangle = \int \Delta^2(k) \tilde{W}^2(kR) d\log k, \tag{2.76}$$

where $\delta(\boldsymbol{r}, R)$ is the density field smoothed on a scale R and $\tilde{W}(kR)$ is the smoothing window function in Fourier space. One of the most employed window function is the top-hat configuration, that is

$$W_{th}(\boldsymbol{r}, R) = \left(\frac{4\pi}{3} R^3\right)^{-1} \begin{cases} 1 & r \leq R \\ 0 & r > R \end{cases}, \tag{2.77}$$

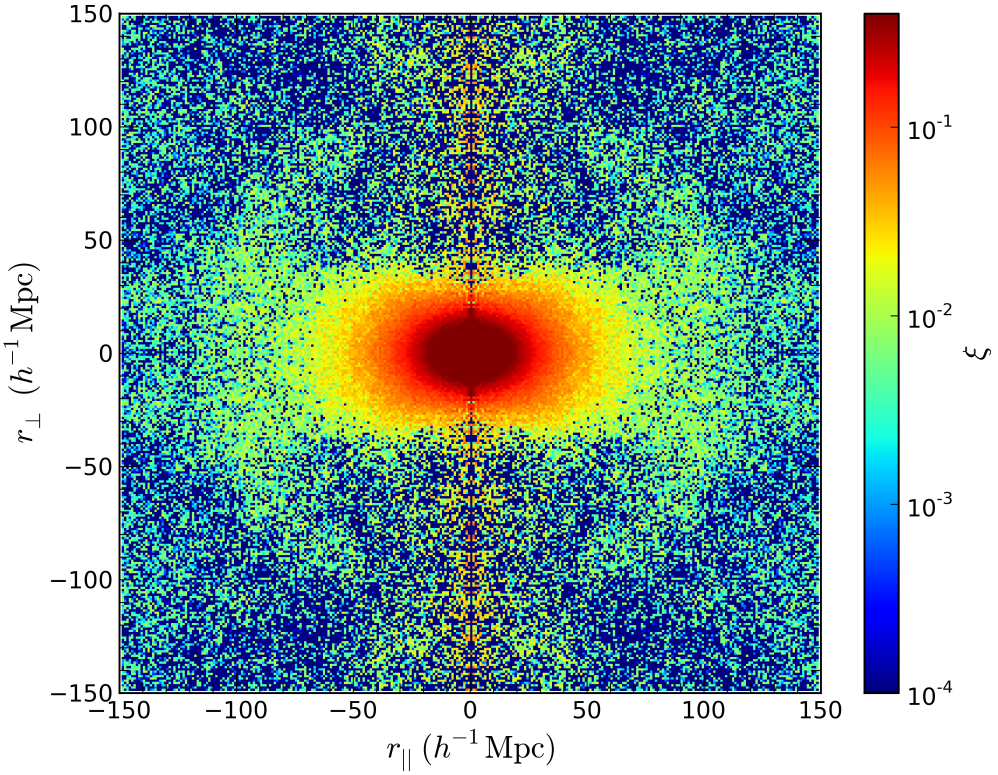

Figure 2.5: Two-point correlation function measured from the BOSS survey (Samushia et al. 2013). In this case the signal is deprojected along the direction orthogonal (x axis) and along the line of sight (y axis). The BAO ring is clearly visible surrounding the central feature. The anisotropies visible in the inner regions are produced by galaxy peculiar velocities, as explained in Section 2.4.

which basically is 1 within a sphere of radius R and 0 outside. Clearly the value of $\sigma(R)$ will change significantly for different values of R, to the limit of $\sigma(R) \to 0$ for $R \to \infty$ (this is a consequence of the cosmological principle). For historical reason, the amount of non-linearities of the matter power spectrum is typically quantified as the variance of the density field smoothed with a top-hat window function of radius $R = 8\,h^{-1}\,\mathrm{Mpc}$, and thus the name σ_8. This quantity is a crucial cosmological parameter which has a big influence over the growth of fluctuations in the early universe. The current analyses lead to values of σ_8 that are consistent with ~ 0.8 at $z = 0$. In simple words, we can identify σ_8 as a normalisation for the amplitude of the matter power spectrum. Its usefulness will become transparent in the following chapters.

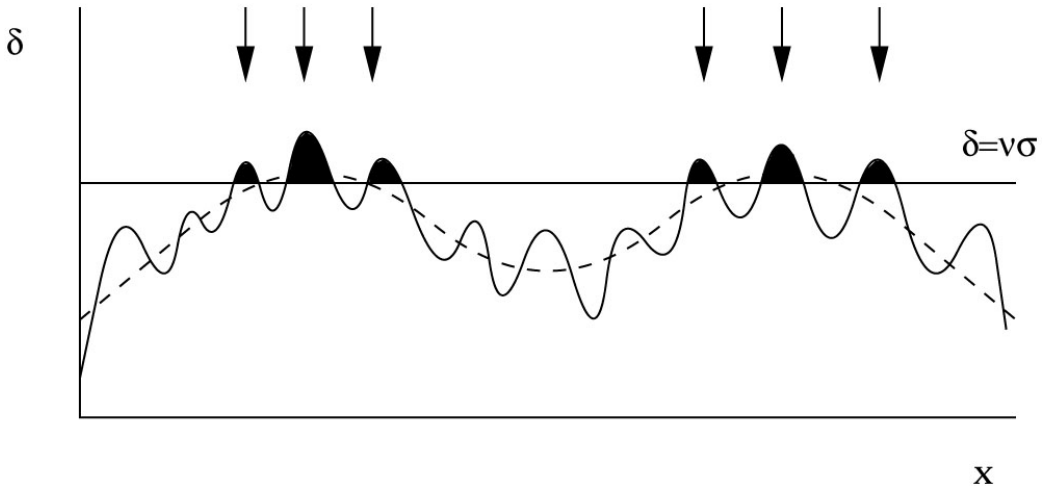

Figure 2.6: One-dimensional sketch of the critical threshold required to produce a collapsed structure. The curve black line represents a reference one-dimensional density field, whereas the straight horizontal line mark the threshold for the formation of structures. Galaxies form only within the regions whose local density is larger than the threshold (black regions).

2.3 Galaxy bias

The previous section has dealt with the properties of the dark matter density field, with no reference to the real observable, i.e. galaxies. Actually, the galaxy density field can be a non-local, non-linear and stochastic function of the underlying matter density. This galaxy biasing is the product of several physical processes, mostly involving the physics of galaxy formation. The result is that the distribution of baryons differ from the one of dark matter, with galaxies being concentrated in the peaks of the matter distribution (see Figures (2.6) and (2.7)). For this reason, any model of matter clustering must take into account how galaxies trace the matter density field.

The original concept of galaxy bias was introduced by Kaiser (Kaiser 1984) in order to reconcile the different clustering length of galaxies and rich clusters. As a matter of fact, being mostly rare objects that form above a very high density threshold, the latter exhibit a larger clustering amplitude. This idea was subsequently developed in parallel analysis (Mo et al. 1996), showing that the bias of haloes is strongly dependent on the halo mass and on the epoch of formation (massive and old haloes are more biased than their small and young counterparts).

Stochasticity appears to have a small impact on the galaxy distribution, except for adding an extra variance term, whereas it is possible to avoid at first order the assumption of non-local bias by smoothing the density field on

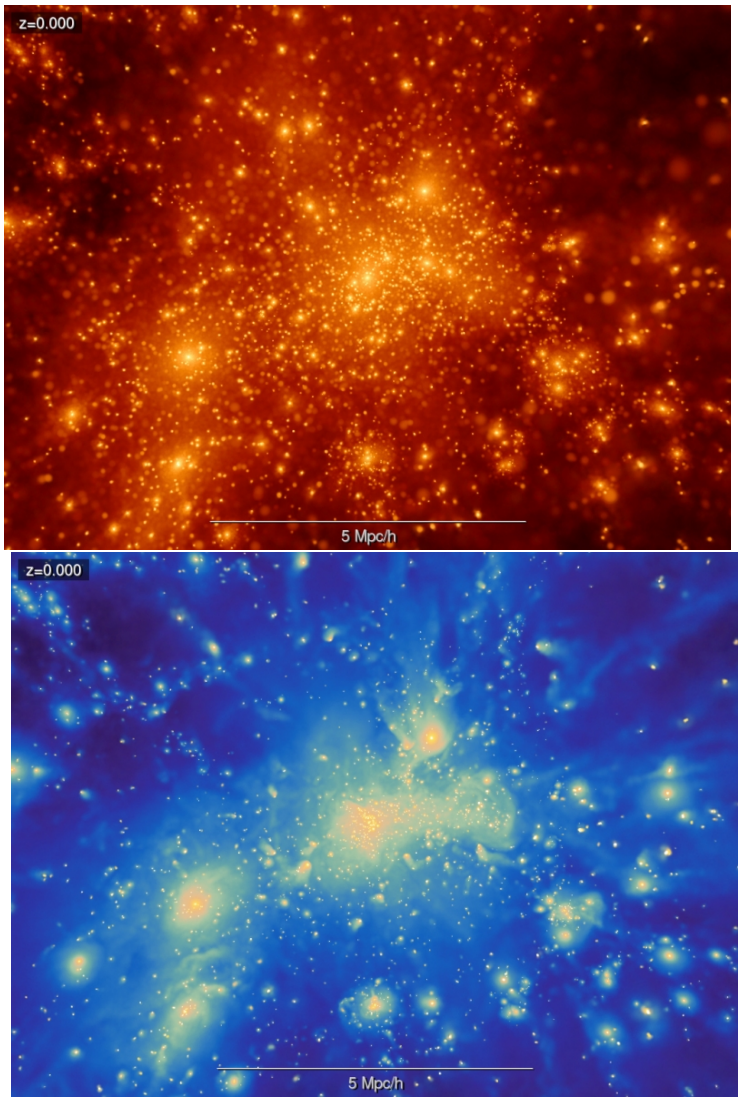

Figure 2.7: Particle distribution inside a 10Mpc box in a snapshot at $z = 0$ of the MDR1 dark matter simulation. The top and bottom panels show respectively the distribution of dark matter and baryonic particles. A quick comparison between the two distributions make visible how baryons (and by consequence galaxies) are only a limited proxy of the matter density field.

large enough scales. As for the non-linearity, things are definitely worse, since there is not yet a complete scheme depicting the behaviour of baryons inside the strong non-linear regions. Focusing on the largest scales has become common practice in the scientific analysis (see Desjacques et al. (2016) for a review on galaxy bias on quasi-linear scales). In this case, it is fair to assume the galaxy density contrast δ_g to be a linear function of the matter density contrast δ_m and to define the linear bias b as

$$\delta_g(\boldsymbol{x}) = b\,\delta_m(\boldsymbol{x}). \tag{2.78}$$

Representing how a particular galaxy sample is tracing the underlying matter distribution, the galaxy bias is strongly dependent on the intrinsic characteristics of the sample, like luminosity, colour, morphology and age. In terms of two-point statistics, and following Equation (2.61), the linear bias can be defined as

$$b = \left(\frac{\xi_g}{\xi_m}\right)^{1/2} = \left(\frac{P_g}{P_m}\right)^{1/2}, \tag{2.79}$$

and can be directly measured on linear scales (where this ratio is found to be approximately constant).

If one wishes to extend this model also including non-linear effects, then it is possible to rewrite equation 2.78 as it follows,

$$\delta_g = b_1\delta_m + \frac{b_2}{2!}\delta_m^2 + \frac{b_3}{3!}\delta_m^3 + ... = \sum_{k=0}^{\infty}\frac{b_k}{k!}\delta_m^k, \tag{2.80}$$

where now b_1, b_2, b_3, ..., b_k are the coefficients of the Taylor expansion of the galaxy density field around the underlying matter density field. A classical non-linear bias including analysis assumes the first two terms of the expansion (first and second order) to be free parameters, while fixing all the higher order terms to be zero.

If one also wishes to consider the non-local nature of the bias, then the number of parameters increases. In this analysis, we will consider only local bias (either linear and non-linear). For this reason, any deviation from Equation (2.80) will be neglected. An interesting and deep analysis on the concepts of non-linear and non-local galaxy bias can be found in Chan et al. (2012), where they propose the following model,

$$\delta_g = b_1\delta_m + \frac{b_2}{2!}\delta_m^2 + \gamma_2\mathcal{G}_2 + \gamma_3^-\mathcal{G}_3 + ... \tag{2.81}$$

Here $\mathcal{G}_2$, $\mathcal{G}_3$ are just operators involving the density and velocity potentials, whereas γ_2, γ_3^- are additional free parameter that can be either fixed (assuming local bias instance) or let free. For a practical use of this model, we refer to Sanchez et al. (2016).

2.4 Redshift-space distortions

Given a particular cosmological model and using Equation (1.16) with the correct values of the density parameters, it is possible to reconstruct the spatial distribution of galaxies starting from their measured redshifts. However, redshift-inferred distances are not perfect proxies of the galaxy true positions. Indeed, in addiction to the Hubble flow, galaxies do possess peculiar velocities, that are generated from the gravitational interactions with the local environment. This extra-contribution to the velocity field must be added up to the cosmological expansion, and its main effect to the measured redshifts can be modelled as a Doppler shift,

$$z_{\rm obs} = z_{\rm cosmo} + z_{\rm pec} \tag{2.82}$$

that alters the distribution of galaxies along the line of sight (see Harrison (1974) for a complete derivation of the previous formula). These displacements lead to the apparent distortion of the pattern of galaxy clustering in redshift space, compared to the one that would be obtained in real space, using only the cosmological contribution $z_{\rm cosmo}$. Although such distortions complicate the interpretation of the observed galaxy density field, they have the tremendous advantage of bearing information about the dynamics of galaxies, and by consequence about the gravitational field in which they are embedded. One of the most important potential goal of redshift-space distortions is the understanding of the accelerated expansion of the Universe. As a matter of fact, the acceleration can be explained either invoking an additional energy component (ΛCDM) or reformulating the laws of gravity on cosmological scales (modified gravity). Being sensitive only to gravity, redshift-space distortions could eventually lift this degeneracy and help to discriminate among different cosmological models. Hereafter I will briefly recap the most important step in the theoretical description of RSD, focusing on both giving a physical motivation to the obtained results and empirically understand the effects of RSD on the shape of two-point correlation function.

The analogous of Equation (2.82) using comoving distances can be recast in the following way,

$$\boldsymbol{s} = \boldsymbol{r} + \frac{v_{\parallel}(\boldsymbol{r})\hat{\boldsymbol{e}}_{\parallel}}{aH(a)}, \tag{2.83}$$

where $\boldsymbol{r}$ and $\boldsymbol{s}$ are the positions in real- and redshift-space, $\hat{\boldsymbol{e}}_{\parallel}$ is the unit vector along the line of sight, and $v_{\parallel}$ is the component of the galaxy peculiar velocity along the line of sight (projected onto $\hat{\boldsymbol{e}}_{\parallel}$). In Figure 2.8 we show the visual effect of adding RSD to a simulated galaxy dataset.

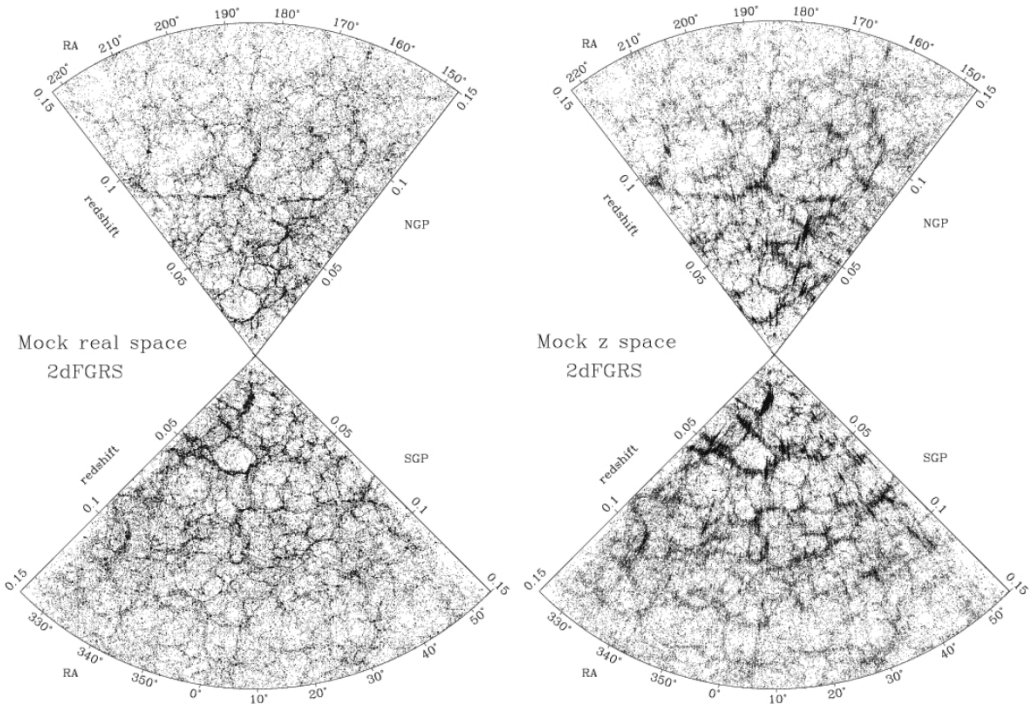

Figure 2.8: Galaxy distribution within a RA-z cone diagram from a mock catalogue of the 2dFGRS. On the left: real-space. On the right: redshift-space. Although the large-scale structures are the same between the two samples, along the line of sight we can distinguish a flattening of the largest structures (Kaiser effect) and a stretching of the smallest ones (Fingers of God).

Invoking mass conservation, the redshift-space density field $\delta^s(\boldsymbol{s})$ can be expressed as a function of its real-space counterpart $\delta(\boldsymbol{r})$ as

$$\delta^s(\boldsymbol{s}) = [1 + \delta(\boldsymbol{r})] \left| \frac{d^3\boldsymbol{s}}{d^3\boldsymbol{r}} \right|^{-1} - 1. \tag{2.84}$$

A common assumption is to work in the plane-parallel approximation, with the largest probed separations much smaller than the distance from the observer to the sources. In this case, it is fair to assume the line of sight to different objects to be the same and the Jacobian of the transformation assumes the simple form of

$$\left| \frac{d^3\boldsymbol{s}}{d^3\boldsymbol{r}} \right| = 1 - f\partial_\parallel u_\parallel, \tag{2.85}$$

where the renormalized velocity is defined as $u_\parallel(\boldsymbol{r}) = -v_\parallel(\boldsymbol{r})/[faH(a)]$. In the hypothesis of a perfectly irrotational velocity field (Bernardeau et al.

2002), we can define the velocity divergence as $\theta(\boldsymbol{r}) = \nabla \cdot \boldsymbol{v}(\boldsymbol{r})$ and equation (2.84) can be written as

$$\delta^s(\boldsymbol{s}) = \left[\delta(\boldsymbol{r}) + f\partial_\parallel^2 \Delta^{-1}\theta(\boldsymbol{r})\right]\left[1 - f\partial_\parallel^2 \Delta^{-1}\theta(\boldsymbol{r})\right]^{-1}, \tag{2.86}$$

with Δ denoting the Laplace operator. In Fourier space, the operator in the equation above assumes a more simplified appearance, namely $\partial_\parallel^2 \Delta^{-1} = (k_\parallel/k)^2 = \mu^2$, where μ is but the cosinus of the angle between the wave vector $\boldsymbol{k}$ and the line of sight. Substituting this expression inside Equation (2.86) and taking its Fourier transform, one finally obtains

$$\delta^s(k,\mu) = \int \frac{d^3\boldsymbol{s}}{(2\pi)^3} e^{-i\boldsymbol{k}\cdot\boldsymbol{s}} \delta^s(\boldsymbol{s}) = \int \frac{d^3\boldsymbol{r}}{(2\pi)^3} e^{-i\boldsymbol{k}\cdot\boldsymbol{r}} e^{-ik\mu f u_\parallel} \left[\delta(\boldsymbol{x}) + \mu^2 f\theta(\boldsymbol{x})\right]. \tag{2.87}$$

Using the definition of Equation (2.70), the redshift-space power spectrum assumes the following form (Scoccimarro et al. 1999),

$$P^s(k,\mu) = \int \frac{d^3\boldsymbol{r}}{(2\pi)^3} e^{-i\boldsymbol{k}\cdot\boldsymbol{r}} \left\langle e^{-ik\mu f \Delta u_\parallel} \times \left[\delta(\boldsymbol{x}) + \mu^2 f\theta(\boldsymbol{x})\right]\left[\delta(\boldsymbol{x'}) + \mu^2 f\theta(\boldsymbol{x'})\right] \right\rangle, \tag{2.88}$$

with $\Delta u_\parallel = u_\parallel(\boldsymbol{x}) - u_\parallel(\boldsymbol{x'})$ and $\boldsymbol{r} = \boldsymbol{x} - \boldsymbol{x'}$. If we reomve the rather strong assumption of working with an irrotational velocity field (that is no more valid as long as smaller scales are included) than Equation (2.88) turns into

$$P^s(k,\mu) = \int \frac{d^3\boldsymbol{r}}{(2\pi)^3} e^{-i\boldsymbol{k}\cdot\boldsymbol{r}} \left\langle e^{-ik\mu f \Delta u_\parallel} \times \left[\delta(\boldsymbol{x}) + f\partial_\parallel u_\parallel\right]\left[\delta(\boldsymbol{x'}) + f\partial_\parallel u_\parallel\right] \right\rangle. \tag{2.89}$$

This last equation completely describes the anisotropies of the clustering of matter at each separation, with the only assumption of working in the plane-parallel approximation. As one can notice, redshift-space distortions depend both on the non-linear density and the velocity field.

At first, it is possible to identify two main regimes within which distortions occur in a well-defined fashion. At large separations, matter tends to follow coherent motions towards overdense regions and velocities are thus responsible for the enhancement of clustering. In this linear regime, the density and velocity fields are strictly correlated, up to the limiting case given by the linear theory in which $\delta = \Theta$ (as it is explained in the previous sections). This first kind of distortions commonly goes under the name of *Kaiser effect*, and it is basically produced by the terms inside the square brackets inside Equation (2.88).

On the contrary, at the scales of galaxy clusters, structures are capable of reaching thermal equilibrium. This means that the dynamics inside these

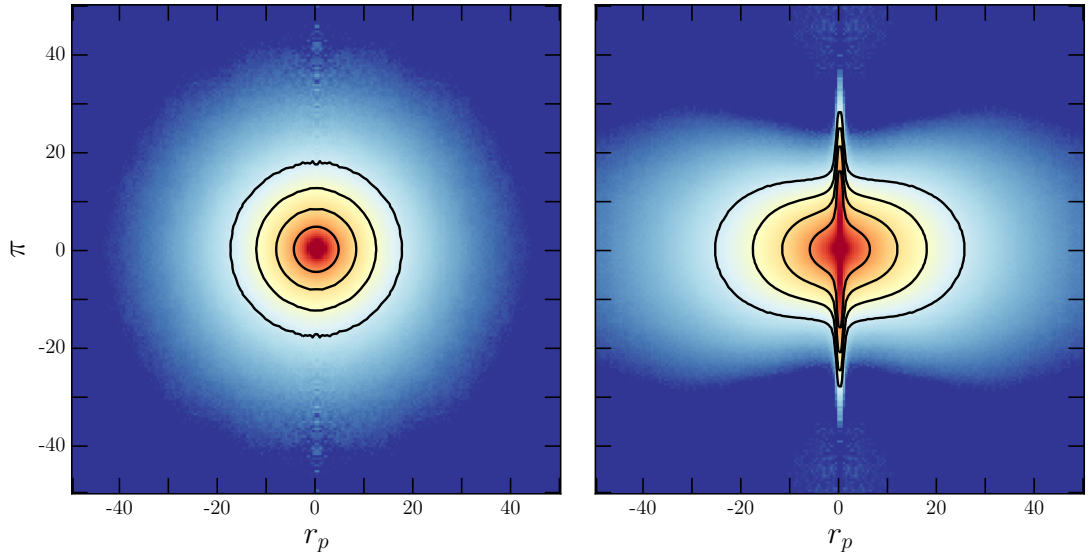

Figure 2.9: Comparison between the two-dimensional correlation function measured in real- (on the left) and redshift-space (on the right). Measurements have been realised averaging a sample of 300 mock realizations in order to reduce the noise. The expected pattern of the anisotropic 2PCF appears clearly when adding peculiar velocities to infer distances. On the contrary, real-space clustering has no privileged direction. Black lines denote iso-correlation curves $(1, 0.4, 0.2, 0.1$ from the inner to the outer line).

virialized regions is mainly driven by an isotropic velocity field, with no preferred direction. In this case, the apparent clustering rate is smaller than the true one, and structures look stretched along the line of sight. In literature, this effect has earned the peculiar name of *Fingers of God* (Jackson 1972).

The previous distortions are directly observed and quantified using the two-point correlation function and deprojecting it along the directions parallel and orthogonal to the line of sight. As a matter of fact, Equation (2.82) shows how the distortions induced by peculiar velocities are concentrated only along the observer line of sight. With this purpose in mind, it is necessary to explicitly define these directions using two new coordinates. Namely, if $\boldsymbol{s_1}$ and $\boldsymbol{s_2}$ are two positions in redshift-space, we can define the separation vector and the mean position respectively as $\boldsymbol{s_{12}} = \boldsymbol{s_1} - \boldsymbol{s_2}$ and $\boldsymbol{m} = (\boldsymbol{s_1} + \boldsymbol{s_2})/2$, and consequently the separations parallel and orthogonal to the line of sight,

$$\pi = \frac{\boldsymbol{s_{12}} \cdot \boldsymbol{m}}{|\boldsymbol{s_{12}}|} \tag{2.90}$$

$$r_p = \boldsymbol{s_{12}} \cdot \boldsymbol{s_{12}} - \pi^2. \tag{2.91}$$

Figure 2.9 shows a comparison between the expected pattern of the two-point

correlation function in real- and redshift-space once it has been deprojected along r_p and π. The main effects of peculiar velocities are represented by the flattening of the iso-correlation curves at large separations on the sky (the Kaiser effect), and by the apparent stretching of the radial dimension of structures on the scales of galaxy clusters and dark matter haloes (the Fingers of God).

Although Equation (2.88) is based on the only assumption of working in the plane-parallel approximation, and thus represents a complete description of the distortions induced by peculiar velocities in redshift-space, its practical implementation is something difficult to realize, mainly because literature has not been able yet to provide a trustful model for the velocity field and for its dispersion at non-linear separations (something that enters in the exponential prefactor inside Equation (2.88)). For this reason, approximations with simpler and more transparent models are in some sense fostered at the expense of losing part of the true physics behind the clustering process in redshift-space.

The model developed by Kaiser in 1987 is based on the assumption of completely linear regime, for which the amplitude of the velocity dispersion becomes negligible (at large separations the velocity field is perfectly coherent and points towards the bulk of the density field). In addiction, using the continuity equation in (2.13), it is possible to identify the velocity field with the density field itself. These assumptions lead to the following model for the redshift-space power spectrum,

$$P^s(k,\mu) = \left[1 + f\mu^2\right]^2 P(k), \tag{2.92}$$

where $P(k)$ is just its isotropic real-space counterpart. In the case of galaxy clustering, and with the assumption of linear bias, it is possible to substitute the linear growth rate f with the distortion parameter defined as $\beta = f/b$, so that Equation (2.92) turns into

$$P_g^s(k,\mu) = \left[1 + \beta\mu^2\right]^2 P_g(k), \tag{2.93}$$

where now, P_g is the galaxy power spectrum. In general, it is possible to expand $P^s(k,\mu)$ in harmonics of μ, such that

$$P^s(k,\mu) = \sum_l P_l^s(k)\mathcal{L}_l(\mu), \tag{2.94}$$

where $\mathcal{L}_l$ are the Legendre polynomials and

$$P_l^s(k) = \frac{2l+1}{2}\int_{-1}^{+1} P^s(k,\mu)\mathcal{L}_l(\mu)d\mu \tag{2.95}$$

are the multipoles of the expansion. In real space, the only term of this expansion is $P_0(k) = P(k)$ (implying isotropy). Given that redshift distortions act in a way that only the absolute value of μ matters, and since the odd terms of the Legendre polynomials are odd functions, the odd multipoles $P_1^s(k)$, $P_3^s(k)$, ... are all zero. In addiction, if linear theory is assumed (and thus the Kaiser model), the only non-zero contributions are the first three even terms, $P_0^s(k)$, $P_2^s(k)$ and $P_4^s(k)$. Following the definition given in Equation (2.95), we can analytically predict the shapes of these functions as

$$P_0^s(k) = \left(1 + \frac{2}{3}\beta + \frac{1}{5}\beta^2\right)P(k), \tag{2.96}$$

$$P_2^s(k) = \left(\frac{4}{3}\beta + \frac{4}{7}\beta^2\right)P(k), \tag{2.97}$$

$$P_4^s(k) = \frac{8}{35}\beta^2 P(k). \tag{2.98}$$

The transposition of the linear theory in configuration space can be found in Hamilton (1992). Basically, in this case, the redshift-space two-point correlation function can be written as

$$\xi^s(s,\mu) = \xi_0^s(s)\mathcal{L}_0(\mu) + \xi_2^s(s)\mathcal{L}_2(\mu) + \xi_4^s(s)\mathcal{L}_4(\mu). \tag{2.99}$$

In the previous equation, the terms of the expansion are

$$\xi_0^s(s,\mu) = \left(1 + \frac{2}{3}\beta + \frac{1}{5}\beta^2\right)\xi(s), \tag{2.100}$$

$$\xi_2^s(s,\mu) = \left(\frac{4}{3}\beta + \frac{4}{7}\beta^2\right)\left[\xi(s) - \frac{3J_3(s)}{s^3}\right], \tag{2.101}$$

$$\xi_4^s(s,\mu) = \frac{8}{35}\beta^2\left[\xi(s) + \frac{15}{2}\frac{J_3(s)}{s^3} - \frac{35}{2}\frac{J_5(s)}{s^5}\right], \tag{2.102}$$

where $\xi(s = r)$ is the real-space correlation function and J_l is defined as its integral functions,

$$J_l(x) = \int_0^x \xi(y)y^{l-1}dy. \tag{2.103}$$

The global effect of RSD on the monopole ξ_0^s is shown in Figure 2.10.

In order to partially recover the stretching effect in the non-linear regime, it is possible to model both the redshift-space power spectrum and correlation function adding a phenomenological damping factor that plays the role of a pairwise velocity distribution, and thus mimicking the effect of the exponential prefactor inside Equation 2.88. This is the idea at the basis of the

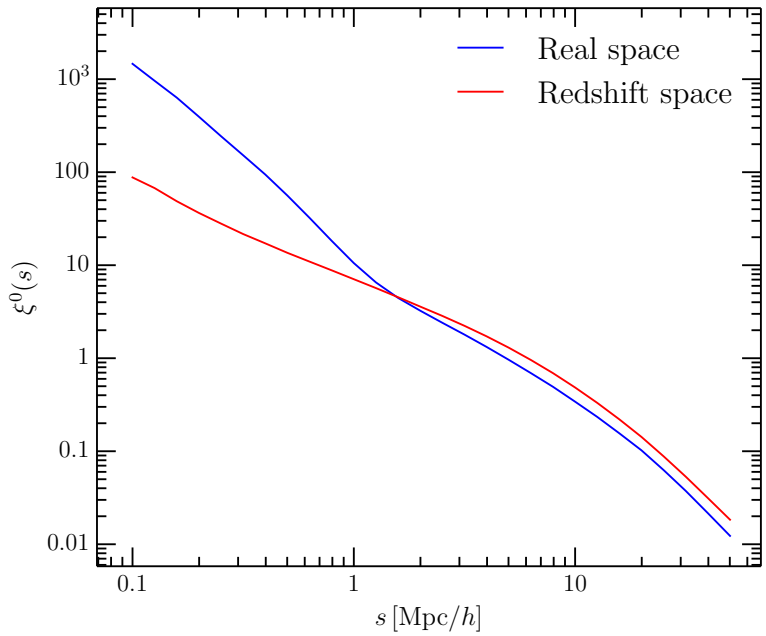

Figure 2.10: Comparison between the monopole of the two-point correlation function in real- and redshift-space. Measurements have been extracted from the mean over 26 mock catalogues of the VIPERS survey. Fingers of God suppress the clustering amplitude in the one-halo term, since structures appear more elongated than what they actually are. On the contrary, the Kaiser effect can be understood looking to the different amplitude on scales above $\sim$ 1 Mpc/h, that corresponds to the term inside round brackets inside Equation (2.100). The almost constant difference between the two curves can be justified thanks to Equation (2.100).

long-known dispersion model (Peacock & Dodds 1994). In detail, with this model it is possible to include the Fingers of God assuming

$$P^s(k,\mu) = D(k\mu\sigma_v)P^s_{\mathrm{Kaiser}}(k,\mu), \tag{2.104}$$

$$\xi^s(s,\mu) = \int_{-\infty}^{+\infty} \xi^s_{\mathrm{Kaiser}}(s',\mu)f(u-u')ds', \tag{2.105}$$

where $P^s_{\mathrm{Kaiser}}(k,\mu)$ and $\xi^s_{\mathrm{Kaiser}}(s',\mu)$ are the linear components described in Equations (2.94) and (2.99), while $D(k\mu\sigma_v)$ and $f(u)$ are the damping factor respectively in Fourier and configuration space. Each one of the two configurations depends on a parameter σ_v (σ_u in configuration space) that can be regarded as an effective pairwise velocity dispersion, and that can be fitted for during the RSD analysis. From the previous two equations, we realise that one of the advantage of working with the power spectrum is that in this

case the damping factor enters in the model only as a multiplicative factor. This is no longer true as soon as we turn to the space of configurations: here, the linear term $P^s_{\rm Kaiser}(k,\mu)$ is convolved with the damping factor, making all the procedure computationally expensive and awkward. Among the most employed analytical form, we can cite the Gaussian,

$$f(u) = \frac{1}{\sqrt{2\pi}\sigma_u} \exp\left[-\frac{u^2}{2\sigma_u^2} \right], \tag{2.106}$$

and the exponential distribution,

$$f(u) = \frac{1}{\sqrt{2}\sigma_u} \exp\left[-\frac{\sqrt{2}}{\sigma_u}|u| \right], \tag{2.107}$$

whose Fourier transform are respectively

$$D(k\mu\sigma_v) = \exp\big(-(k\mu\sigma_v)^2 \big), \tag{2.108}$$

and

$$D(k\mu\sigma_v) = \frac{1}{1+(k\mu\sigma_v)^2}. \tag{2.109}$$

Unfortunately, the pairwise velocity field is strongly scale-dependent. Several studies (Bianchi et al. 2015b; Uhlemann et al. 2015) have now proved how the shape of these functions follow neither a gaussian or an exponential profile, but can in principle be approximated with a superposition of gaussian distributions (Bianchi et al. 2015a) (see Figure 2.11). Nevertheless, as long as the data points used for the RSD fit are not fully inside the non-linear regime, the approximation with an analytic function such as 2.108 or 2.109 is fair.

A further improvement of the dispersion model can be found using the prescriptions proposed by Scoccimarro (2004). The model, that clearly goes under the name of its developer, assumes only a single ansatz, that the exponential prefactor inside Equation (2.88) can be taken outside of the ensemble average. This factor can be subsequently replace with an empirical damping term as for the dispersion model. The Kaiser term in this case can be written as it follows,

$$P^s(k,\mu) = P_{\delta\delta}(k) + 2f\mu^2 P_{\delta\theta}(k) + f^2\mu^4 P_{\theta\theta}(k), \tag{2.110}$$

where $P_{\delta\delta} = P$ is the usual density power spectrum, while $P_{\theta\theta}$ and $P_{\delta\theta}$ are respectively the velocity divergence auto power spectrum and the density-velocity divergence cross power spectrum. In the case of a biased tracer, the previous equation can simply be recast as

$$P^s(k,\mu) = b^2 P_{\delta\delta}(k) + 2fb\mu^2 P_{\delta\theta}(k) + f^2\mu^4 P_{\theta\theta}(k). \tag{2.111}$$

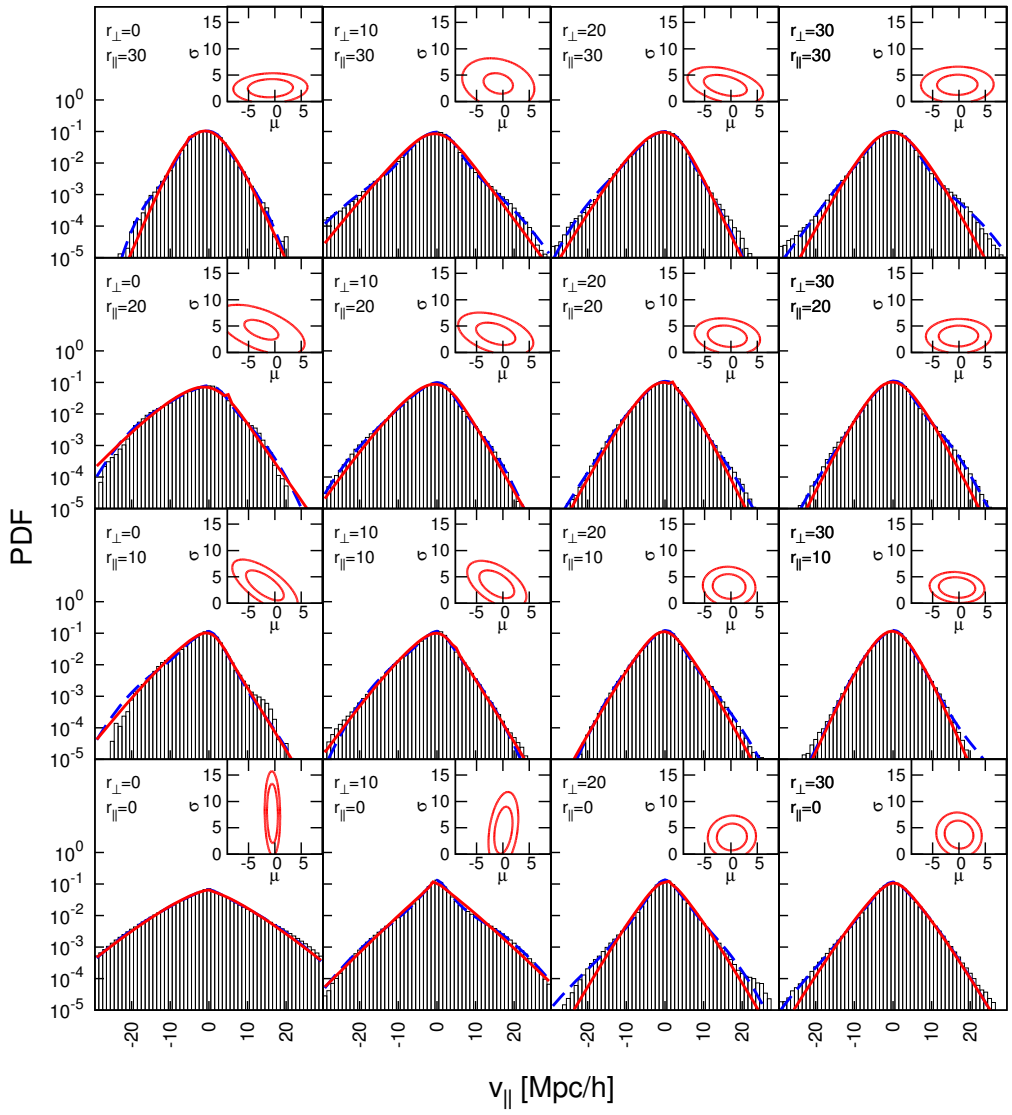

Figure 2.11: The distribution functions of los pairwise velocities $f(u)$, measured in Bianchi et al. (2015a) from a $z = 0$ snapshot of the Bolshoi N-body simulations (Riebe et al. 2013). The plot shows the distribution function measured at different separations, both orthogonal and along the line of sight. The superimposed dashed and solid lines give the model PDFs for two different prescriptions tested in Bianchi et al. (2015a). All the profiles shown in the small panels are clearly not well reproducible by a unique lorentzian/gaussian distribution, although it is possible to make this approximation outside of the strongly non-linear regime.

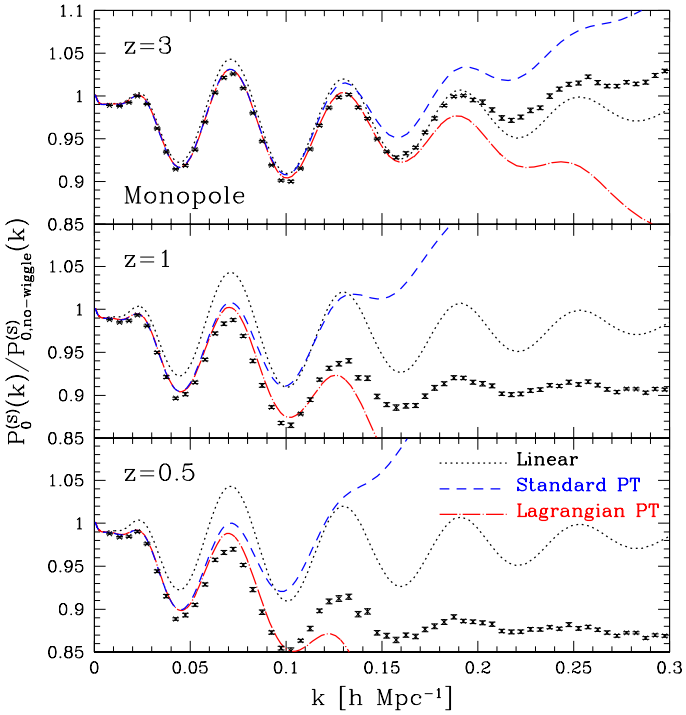

Figure 2.12: Measurements and predictions for the redshift-space power spectrum as done in Taruya et al. (2010). The plots shows the ratio of the redshift-space power spectrum to a smoothed reference spectrum that features no BAO wiggles. The three panels shows results at three different redshifts, $z = 3, 1, 0$. N-body measurements (black markers) come from the wmap5 simulations. The dotted line shows the linear theory prediction, while short dashed and dot-dashed lines respectively indicate the results of one-loop perturbation theory and Lagrangian perurbation theory calculations for the redshift-space power spectrum.

The most relevant difference with the dispersion model is that the contribution of the velocity divergence θ is not substituted with the one of the density field δ. As a matter of fact, as explained in the first section of this chapter, the assumption $\delta = \theta$ is valid only for the linear theory (and thus only for wavelenghts $k \ll 1$ and redshifts $z \gg 1$). By separately considering the different contribution of density and velocity to the redshift-space power spectrum, it is possible to obtain a slightly improved description of redshift-space distortions down to the mildly non-linear regime.

An even further improvement is the one proposed with the TNS model (Taruya et al. 2010). In this case, the Scoccimarro ansatz of taking the exponential prefactor outside of the ensemble average is avoided, and using second order perturbation theory, it can be substituted by additional correc-

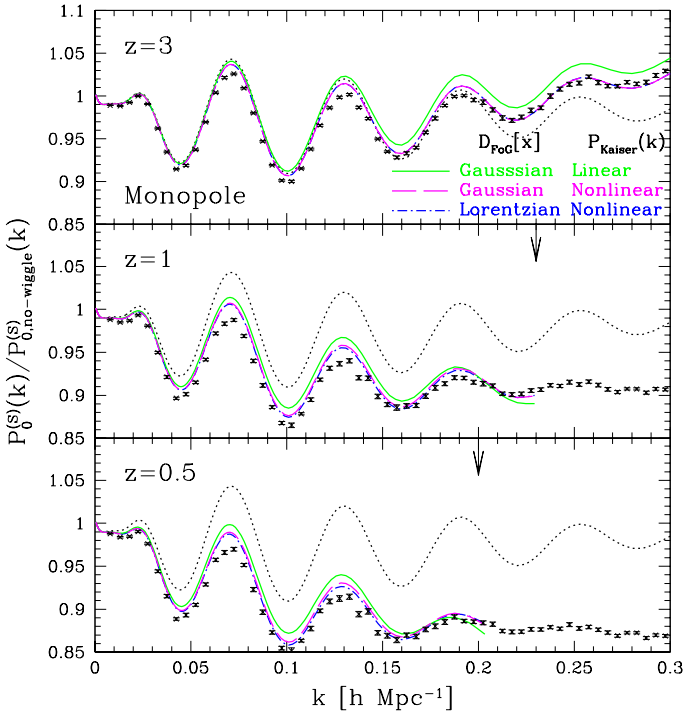

Figure 2.13: Same as in Figure 2.12, but showing predictions from empirical models (Taruya et al. 2010). In detail, the solid green, purple dashed and blue dash-dotted lines respectively represent the dispersion model with a gaussian damping factor and the Scoccimarro model with a gaussian and lorentzian damping factor. The dotted line still represents linear theory predictions.

tion terms appearing inside Equation (2.111), yielding

$$P^s(k,\mu) = b^2 P_{\delta\delta} + 2fb\mu^2 P_{\delta\theta} + f^2\mu^4 P_{\theta\theta} + C_A(b,f,k,\mu) + C_B(b,f,k,\mu). \quad (2.112)$$

The terms C_A and C_B will be accurately described in Section 3.2, where we will spend some pages to depict the procedure adopted for their computation.

In this section, we want to stress how much accurate is the TNS model with respect to other RSD models. Figures 2.12, 2.13 and 2.14 (that are taken from Taruya et al. (2010)) can be used as a trustful example of this statement. Figure 2.12 shows a comparison between measurements of the redshift-space power spectrum from the wmap5 simulation (Taruya et al. 2009) and predictions coming from linear theory and perturbation theory. In all the panels, the y-axis shows the redshift-space power spectrum divided by a smoothed power spectrum that features no BAO wiggles (Eisenstein & Hu 1998). We can recognize the improvement provided by perturbation theory

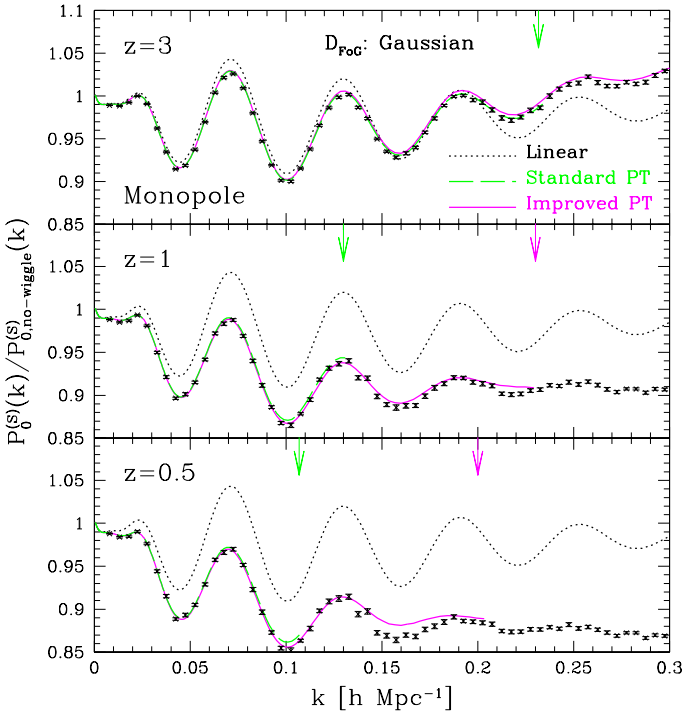

Figure 2.14: Same as in Figure 2.12, but showing predictions from the TNS model (Taruya et al. 2010). The solid purple and green dashed lines represent the output given by the TNS model once the density and velocity spectra $P_{\delta\delta}$, $P_{\delta\theta}$, $P_{\theta\theta}$ are computed respectively using an improved second order perturbation theory (improved PT in the labels) and the standard perturbation theory. The dotted line still represents linear theory predictions. The vertical arrows indicate the maximum wavenumber $k_{1\%}$ at which the accuracy of the particular perturbation theory model to reproduce the N-body results is better than 1% (that is, the systematic deviation is below 1%).

with respect to the linear prediction as soon as we move to lower redshifts (non-linearities become stronger). However, above a typical $k_{\rm max}$ (which is approximately $0.1\,h\,{\rm Mpc}^{-1}$ at $z = 0$) all the models fail in reproducing the measurements. In Figure 2.13, the authors move forward, showing the best fit using the dispersion and the Scoccimarro model, that clearly reduce the deviation of models from data points at larger wavelenghts thanks to the presence of a damping factor, either gaussian or lorentzian (σ_v is fitted as a free parameter). Nevertheless there is still place for improvements, given that the accuracy of the matching between data and best fits is not very large. Figure 2.14 shows the best fits using the TNS model. In all the three panels, the damping factor is gaussian. In this case, the authors test the difference obtained in the fit when using density and velocity spectra $P_{\delta\delta}$, $P_{\delta\theta}$ and $P_{\theta\theta}$ computed with perturbation theories of different orders. In both

cases, the accuracy of the fit is significant and it is definitely larger than in the previous plot. This, along with the accurate tests performed on the VIPERS simulated lightcones (see Section 6.2), is the main reason at the basis of our choice of employing the TNS model to provide a final RSD measurements of the growth rate using the VIPERS galaxy sample.

2.4.1 Measuring the real-space correlation function from a galaxy survey

As described in this section, peculiar velocities introduce distortions in the measured two-point statistics, either the power spectrum and the correlation function. Nevertheless, it is still possible to deduce the real-space function simply using part of the available information. Indeed, given that real-space clustering is homogeneous and isotropic on large enough scales (cosmological principle), we shall expect the clustering along the direction orthogonal to the line of sight to be a good representative of the 3D clustering. This can be justified since the former is not affected by redshift distortions, that instead are concentrated only along the line of sight.

Following Lilje & Efstathiou (1988) and Saunders et al. (1992), the real-space correlation function (that consists only of its monopole) can be recovered defining the projected correlation function as

$$w_p(r_p) = 2 \int_0^\infty \xi(r_p, \pi) d\pi, \tag{2.113}$$

which is just the anisotropic function $\xi(r_p, \pi)$ integrated along the line of sight in order to get rid of the redshift distortions. Indeed, there is no difference between the projected correlation function measured in real- or redshift-space. Applying the substitution $y = \sqrt{r_p^2 + \pi^2}$, we can write

$$w_p(r_p) = 2 \int_{r_p}^\infty \frac{y\xi(y)}{\sqrt{y^2 - r_p^2}} dy, \tag{2.114}$$

where we have made explicit the equivalence $\xi(r_p, \pi) = \xi(y)$. By inverting the precedent relation, it is possible to find

$$\xi(r) = \frac{1}{\pi} \int_r^\infty \frac{dw_p(r_p)/dr_p}{\sqrt{r_p^2 - r^2}} dr_p. \tag{2.115}$$

Note that, in this last equation, π is the mathematical constant rather than the coordinate for the separation along the line of sight. In computational terms, Equation (2.115) can be hard to implement, since it features both

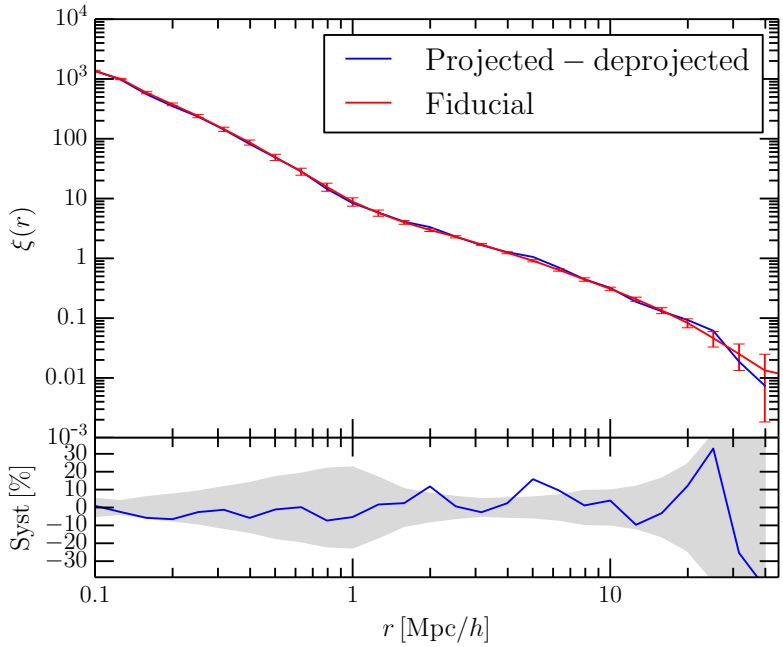

Figure 2.15: Top panel: comparison between the measured real-space correlation function (red line) and the one obtained with the projection-deprojection method (blue line), using a single mock catalogue of the VIPERS survey. Bottom panel: systematic deviation between the two curves. The grey shaded region marks the 1-sigma confidence of the measured real-space function (similarly to red errorbars in the top panel).

a derivative and singularities at $r_p = r$. Though, it is possible to linearly interpolate $w_p(r_p)$ between its sampling positions $r_{p\,i}$ leading to

$$\xi(r_{p,\,i}) = -\frac{1}{\pi} \sum_{j \geq i} \frac{w_p(r_{p,\,j+1}) - w_p(r_{p,\,j})}{r_{r,\,j+1} - r_{p,\,j}} \log \left(\frac{r_{p,\,j+1} + \sqrt{r_{p,\,j+1}^2 - r_{p,\,i}^2}}{r_{p,\,j} + \sqrt{r_{p,\,j}^2 - r_{p,\,i}^2}} \right). \tag{2.116}$$

The only source of uncertainties that we have not mentioned so far comes from the estimation of the projected correlation function $w_p(r_p)$, since, although the integral inside Equation (2.114) goes up to infinity, during the computation we must select a finite $\pi_{\max}$. This choice could alter the results in two different ways: indeed, selecting a small value of $\pi_{\max}$ could imply a loss of signal in the recovered real-space function, but at the same time, a large $\pi_{\max}$ could introduce in the procedure a significant amount of noise, simply because we are including scales whose statistical uncertainty is already large. It is thus necessary to balance the two effects and select a $\pi_{\max}$ somewhere in the middle.

Figure 2.15 shows an example of how well this procedure can work. We use one single mock realisation, and measure both the real-space correlation function $\xi(r)$ and the anisotropic redshift-space function $\xi(r_p, \pi)$. From the latter, we deduce $\xi(r)$ following the procedure described above and compare the two functions. In this case, we have selected $\pi_{\rm max} = 50\,h^{-1}\,{\rm Mpc}$. The agreement is good (almost every data point of the deduced function is within 1-sigma from the direct measurement). Therefore we find that this procedure is capable of producing a reliable and trustful estimate of the real-space two-point function also in a galaxy sample whose comoving coordinates are expressed only in redshift-space.

Chapter 3

IMPLEMENTING MODELS OF RSD

The theoretical description of the clustering distortions induced by peculiar velocities have been already addressed in Chapter 2. Here we illustrate the ingredients required in the construction of a proper model for redshift-space distortions (from the linear theory enclosed in the Kaiser model to the most sophisticated prescriptions), and the methodology for deriving them with precision and accuracy.

With the only assumptions of working in the plane-parallel approximation (meaning that the probed separation range is largely below the distance between sources and observer), the impact of redshift-space distortions on the galaxy power spectrum can be summarised within Equation (2.88). With the exception of RSD parameters, that will be fitted directly over the measurements of VIPERS, the elements necessary for the implementation of this equation, and of the models we want to test, are the density auto power spectrum $P_{\delta\delta}(k)$, the velocity divergence auto power spectrum $P_{\theta\theta}(k)$, the cross power spectrum $P_{\delta\theta}(k)$, the non-linear mode coupling terms $C_A(k, \mu, f, b)$ and $C_B(k, \mu, f, b)$ of the Taruya-Nishimichi-Saito model, and finally the shape of the damping factor $D(k\mu\sigma_v)$ in the strong non-linear regime.

3.1 The real-space density and velocity spectra

The real-space counterpart of the quantities we want to predict in redshift-space can be obtained in different ways. On sufficiently large scales ($k < 0.2\,h\,\mathrm{Mpc}^{-1}$) it has been shown (Crocce & Scoccimarro 2006; Gil-Marín et al. 2012) that using renormalised Eulerian perturbation theory we can give a description of the real-space density power spectrum with an accuracy $< 2\%$

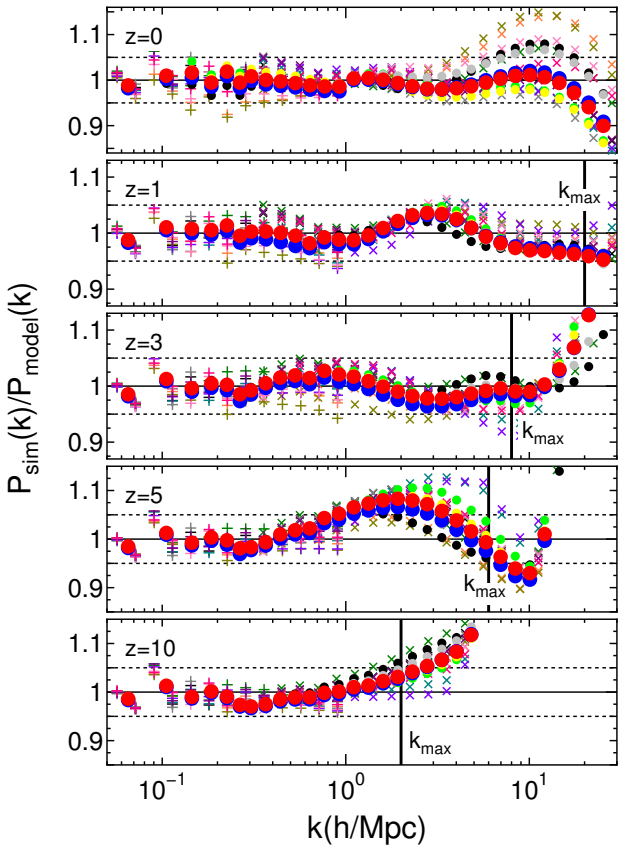

Figure 3.1: Accuracy of the fit performed by (Takahashi et al. 2012) for the matter density power spectrum. The y-axes shows the ratio between the measured (from simulations) power spectrum and the best fit using HALOFIT prescriptions. Different markers stand for different cosmologies; filled circles show results for 6 WMAP models, whereas cross and plus markers show results for different Coyote models (Heitmann et al. 2009). The considered redshift increases from the top to the bottom panel (as labelled in the figure). The horizontal dotted lines show a systematic deviation of 5% from the unity.

at $z < 1.5$. Not only, these results can be afforded with similar perturbative approaches, like standard perturbation theory (Bernardeau et al. 2002; Scoccimarro & Frieman 1996), Lagrangian perturbation theory (Matsubara 2008; Carlson et al. 2009) and closure theory (Taruya & Hiramatsu 2008; Carlson et al. 2009). Nevertheless, the VIPERS intrinsic limitation of precisely probing only comoving scales $s < 50\,h^{-1}\,\mathrm{Mpc}$ forces us to rely on an empirical description of the power spectrum, based on fitting functions that can be tuned to large N-body simulations. We assume one of the most successful of these fitting functions, HALOFIT (Smith et al. 2003; Takahashi et al. 2012), to obtain a precise estimate of the real-space density auto power spectrum

$P_{\delta\delta}(k)$ up to $k_{max} = 1\,h\,\mathrm{Mpc}^{-1}$ (with an accuracy $< 5\%$ at $0 < z < 10$). We show in Figure 3.1 the accuracy of the fit as it has been obtained directly in Takahashi et al. (2012) using different cosmologies, mostly WMAP-like and from the Coyote Universe project Heitmann et al. (2009). We make use of the public package CAMB (Code for Anisotropies in the Microwave Background, Lewis et al. (2000)), that can produce a power spectrum prediction (both linear and using HALOFIT), giving the chance to the user to select the value of cosmological parameters, sampling positions and other variables.

In regard of the velocity auto and cross spectra, the strategy we have adopted is slightly different, since there are not yet public and well-known empirical formulae as for the density auto spectrum (but with some rare exception, like in Jennings et al. (2011), Jennings (2012) and (Hahn et al. 2015)). Given the strong requirement of reaching a good accuracy at non-linear scales, mostly because of the peculiar geometry of VIPERS, the previous fitting formulae cannot be used directly while analysing the VIPERS dataset. We have developed some reliable fitting functions, with the aim of reaching an accuracy at $k \sim 1\,h\,\mathrm{Mpc}^{-1}$ similar to the one afforded by HALOFIT also for the velocity spectra.

3.1.1 Fitting functions for $P_{\delta\theta}$ and $P_{\theta\theta}$

As for the previous case of the matter non-linear power spectrum, we also need a reliable description of the velocity power spectra down to the mildly non-linear regime. This is motivated one again by the limiting maximum scale probed by VIPERS.

In order to perform reliable and safe tests on the velocity spectra, we first need a catalogue of dark matter particles for which measurements of $P_{\delta\theta}$ and $P_{\theta\theta}$ are available. In this work, we make use of the DEMNUni (Carbone et al. 2016; Castorina et al. 2015) simulations.

The *Dark Energy and Massive Neutrino Universe* are a set of four N-body dark matter simulations that have been realised with the aim of testing multiple cosmological probes in the presence of massive neutrinos. They are meant to be a vanguard for future N-body simulations and a reliable tool for exploring the impact of neutrinos on a wide range of dynamical scales. The final samples have been realised using flat $\nu\Lambda$CDM cosmologies, featuring different values of the total neutrino mass, $\sum m_\nu = 0, 0.17, 0.3, 0.53\,\mathrm{eV}$, while keeping the total matter density parameter fixed at $\Omega_m = 0.32$. This implies that the density parameter of cold dark matter Ω_{cdm} changes among the four simulations according to the corresponding neutrino density Ω_ν. The latter can be easily related to the total neutrino mass, using the simple relation $\Omega_\nu = \sum m_\nu / 93.14\,h^{-2}\,\mathrm{eV}^{-1}$. Further properties shared by the four

$\sum m_\nu$ [eV]	Ω_{cdm}	Ω_ν	$\sigma_{8,mm}$	$\sigma_{8,cc}$	$\frac{m_p^c}{10^{10}}\left[\frac{M_\odot}{h}\right]$	$\frac{m_p^\nu}{10^9}\left[\frac{M_\odot}{h}\right]$
0.00	0.2700	–	0.846	0.846	8.27	–
0.17	0.2659	0.0041	0.803	0.813	8.16	1.05
0.30	0.2628	0.0072	0.770	0.786	8.08	1.85
0.53	0.2573	0.0127	0.717	0.740	7.94	2.28

Table 3.1: Parameters of the four $\nu\Lambda$CDM simulations that are not fixed among the different runs. The units of the parameter list is specified in the first row of the table.

cosmologies are the density parameter of dark energy $\Omega_\Lambda = 0.68$ and baryons $\Omega_b = 0.05$, the Hubble constant $h = 0.67$, the spectral tilt $n_s = 0.96$ and the scalar amplitude of the primordial matter power spectrum $A_s = 2.1265 \times 10^9$.

The DEMNUni have been run on the FERMI supercomputer at CINECA (5×10^6 CPU hours) using the tree particle hydrodynamical code GADGET-3. The latter has regulated the assembly of $N_{cdm} = 2048^3$ dark matter particle and $N_\nu = 2048^3$ neutrino particle (when present) within a cubic box of comoving size $L = 2000\,h^{-1}\,\mathrm{Mpc}$. The mass resolution of dark matter and neutrinos is different over the four simulations (values are listed in Table 3.1), and in all cases it is large enough to include the very large perturbation modes ($k \sim 0.5h\,\mathrm{Mpc}^{-1}$). The runs start at an initial redshift $z_{in} = 99$ and evolve to $z = 0$, with a softening length $\varepsilon = 20\,h^{-1}\,\mathrm{kpc}$. During the runs, 62 snapshots have been saved for each simulation, choosing a logarithmic binning of the scale factor $a = 1/(1+z)$.

We select four different snapshots, at $z = 0$, 0.5, 1, 1.5 to validate our fitting functions on a broad redshift range, that encloses the one of VIPERS. The usefulness of having four different neutrino masses is that in this way we can test the universality of the fit using cosmologies that possess a time evolution very different from each other. Indeed, a thermal neutrino relic component in the Universe affects both the expansion history and the growth of cosmic structures. Figure 3.2 shows the impact of adding massive neutrinos on the estimate of the linear growth rate at $z = 0$. The most salient feature is the k-dependent suppression of the growth of structures, caused by the free streaming of neutrinos below a typical scale called free streaming length. As a matter of fact, massive neutrinos can become non-relativistic

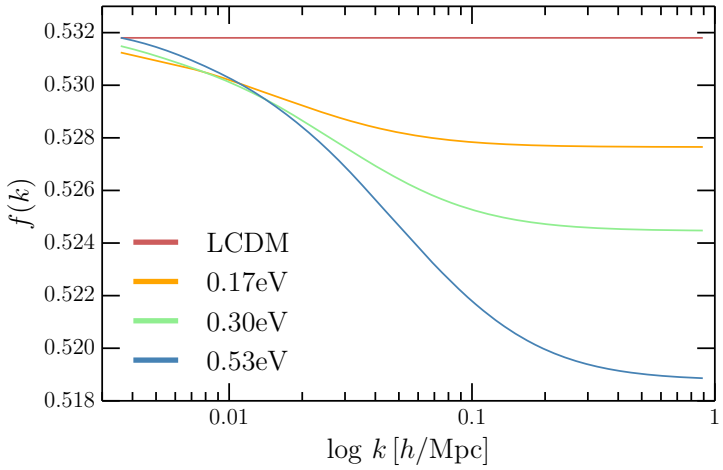

Figure 3.2: Predicted growth rate $f(k)$ at $z = 0$, for the four different cosmologies provided by the DEMNUni simulations. The main impact of introducing massive neutrinos is the suppression of power below the scale of free-streaming. This implies a k-dependent growth rate which is much more important for the highest neutrino mass.

after the epoch of recombination probed by the CMB, when the Hubble radius corresponds to a wave number k_{nr}. This transition significantly changes the interaction between massive neutrinos and cold dark matter, as, on scales $k > k_{nr}$, the large velocity dispersion of non-relativistic species suppresses the formation of neutrino perturbations. This has also an effect on the matter power spectrum, as non-relativistic neutrinos cannot contribute to the gravitational potential wells produced by cold dark matter and baryons. In a pure ΛCDM model, these wells can grow under the effect of their self-gravitation, with the only limitation being classical cooling processes.

Considering different snapshots, and thus different evolutionary stages, is a further significant way to test our fitting functions on different power spectra. Figure 3.3 shows the typical impact of non-linearities on the amplitude of the power spectrum. For clearness, we consider here only the measurements coming from the ΛCDM simulation, given that in the presence of massive neutrinos we expect the observed trends to be similar as in the reference model. Just by looking at the density-density auto spectrum $P_{\delta\delta}$, we can notice an increase of the amplitude of the spectrum with respect to linear predictions as long as time passes by. The non-linear evolution is expected in particular for large values of the wave number k, where the linear assumption that both the density contrast and the velocity module are small (δ, $\|\boldsymbol{u}\| \ll 0$) breaks down. For the same reason, the amplitude of

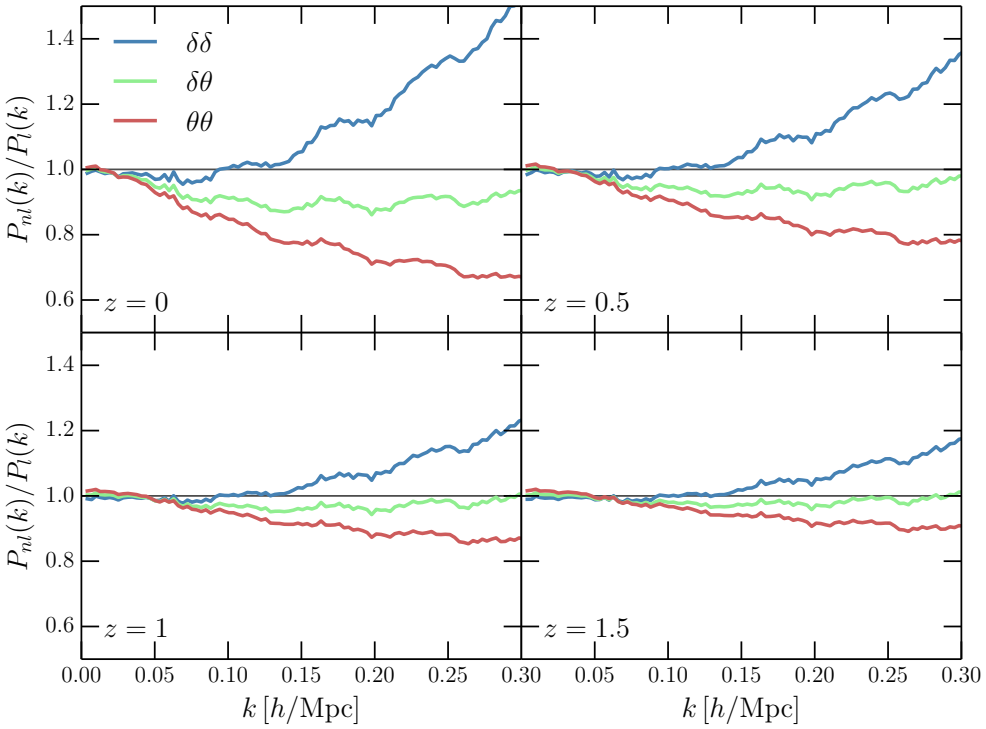

Figure 3.3: Non linear evolution of the density and velocity divergence auto and cross spectra. The four panels refer to different snapshot (as labelled within the panels themselves). Velocity spectra are measured performing a Delaunay tessellation of the velocity field and assigning a single velocity to each tetrahedron of the triangulation. Subsequently, spectra are calculated similarly to what is done for $P_{\delta\delta}$ (a better description of this procedure can be found in Bel et al. in preparation).

the non-linear velocity divergence auto spectrum $P_{\theta\theta}$ drops down because, as non-linear structures start to arise, with their internal dynamics being dominated by random velocities, coherent motions (and thus the velocity divergence) outside the strongly non-linear regime become sub-dominant.

Given these premises, we have decided to employ fitting functions featuring one single free parameter that should account for the damping of the linear prediction in the non-linear regime. First, we have tested an exponential damping like the one in the following equations,

$$P_{\delta\theta}(k) = \left(P_{\delta\delta}(k)P^{lin}(k)e^{-\frac{k}{k^*}}\right)^{\frac{1}{2}}, \tag{3.1}$$

$$P_{\theta\theta}(k) = P^{lin}(k)e^{-\frac{k}{k^*}}, \tag{3.2}$$

where in both the equations the only free parameter of the fit is the typical scale k^* that corresponds to the exponential damping scale. The shape of these functions can be motivated as it follows. As shown in Figure 3.3, the velocity auto spectrum is damped on non-linear scales, with the intensity of the damping becoming more and more severe as non-linearities take place; thus an empirical damping of the linear spectrum can be considered as a fair first attempt to model the velocity spectrum. On the contrary, the choice of a geometrical mean for the cross-spectrum is perfectly valid if we assume densities and velocities to be maximally correlated (and thus on linear scales). Clearly this is a rather strong assumption, given that the goal is to model the mildly non-linear scales of the cross spectrum, but we have found out that this template is accurate enough down to the minimum scale we want to probe. The choice of using a fixed power $\alpha = 1$ for the spectral index of the exponent, rather than having more degrees of freedom (that is, $\exp(-(k/k^*)^\alpha)$), comes from a further test we have carried out, that shows the best fit parameter α converges to 1 as soon as it is let free. The fit of the velocity power spectra is carried out using a least-squares approach. The latter consists in the research within the parameter space of the position that minimises the sum of the residuals between data and model, namely

$$\chi^2 = \sum_{i=1}^{N_{data}} \frac{(P_{model,i} - P_{data,i})^2}{\sigma_i^2}, \tag{3.3}$$

with N_{data} being the total number of sampling positions considered in the fit and σ_i^2 is the variance of the measured spectrum at the $i-$th position. The limitation of having only one realisation for each different cosmology implies that errors have to be estimated using a method alternative to computing the dispersion over a large set of mocks. In this case, we assume the variances to be well-described by a gaussian distribution, defined as

$$\sigma_i^2 = \frac{2\pi}{(Lk_i)^2}\left(P_{data,i} + \left(\frac{L}{N}\right)^3 \frac{1}{(2\pi)^3}\right)^2, \tag{3.4}$$

where $L = 2000\,h^{-1}\,\mathrm{Mpc}$ is the comoving size of the periodic box and $N = 2048^3$ is the total number of particles (CDM only in this case). We fix $k_{max} = 0.6\,h\,\mathrm{Mpc}^{-1}$ rather than the maximum available wave number because our fitting functions are not really able to capture the shape of the velocity spectra above this value.

The results of the fit are shown in the first two columns of Figure 3.4. Although both equations are able to capture the shape of the non-linear velocity spectra below 5% from the measurements, we notice a feature in the

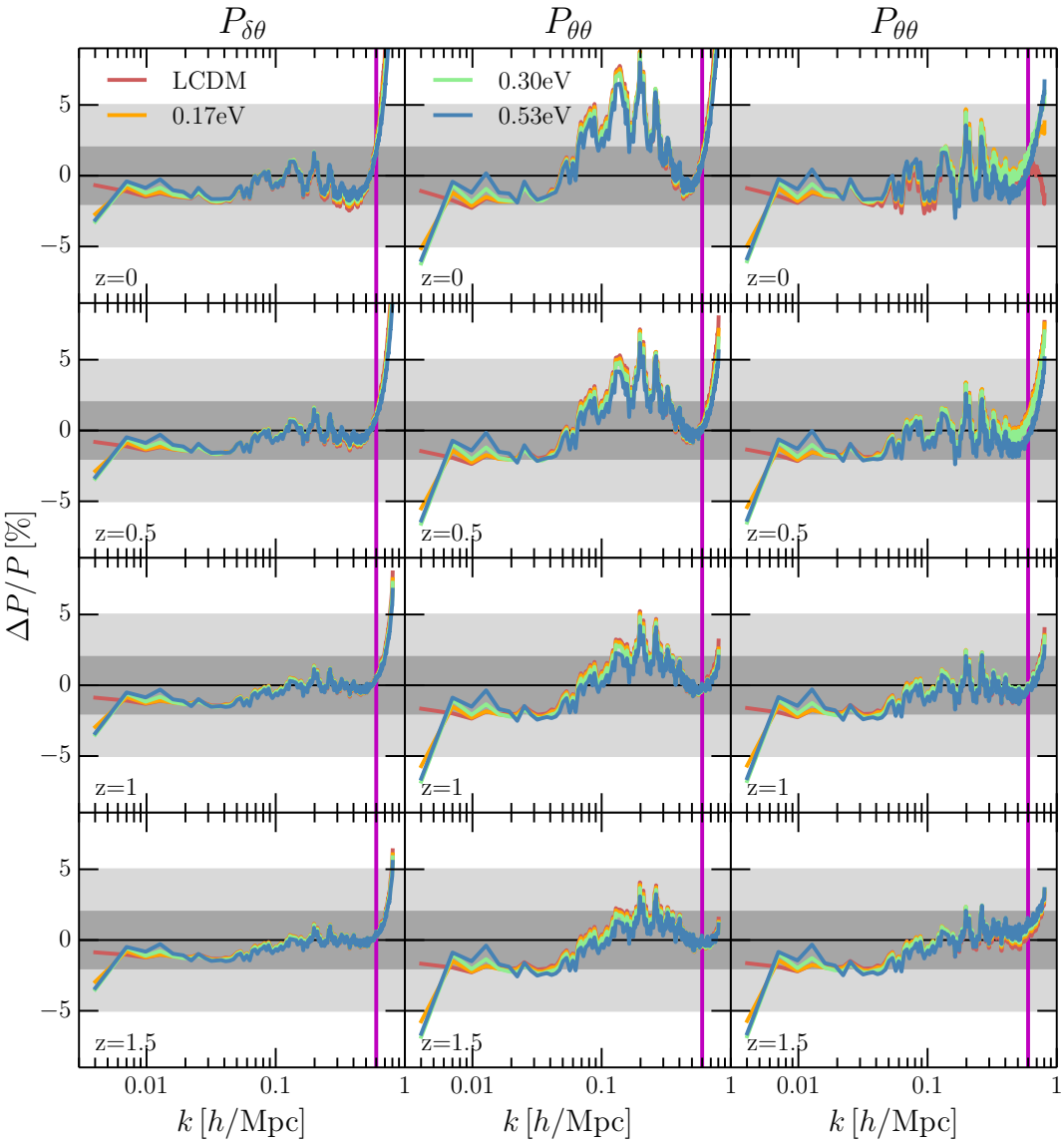

Figure 3.4: Systematic deviation of our best fitting models from measurements of the cross spectrum (left column), and the velocity auto spectrum, both with the one- and three-parameter formula (middle and right column). Different redshift snapshots are shown on different rows. Solid lines show results for different cosmologies (as labelled in the legend). The light and dark grey shaded bands represent the 5% and 2% accuracy. The vertical magenta line stands for $k_{max} = 0.6\,h\,\mathrm{Mpc}^{-1}$, which corresponds to the maximum wave number used in the fit.

fit of the velocity divergence auto power spectrum from $k = 0.1\,h\,\mathrm{Mpc}^{-1}$ up to $k = 0.3\,h\,\mathrm{Mpc}^{-1}$ that we would like to remove. For this reason we test

a slightly more sophisticated fitting formula for $P_{\theta\theta}$ that features three free parameters, like

$$P_{\theta\theta}(k) = P^{lin}(k)\left(p_1 k + p_2 + (1-p_2)e^{-\frac{1}{2}\left(\frac{k}{k^*}\right)^2}\right). \tag{3.5}$$

In this new equation, the set of free parameters is constituted by p_1, p_2 and k^*. Results are shown in the third column of Figure 3.4. In this case, our fitting formulae can fit measurements of $P_{\theta\theta}$ with a systematic deviation $\lesssim 2\%$ at all the redshifts and also for the full set of neutrino masses considered in this analysis. The goodness of the fit of the velocity spectra is astonishing, considered that besides we are just using one single free parameter for $P_{\delta\theta}$ (and $P_{\theta\theta}$, if we accept a tollerance on the systematics below 5%).

Nevertheless, our first goal is to find an universal relation capable of providing a precise value of k^* (and also p_1 and p_2) as a function of the amount of non-linearities at the considered redshift and for the considered cosmological model. The main motivation for choosing this approach is that the velocity spectra are damped differently according to the particular cosmology they refer to. A schematic illustration of this statement can be find in Figure 3.5, where the velocity spectra (auto and cross) are plotted as a function of the corresponding density auto spectrum. As one can easily expect, these trends are different when considering different redshifts, since non-linear evolution of density and velocity spectra has acted differently on different snapshots (see Figure 3.3). This knowledge has been already made explicit thanks to the analysis performed in Jennings (2012), in which they have produced cosmology-independent fitting functions of the velocity spectra at $z = 0$, and generated scaling relations to be used at a generic redshift z'. The most important deviation between our prediction and their results is that, even considering four different cosmologies (a ΛCDM and three quintessence models, SUGRA, CNR and 2EXP, all normalised so that $\sigma_8 = 0.82$ at $z = 0$), the behaviour of $P_{\delta\theta}$ and $P_{\theta\theta}$ as a function of $P_{\delta\delta}$ in their analysis is constant at each fixed redshift (see Figure 3.6). We claim that this apparently universal trend is mainly due to the particular choice of cosmologies they have selected. In a precedent paper (Jennings et al. 2010) that mainly dealt with the description of the simulations used for the analysis on the velocity spectra, they have shown a similar behaviour of the linear growth factor $D(z)$ for the four cosmologies they have tested. If the non-linear velocity-density relation was regulated by the amplitude of $D(z)$, then the observed results would be biased towards the expectation of an universal shape for this profile. An even more clear hint of the goodness of such statement emerges from the apparent trend of the SUGRA model, which is the one whose growth factor (and by consequence σ_8 as well) starts sooner to deviate from the ΛCDM case,

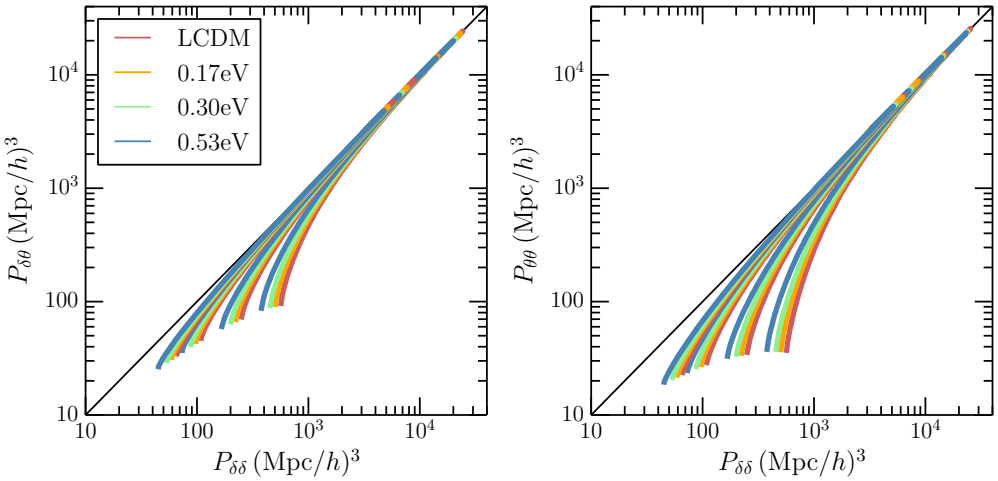

Figure 3.5: Relation between the velocity cross(left)/auto(right) velocity spectrum and the density auto spectrum for the different redshifts and cosmologies considered in this work. Different colours represent different values of the total neutrino mass. Different redshifts(z = 0, 0.5, 1, 1.5) are respectively organised in quartets from z = 0(strongest damping) to z = 1.5(weakest damping). The three spectra are normalised so that at large scale (small wave numbers) their amplitude is the same. The black solid line represent linear prediction ($P_{\delta\delta} = P_{\delta\theta} = P_{\delta\theta}$).

moving from $z = 0$ to higher redshifts. Our simulations are normalised in a slightly different way than the ones used in Jennings (2012), since in our case, the four cosmologies feature the same scalar amplitude at the CMB. This is a first hint for understanding the different trend we observe, an approach to universality at $z = 0$ in their case, and one at $z >> 1$ in our analysis.

Therefore, we have tried to relate the fitted values of the free parameters to the linear σ_8 of the corresponding matter spectrum. In this case, we have found some additional fitting formulas to predict the free parameters of Equations (3.1), (3.2) and (3.5) once the input cosmology (and thus σ_8) is known. We have tested the following relations,

$$\frac{1}{k^*} = a(\sigma_8)^b \tag{3.6}$$

for the one-parameter case, and

$$k^*, p_1, p_2 = a + b\sigma_8 \tag{3.7}$$

for the three-parameter case. In both of them, we have used two free parameters, a and b, whose best fitting value are summarised in Table 3.2. Results of the fit are shown in Figure 3.7. In both cases, we can see a very

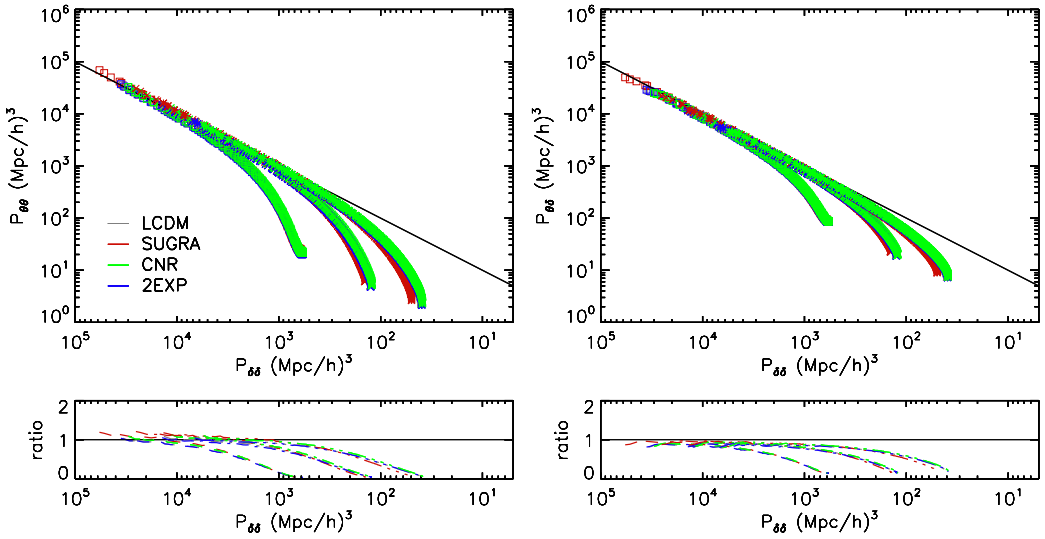

Figure 3.6: Reference plot of Jennings et al. (2011), showing the relation between velocity and density in the same way as in Figure 3.5. Different colours stand for different quintessence models, with multiple line of the same colours showing results at different redshifts ($z = 0$, 1, 2 in this case). Bottom panels show the ratio between the spectra.

strong relation between the values of the fitted parameters and σ_8. Not only, but our fit is performed with an accuracy $< 5\%$ for most of the considered points. We have also tested how the predicted velocity spectra change for small variations of the free parameters, confirming a good stability of our results.

In conclusion, we have developed fitting functions for the velocity auto and cross spectra that can be applied also in the case where the considered cosmologies are very different. The only requirement is the knowledge of the linear σ_8, that can be easily obtained as the output of CAMB or by manually integrating the linear spectrum using Equation 2.74.

3.2 Calculation of the TNS terms

As mentioned in Chapter 2, the additional terms to the redshift-space power spectrum, $C_A(k, \mu, f, b)$ and $C_B(k, \mu, f, b)$, are generated from the non-linear mode coupling between the density and the velocity field during the transition from the Kaiser effect (squashing of structures at large separations) to the strongly non-linear Fingers of God (stretching of bound structures

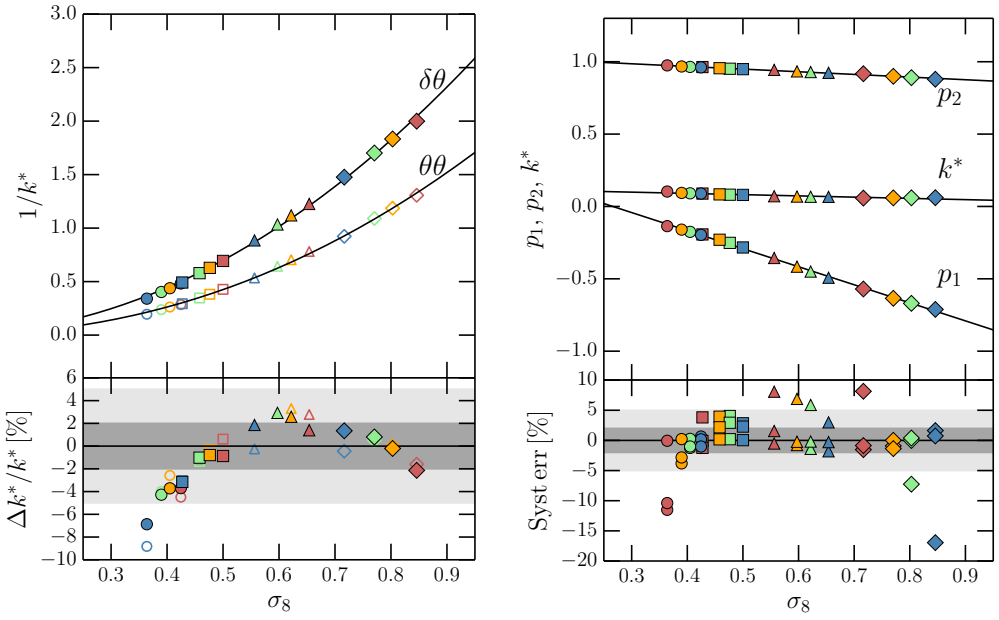

Figure 3.7: Fit of the free parameters k^*, p_1, p_2 as a function of the linear σ_8 of the corresponding density power spectrum. On the left: values of k^* for $P_{\delta\theta}$ and $P_{\theta\theta}$ (for the one-parameter formula). On the right: values of k^*, p_1, p_2 for $P_{\theta\theta}$ (for the three-parameter formula). Marker shapes and colours represent different cosmologies and redshifts, as in the previous plots. Bottom panels show the accuracy of the fit.

	$k^*_{\delta\theta}$ $[h/\mathrm{Mpc}]$	$k^*_{\theta\theta}$ $[h/\mathrm{Mpc}]$	p_1	p_2	k^* $[h/\mathrm{Mpc}]$
a	2.874	1.908	0.332	1.041	0.125
b	2.039	2.166	−1.247	−0.184	−0.086

Table 3.2: Fitting parameters of the relations between the parameters used to obtain the velocity spectra and the corresponding linear σ_8. The units of the parameter list is specified in the first row of the table.

along the line of sight). In detail, it is possible to rewrite Equation (2.88) as

$$P^s(k,\mu) = \int \frac{d\boldsymbol{r}^3}{(2\pi)^3} e^{-i\boldsymbol{k}\cdot\boldsymbol{r}} \Big\langle e^{j_1 A_1} A_2 A_3 \Big\rangle, \tag{3.8}$$

where we have substituted with j_1, A_1, A_2, A_3 the following quantities,

$$j_1 = -ik\mu f, \tag{3.9}$$
$$A_1 = u_z(\boldsymbol{r}) - u_z(\boldsymbol{r'}), \tag{3.10}$$
$$A_2 = \delta(\boldsymbol{r}) + \mu^2 f\theta(\boldsymbol{r}), \tag{3.11}$$
$$A_3 = \delta(\boldsymbol{r'}) + \mu^2 f\theta(\boldsymbol{r'}). \tag{3.12}$$

Exploiting the properties of the moment generating function, it is possible to rewrite the term within the ensemble average as

$$\Big\langle e^{j_1 A_1} A_2 A_3 \Big\rangle = \exp\{\langle e^{j_1 A_1}\rangle_c\} \times \big[\langle e^{j_1 A_1} A_2 A_3\rangle_c + \langle e^{j_1 A_1} A_2\rangle_c + \langle e^{j_1 A_1} A_3\rangle_c\big], \tag{3.13}$$

where a subscript c refers to the connected part of the total moment. The ansatz assumed in the model of Scoccimarro (that the exponential pre-factor can be completely taken outside the ensemble average) is not accounting for the presence of the term $e^{j_1 A_1}$ in front of A_2 and A_3. This coupling cannot be easily broken, and it is introducing a non-trivial correlation between the density and the velocity field. Once again, on sufficiently large scales, the velocity field is organised so that coherent motions stream towards the overdense regions, leading to $j_1 = 0$ and thus retrieving predictions from the linear theory.

Assuming $j_1 \to 0$ small enough, but not completely zero, it is possible to expand the terms inside square brackets in Equation (3.13) up to the second order, and taking only the leading and next-to-leading contribution. This yields

$$\begin{aligned}\langle e^{j_1 A_1} A_2 A_3\rangle_c + \langle e^{j_1 A_1} A_2\rangle_c + \langle e^{j_1 A_1} A_3\rangle_c \simeq \langle A_2 A_3\rangle + j_1\langle A_1 A_2 A_3\rangle_c + \\ + j_1^2\{\langle A_1 A_2\rangle_c \langle A_1 A_3\rangle_c\} + \mathcal{O}(j_1^3),\end{aligned} \tag{3.14}$$

where it is possible to underline two different terms, the one involving the mixed bispectrum $\langle A_1 A_2 A_3\rangle_c$ and the one involving the squared mixed spectrum $\langle A_1 A_2\rangle_c \langle A_1 A_3\rangle_c$. The contribution of these terms to the anisotropy felt by the redshift space power spectrum can be thus expressed as

$$A(k,\mu) = j_1 \int \frac{d\boldsymbol{r}^3}{(2\pi)^3} e^{-i\boldsymbol{k}\cdot\boldsymbol{r}} \langle A_1 A_2 A_3\rangle_c, \tag{3.15}$$

$$B(k,\mu) = j_1^2 \int \frac{d\boldsymbol{r}^3}{(2\pi)^3} e^{-i\boldsymbol{k}\cdot\boldsymbol{r}} \langle A_1 A_2\rangle_c \langle A_1 A_3\rangle_c. \tag{3.16}$$

Using perturbation theory, we can express these integrals in a different fashion. Following Taruya et al. (2010) and de la Torre & Guzzo (2012), we can adapt them for a biased tracer as the sum over different contribution, namely

$$C_A(k,\mu,f,b) = \sum_{m,n=1}^{3} b^{3-n} f^n \mu^{2m} P_{Amn}(k), \tag{3.17}$$

$$C_B(k,\mu,f,b) = \sum_{n=1}^{4} \sum_{a,b=1}^{2} b^{4-a-b} (-f)^{a+b} \mu^{2n} P_{Bnab}(k), \tag{3.18}$$

where f is the growth rate, b is the bias of the tracer and

$$\begin{aligned} P_{Amn}(k) =& \frac{k^3}{(2\pi)^2} \Bigg[\int_0^\infty dr \int_{-1}^{+1} dx \Big(A_{mn}(r,x) P(k) + \tilde{A}_{mn}(r,x) P(kr) \Big) \times \\ & \times \frac{P\Big(k\sqrt{1+r^2-2rx}\Big)}{(1+r^2-2rx)^2} + P(k) \int_0^\infty dr a_{mn}(r) P(kr) \Bigg], \end{aligned} \tag{3.19}$$

$$P_{Bnab}(k) = \frac{k^3}{(2\pi)^2} \Bigg[\int_0^\infty dr \int_{-1}^{+1} dx \Big(B^n_{ab}(r,x) \frac{P_{a\theta}\Big(k\sqrt{1+r^2-2rx}\Big) P_{b\theta}(kr)}{(1+r^2-2rx)^a}. \tag{3.20}$$

The non-vanishing components of A_{mn}, $\tilde{A}_{mn}$, a_{mn} and B^n_{ab} have been directly provided in Taruya et al. (2010), and are as it follows,

$$A_{11} = -\frac{r^3}{7}\{x + 6x^3 + r^2 x(-3+10x^2) + r(-3+x^2-12x^4)\},$$

$$A_{12} = \frac{r^4}{14}(x^2-1)(-1+7rx-6x^2),$$

$$A_{22} = \frac{r^3}{14}\{r^2 x(13-41x^2) - 4(x+6x^3) + r(5+9x^2+42x^4)\},$$

$$A_{23} = A_{12},$$

$$A_{33} = \frac{r^3}{14}(1-7rx+6x^2)\{-2x + r(-1+3x^2)\},$$

for A_{mn},

$$\tilde{A}_{11} = \frac{1}{7}(x + r - 2rx^2)(3r + 7x - 10rx^2),$$

$$\tilde{A}_{12} = \frac{r}{14}(x^2-1)(3r+7x-10rx^2),$$

$$\tilde{A}_{22} = \frac{1}{14}\{28x^2+rx(25-81x^2)+r^2(1-27x^2+54x^4)\},$$

$$\tilde{A}_{23} = \frac{r}{14}(1-x^2)(r-7x+6rx^2),$$

$$\tilde{A}_{33} = \frac{1}{14}(r-7x+6rx^2)(-2x-r+3rx^2),$$

for $\tilde{A}_{mn}$,

$$a_{11} = -\frac{1}{84r}\left[2r(19-24r^2+9r^4)-9(r^2-1)^3\log\left|\frac{r+1}{r-1}\right|\right],$$

$$a_{12} = \frac{1}{112r^3}\left[2r(r^2+1)(3-14r^2+3r^4)-3(r^2-1)^4\log\left|\frac{r+1}{r-1}\right|\right],$$

$$a_{22} = \frac{1}{336r^3}\left[2r(9-185r^2+159r^4-63r^6)+9(r^2-1)^3(7r^2+1)\log\left|\frac{r+1}{r-1}\right|\right],$$

$$a_{23} = a_{12},$$

$$a_{33} = \frac{1}{336r^3}\left[2r(9-109r^2+63r^4-27r^6)+9(r^2-1)^3(3r^2+1)\log\left|\frac{r+1}{r-1}\right|\right],$$

for a_{mn}, and

$$B^1_{11} = \frac{r^2}{2}(x^2-1),$$

$$B^1_{12} = \frac{3r^2}{8}(x^2-1)^2,$$

$$B^1_{21} = \frac{3r^4}{8}(x^2-1)^2,$$

$$B^1_{22} = \frac{5r^4}{16}(x^2-1)^3,$$

$$B^2_{11} = \frac{r}{2}(r+2x-3rx^2),$$

$$B^2_{12} = -\frac{3r}{4}(x^2-1)(-r-2x+5rx^2),$$

$$B^2_{21} = \frac{3r}{4}(x^2-1)(-2+r^2+6rx-5r^2x^2),$$

$$B^2_{22} = -\frac{3r^2}{16}(x^2-1)^2(6-30rx-5r^2+35r^2x^2),$$

$$B^3_{12} = \frac{r}{8}\{4x(3-5x^2)+r(3-30x^2+35x^4)\},$$

$$B_{21}^3 = \frac{r}{8}\{-8x + r[-12 + 36x^2 + 12rx(3 - 5x^2) + r^2(3 - 30x^2 + 35x^4)]\},$$

$$B_{22}^3 = \frac{3r}{16}(x^2 - 1)\{-8x + r[-12 + 60x^2 + 20rx(3 - 7x^2) + \\ + 5r^2(1 - 14x^2 + 21x^4)]\},$$

$$B_{22}^4 = \frac{r}{16}\{8x(-3 + 5x^2) - 6r(3 - 30x^2 + 35x^4) + 6r^2x(15 - 70x^2 + 63x^4) + \\ + r^3[5 - 21x^2(5 - 15x^2 + 11x^4)]\},$$

for B_{ab}^n.

The integrals inside Equations (3.19) and (3.20) are not straightforward to solve. In particular the integration of the a_{mn} is hard since these terms rapidly goes to r as $r \ll 1$, leading to strong oscillations that are generated by numerical issues. We have adopted a slightly better approach, that consists in the expansion of the logarithm inside a_{mn} up to the order when the term can be approximated to a constant. This value can be used for sufficiently large values of r instead of the full expression of a_{mn}.

The integration has been realised using the GNU Scientific Library (GSL), and in detail exploiting the CQUAD routine. This is a doubly-adaptive quadrature routine, capable of handling most type of singularities, among which also divergent integrals. The output of the integration has been tested by cross-checking both with a parallel internal code (written by Sylvain de la Torre) and with the public code provided by Atsushi Taruya on his webpage. Results of this last comparison are shown in Figure 3.8. For all the terms, the agreement is almost perfect on the central region (from $k = 0.005\,h\,\mathrm{Mpc}^{-1}$ up to $k = 1\,h\,\mathrm{Mpc}^{-1}$), with only a couple of very high spikes (bottom left panel) when the considered terms cross the zero. At the boundaries instead, we can notice a systematic deviation, for which the most important explanation is the different k-range of integration.

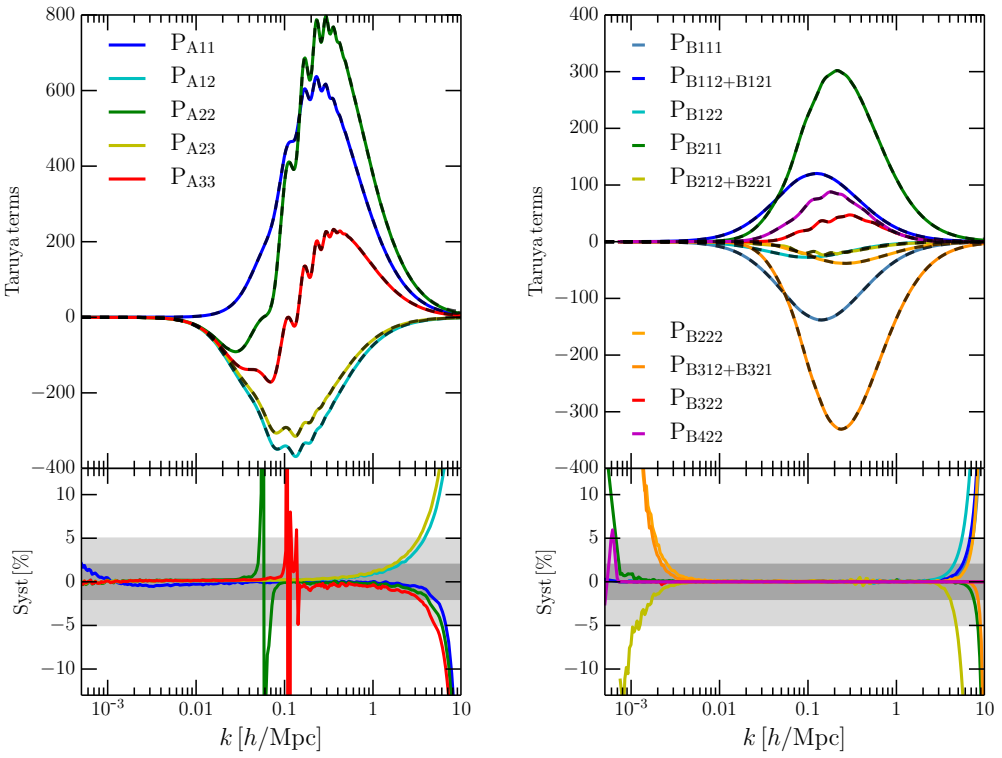

Figure 3.8: Comparison between the terms of equations 3.19 and 3.20, as computed with our code (coloured lines) and using the public routine by Taruya (dashed black lines). Bottom panels show the systematic deviation of the two independent measurements. Light/dark grey bands represent respectively the 5%/2% deviation from 0.

3.3 Choice of the damping pre-factor

As already mentioned in Section 2.4, the exponential pre-factor $D(k\mu\sigma_v)$ of the redshift-space power spectrum can partially account for the FoG effect generated by pairwise velocities inside strongly virialised regions (either haloes for dark matter particles and clusters for galaxies). In this case, σ_v can be regarded as an effective pairwise velocity dispersion, that is left as a free parameter during the fit. From a physical point of view, this approximation is definitely poor, since it has been shown (Scoccimarro 2004; Bianchi et al. 2015b) that the true velocity dispersion varies as a function of both two-point separation and orientation, and the choice of a fixed damping factor can thus results in non-negligible biases within the strongly non-linear regions. Nevertheless, studies on the small-scale velocity field have started relatively recently, with an increasing interest witnessed by several works on the topic. In the last decade many parallel analysis have been carried out,

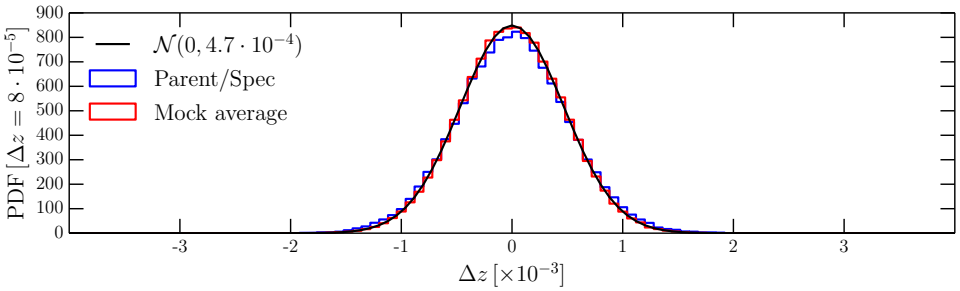

Figure 3.9: Normalised distribution of redshift errors for the first W1 mock, as measured from the spectroscopically selected sample (blue histogram) and from a parallel realisation of the parent sample that also features redshift errors (red histogram). The black line shows the reference normal distribution with mean $\mu = 0$ and dispersion $\sigma = 4.7 \cdot 10^{-4}$.

mostly regarding evolutions of the streaming model (Davis & Peebles 1983; Fisher 1995; Scoccimarro 2004) such as the gaussian streaming model (Reid et al. 2014) and the bivariate gaussian description of the pairwise velocity distribution (Bianchi et al. 2015b).

In this work, we still rely on the use of an empirical damping factor that features a single parameter σ_v. Indeed, Taruya et al. (2010) has demonstrated that the use of either a gaussian

$$D(k\mu\sigma_v) = \exp\big(-(k\mu\sigma_v)^2\big), \tag{3.21}$$

or a lorentzian

$$D(k\mu\sigma_v) = \frac{1}{1 + (k\mu\sigma_v)^2}, \tag{3.22}$$

damping factor dramatically improves the recovery of the redshift-space power spectrum over the mildly non-linear scales. Moreover, a complete description of the two-point galaxy correlation function must deal with the impact of redshift errors on the shape of the signal at small separations, that ultimately behaves as an additional damping factor. As it will be properly introduced in Chapter 4, redshift errors follow a gaussian distribution with a typical rms error of $160\,\mathrm{Km\,s^{-1}}$. In order to assess the impact of this smoothing scale, in the following section we test the recovery of the growth rate $f\sigma_8$ on different mock samples, switching off and on the presence of redshift errors, using different analytical form to model the FoG suppression. To do that, we add a gaussian displacement to redshifts coming from the parent mocks that follows the gaussian profile described above. In this way, we obtain a set of mock realisations featuring redshift errors but neglecting the impact of the target selection effects. Figure 3.9 shows the distribution of redshift displacements Δz obtained from one of the W1 mocks (blue histogram), compared to

the analytical gaussian template adopted to derive the displacements. The distribution is also compared to the signal coming from the corresponding target-selected mock (red histogram), showing a good agreement with the new set of mocks that we have constructed.

Chapter 4

THE VIPERS SURVEY

The VIMOS Public Extragalactic Redshift Survey (presentation papers: Guzzo et al. (2014); Scodeggio et al. (2016); data reduction: Garilli et al. (2014)) has been designed to collect the redshift of about 100000 extragalactic sources (divided between normal galaxies and AGNs) located at $0.4 < z < 1.2$. The intrinsic properties of such spectroscopic sample make VIPERS a perfect candidate to understand the structure of the cosmic web and the spatial distribution of galaxies at an unprecedented redshift. Indeed, the full volume of the survey ($V = 5 \times 10^7\, h^{-3}\,\mathrm{Mpc}^3$) and its mean galaxy number density ($n_g = 0.002\, h^3\,\mathrm{Mpc}^{-3}$) can be compared to the ones achieved by surveys of the local Universe, such as the 2 degree Field Galaxy Redshift Survey (2dFGRS, Colless et al. (2001)) and the Sloan Digital Sky Survey (SDSS, York et al. (2000)). For an illustrative purpose, in Figure 4.1 (Guzzo et al. 2014) we show a clear comparison between the datasets collected in the SDSS Main/LRG samples and the observations performed by VIPERS at higher redshift. Although the construction of such an innovative galaxy set has been motivated mainly by the need for a representative sample of the large-scale structure at $z \sim 1$, the wide distance range probed by the survey also makes it a powerful tool to study the morphological evolution of galaxies down to an age when the Universe was only half of its current age.

4.1 The VIPERS redshift distribution

The VIPERS spectroscopy has been selected from the Canada-France-Hawaii Telescope Legacy Survey (CFHTLS) Wide photometric catalogue (Ilbert et al. 2006; Coupon et al. 2009), making use of the T0005 release and subsequently updating it by the T0006 release. The total surface within which VIPERS has collected its dataset amounts to 24 deg^2, divided between

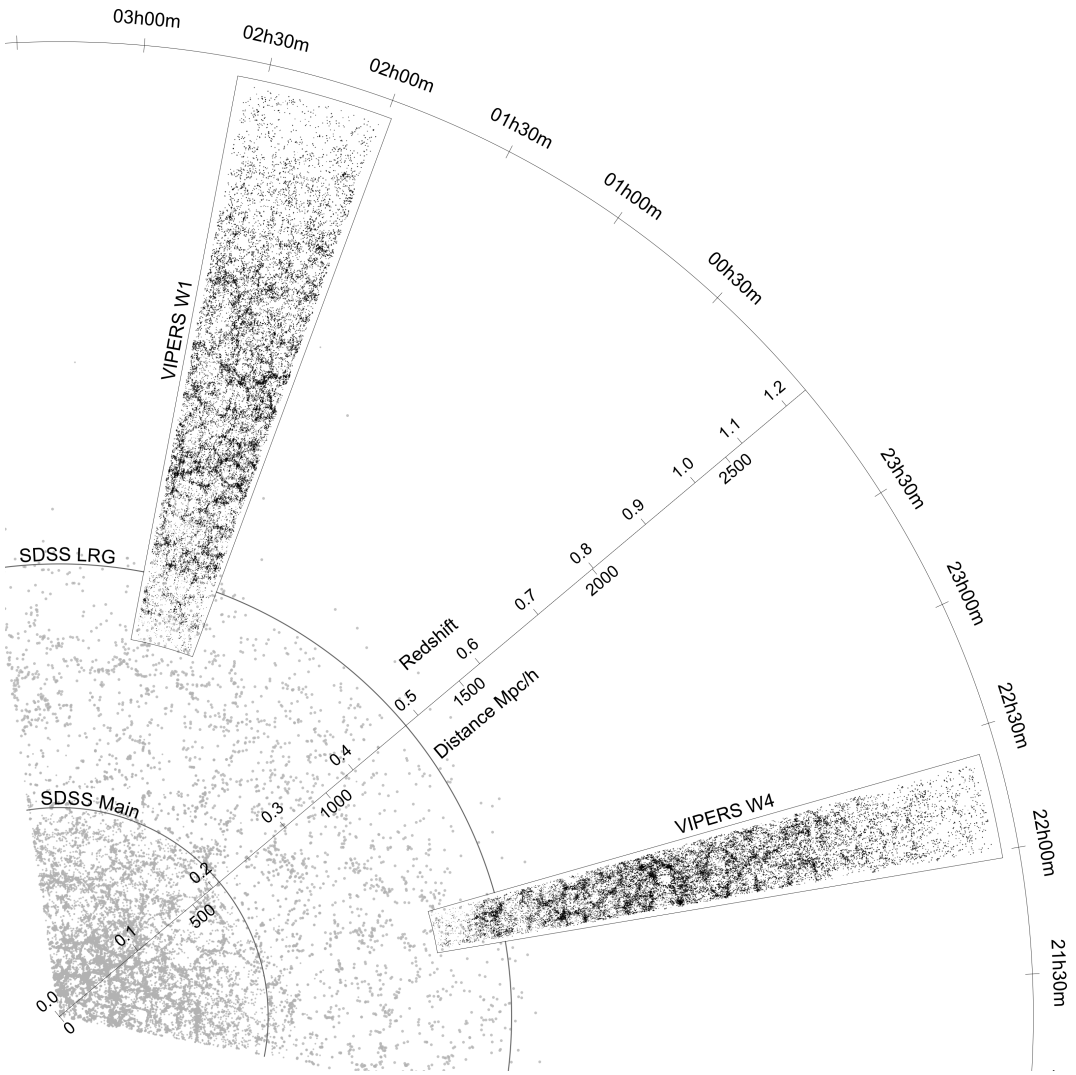

Figure 4.1: VIPERS W1 and W4 cone diagrams in the RA-z plane at $0.4 < z < 1.2$, compared to a 4-degrees thick slice of the SDSS Main ($0 < z < 0.2$) and LRG ($0.2 < z < 0.45$) samples. It is remarkable how thickly sampled the VIPERS cones are with respect to the SDSS catalogues, considering the broader redshift range and the more distant sources that have been targeted.

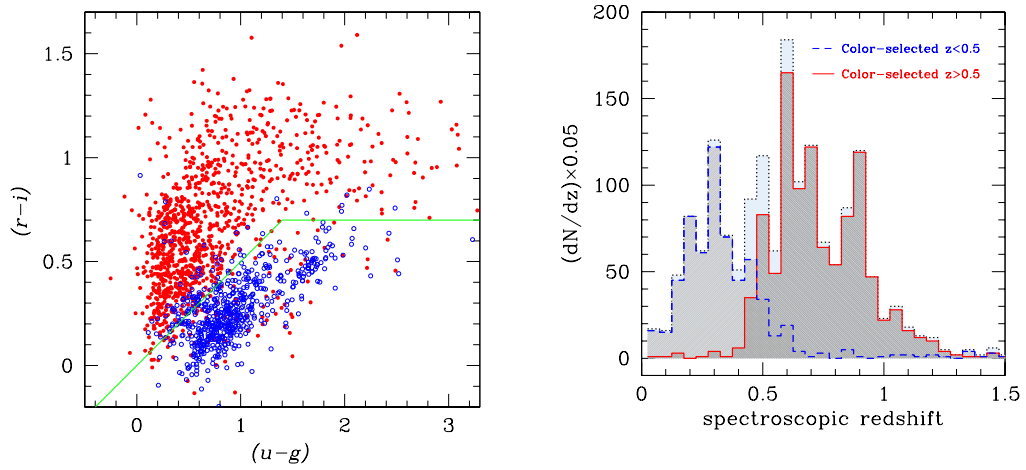

Figure 4.2: Left: scheme of the colour-colour pre-selection of the $i'_{AB} < 22.5$ VVDS-Deep photometry. Red and blue points correspond respectively to sources located at $z > 0.5$ and $z < 0.5$. The green line mark the empirical separation used to split the sample in different redshift ranges. Right: consistency check on the redshift distribution of the sample collected by the VVDS-Deep survey. The blue dash-dotted line shows the redshift distribution of the subsample corresponding to the blue points in the previous plot, while the solid red line does the same for the red points. The dotted line shows the histogram of the total redshift distribution.

two of the original CFHTLS fields, W1 (16 deg^2) and W4 (8 deg^2). Potential candidates have been selected by fixing an infrared magnitude limit of $i'_{AB} < 22.5$. Even so, the radial distribution of VIPERS is different from the one expected in a pure magnitude-limited sample. This happens because the full set of targets satisfying the VIPERS selection criteria has been pre-selected in order to remove most of the objects placed at $z < 0.5$. The isolation of the desired redshift range has been achieved using a robust colour-colour pre-selection in the $(r-i)$vs$(u-g)$ plane, capable of producing a galaxy sample featuring a completeness $> 98\%$ within the VIPERS redshift range. In Figure 4.2 we show how well this procedure can confine the desired distant sources at the expense of the closest objects, using similar results from the VVDS-Deep survey, i.e. VVDS (Le Fèvre et al. 2004; **?**; Garilli et al. 2008) and zCOSMOS (Lilly et al. 2009), as a consistency test (the first motivation of using this dataset comes from the fact that both VVDS and VIPERS are based on the same instrument). The final result of this procedure is a collection of galaxy redshifts whose distribution follows a bell profile, that approximates a magnitude-limited sample above $z > 0.6$. In a previous redshift-space distortions analysis performed on the first public data

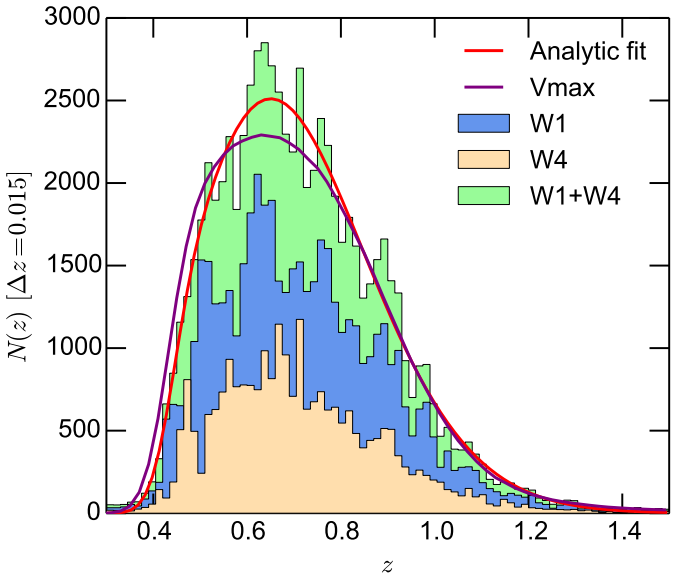

Figure 4.3: Redshift distribution of the VIPERS galaxies, separated in the two fields W1 and W4. The effect of the colour pre-selection is visible as a suppression of the number counts at $z < 0.5$ respect to a pure magnitude-limited sample. The red curve shows the best fit of the combined $N(z)$ using the fitting formula inside (4.1), whereas the purple line shows the radial profile obtained with the V_{max} method (see the next section).

release of the VIPERS sample (de la Torre et al. 2013), it has been found that this shape can be well described by an analytical template like the one that follows,

$$N(z) = \alpha_0 \left(\frac{z}{\alpha_1}\right)^{\alpha_2} \exp\left(-\left(\frac{z}{\alpha_1}\right)^{\alpha_3}\right) CSR(z), \tag{4.1}$$

where α_0, α_1, α_2 and α_3 are free parameters to be fitted on the dataset and $CSR(z)$ (Colour Sampling Rate) is a function that describes the suppression of the number counts at low redshift due to the colour pre-selection. Given that as soon as it reaches $z = 0.6$ the sample is almost complete (very few percent from perfect completeness as specified previously), the profile of $CSR(z)$ can be approximated with an error function, like

$$CSR(z) = \frac{1}{2} - \frac{\mathrm{erf}\left[\beta_1(\beta_2 - \mathrm{z})\right]}{2} \tag{4.2}$$

Figure 4.3 shows the redshift distribution of the galaxy sample collected by VIPERS. On top of the histogram showing the distribution of the full sample (combining data from the two fields), we overplot the best-fitting

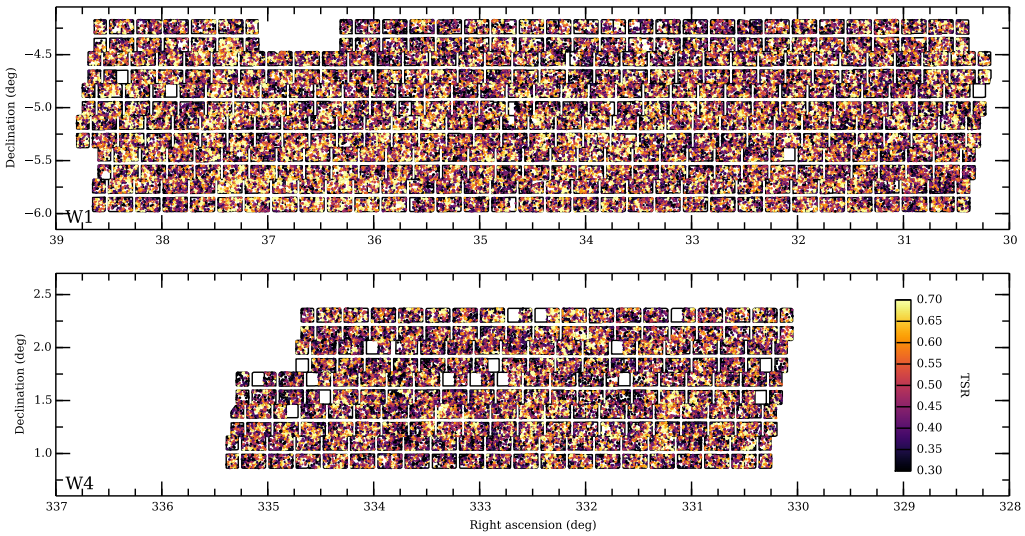

Figure 4.4: Footprint of the spectroscopic masks for the final VIPERS release in the W1 (top) and W4 (bottom) field. The combined effective surface observed by VIPERS amounts to 24 deg^2, and it is shared by the two fields in the ratio 2:1. Observed sources are colour-coded according to the corresponding value of local Target Sampling Rate (see Section 5.1). Empty regions correspond to quadrants that have gone through a failure during the insertion of the corresponding photometric tile.

model using the analytical template of Equation (4.1). Given the necessity of working with a galaxy catalogue complete in the redshift range of interest, in this analysis we consider only galaxies located at $z > 0.5$. This leads to the creation of an effective galaxy sample that is almost complete down to the limiting selection magnitude.

4.2 The VIPERS angular mask

The VIPERS angular selection function is the composition of multiple processes. The main angular limitation is given by the effective sky surface that has been selected for the collection of spectroscopic data. As anticipated in the previous section, these regions fall within the CFHTLS Deep fields, W1 and W4. A schematic representation of the VIPERS spectroscopic fields is provided in Figure 4.4.

Observations have been carried out at the ESO Very Large Telescope (VLT), exploiting the full power of the VIsible Multi-Object Spectrograph (VIMOS, Le Fèvre et al. (2003)). The latter consists of a 4-channel imager and spectrograph, each of the channels being a fully operational spectrograph

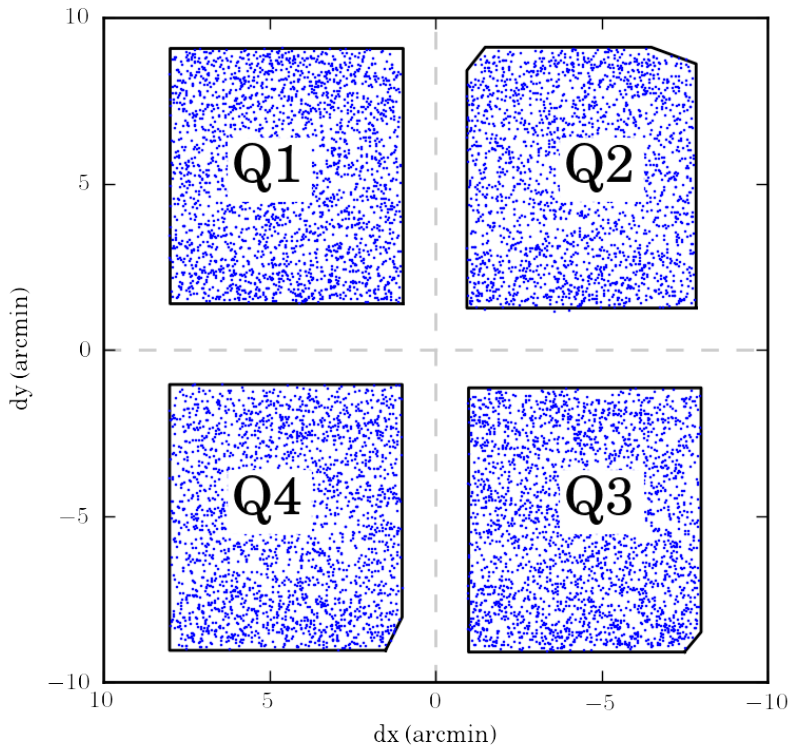

Figure 4.5: Example of the detailed footprint and disposition of the four quadrants in a full VIMOS pointing. Each VIMOS quadrant occupies an area of $7\times8\,\mathrm{arcmin}^2$. Within the central cross-shaped region observations are not performed due to technical constraints. Boundaries of the quadrants are not perfect rectangles, since they are reconstructed pointing by pointing following the borders of the illuminated area.

capable of targeting multiple galaxies at the same time. Each quadrant cover $\sim 7 \times 8\,\mathrm{arcmin}^2$ on the sky, for a total observed area during a single pointing equals to $218\,\mathrm{arcmin}^2$. During the phase of data reduction, the boundaries of each single quadrant are reconstructed following the borders of the illuminated area. In this way, low-sensitivity pixels are excluded from the analysis, leading to a definitely more robust dataset. As an example, in Figure 4.5 we show the typical footprint of a VIMOS pointing.

VIPERS observations have benefited of a single-pass short-slit target selection strategy (Scodeggio et al. 2009). This choice has implied that, among all the possible candidates within each of the VIMOS quadrants, a typical 40% fraction is put under a slit and become part of the final spectroscopic sample. Figure 4.6 shows the disposition of targets within the quadrants of a single VIMOS pointing. Around each selected object, a small rectangle is drawn to highlight the dimension of the spectroscopic slit that has been

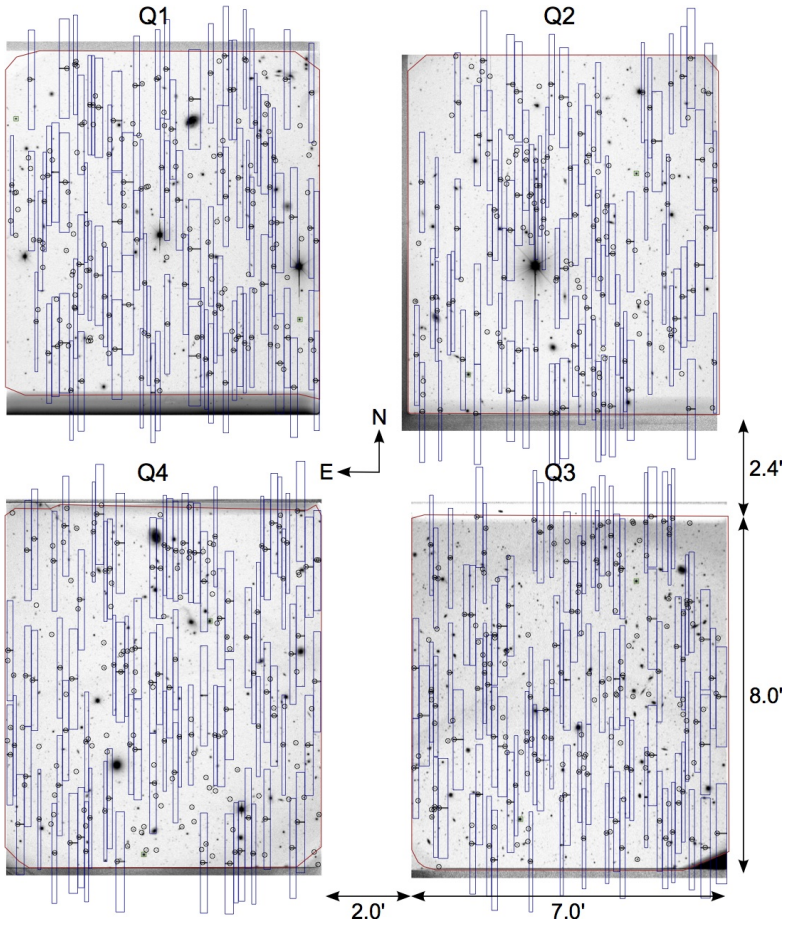

Figure 4.6: Distribution of slits across a single VIMOS pointing (W1P082 in this case). The full set of potential VIPERS target is marked with empty circles. The surface of the photometric tile occupied by slits and raw spectra is marked by empty rectangles. It is clear how the angular distribution of observed galaxies is different from the true underlying distribution.

put on top of the source. A definitely larger rectangle marks the region along which the raw spectrum of the target galaxy is collected (with different wavelengths distributed along the vertical direction). The spectrograph is equipped with the "Low Resolution Red" grism, with an optimal resolution $R = 210$. With these settings, the frequency coverage of the reduced spectra is limited to the optical-infrared band between 5500 and 9500. One of the most important technical innovation of VIPERS is that the data reduction has been performed with a completely automatized pipeline (Scodeggio et al. 2005; Garilli et al. 2008). This implies that the classical handling of the raw spectra, and in particular the search for emission lines required to carry out a redshift measurement, has been performed employing and updating

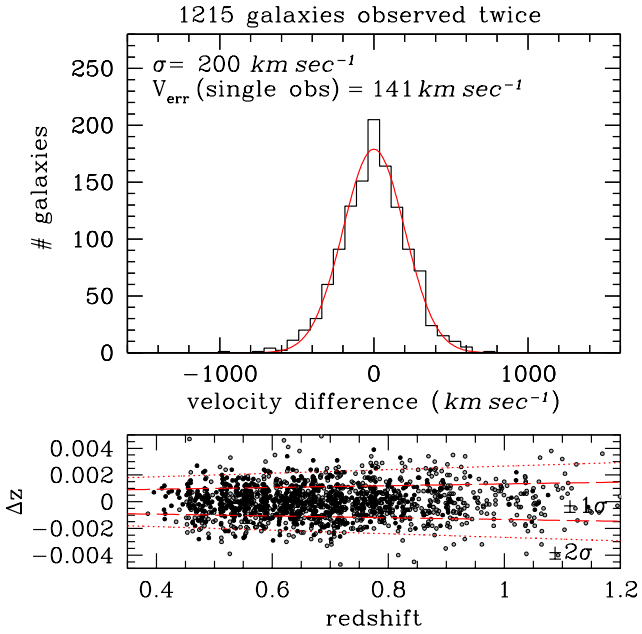

Figure 4.7: Top: distribution of the velocity difference between two independent measurements, computed using a subsample of 1215 galaxies of the PDR-1 with a quality flag > 2. The best-fitting gaussian template is represented by the red solid line and has an intrinsic dispersion of $\sigma_2 = 200$Km/s. This translates in a rms variation for a single source of $\sigma = \sigma_2/\sqrt{2} = 141\,$Km/s. Bottom: the corresponding dispersion of redshift errors, as a function of the redshift itself. It is found that this value can be approximated fairly well by an evolving functional form as $\sigma_z = 0.00047(1 + z)$.

existing algorithms used in precedent VIMOS-based projects. The redshift validation is the only step of the data reduction in which human intervention is required. For a limited subset of the collected data (2275 galaxies with a reliable measured redshift), two independent redshift measurements are performed separately by different teams, in order to assess the reliability of the process of data reduction. This yields an uncertainty on the measured redshifts that follows a normal distribution with $\sigma_z = 0.00054(1 + z)$ (updating the old PDR-1 estimate as in Figure 4.7). This redshift error can be translated in an additional component $\sigma_v = 160\,\mathrm{Km\,s^{-1}}$ ($141\,\mathrm{Km\,s^{-1}}$ in the PDR-1) to the intrinsic dispersion of the galaxy velocity field. Figure 4.7 shows the distribution of velocity difference for the two independent measurements of the PDR-1 subsample, with the best-fitting gaussian model overplotted to the data. During the data reduction, a quality flag is assigned to the measured redshifts with a double purpose: the first one is to classify each object according to its morphology (galaxy/AGN/star), while the sec-

ond one quantifies how much reliable is the extraction of the redshifts from the raw spectra. In this work, we consider only galaxies with quality flags between 2 and 9, that corresponds to a redshift confirmation rate of 98%.

4.3 The VIPERS mocks

The production of a statistical analysis like the one presented in this work requires multiple alternative realisations of the volume probed by the survey. This call is motivated mainly by the pressing need of a safe and robust description of the errors for the galaxy clustering statistics. Computational physics has largely dealt with the improvement of statistical methods to estimate the amplitude of errorbars for a certain physical quantity, and among them we can cite popular resampling methods such as the jackknife and the bootstrap (Efron 1982). Nevertheless it has been proved (Norberg et al. 2009) how all of these techniques constantly underestimate the error with respect to a more accurate statistical analysis where many alternative realisations of the same volume are available. This is the reason for making use of a set of 153 independent mock samples covering both the W1 and W4 fields, that are constructed simply by populating a large N-body simulation with galaxies using Halo Occupation Distribution (HOD) prescriptions.

The realisation of this set of mocks has been achieved taking advantage of the Big MultiDark Planck (BigMDPL, Prada et al. (2011)) run, which belongs to the series of LCDM simulations featuring a flat Planck-like cosmology. The cosmological parameters adopted by the simulation are $\Omega_m = 0.307$, $\Omega_b = 0.048$, $\Omega_\Lambda = 0.693$, $h = 0.678$ and a spectral tilt $n = 0.96$. The amplitude of linear rms fluctuations within spheres of radius $8\mathrm{Mpc}/h$ is set to $\sigma_8 = 0.823$ at $z = 0$. The simulation starts at $z = 120$ and uses a set of 3840^3 dark matter particles, distributed within a cubic box of comoving size $2500\,h^{-1}\,\mathrm{Mpc}$. The particle mass resolution is $2.4 \cdot 10^{10}\,h^{-1}\,\mathrm{M}_\odot$, and the gravitational softening length changes from 30 to $10\,h^{-1}\,\mathrm{kpc}$ moving to the low-z snapshots. Halos in the simulation are identified using a FoF algorithm with a relative linking length of $l_l = 0.20$. This implies that the mass limit to which halo catalogues can be considered complete is $\sim 10^{11.9}\,h^{-1}\,\mathrm{M}_\odot$. This prevent us from populating halos with the faintest galaxies observed with VIPERS, and for this reason, we follow the technique described in de la Torre & Guzzo (2012) to reconstruct dark matter structures below the resolution limit. By applying this reconstruction method, we are able to push the completeness of the halos within the simulation down to $10^{10}\,h^{-1}\,\mathrm{M}_\odot$, allowing to reproduce the least massive galaxies that fall within the survey selection criteria. VIPERS-like lightcones are subsequently constructed by

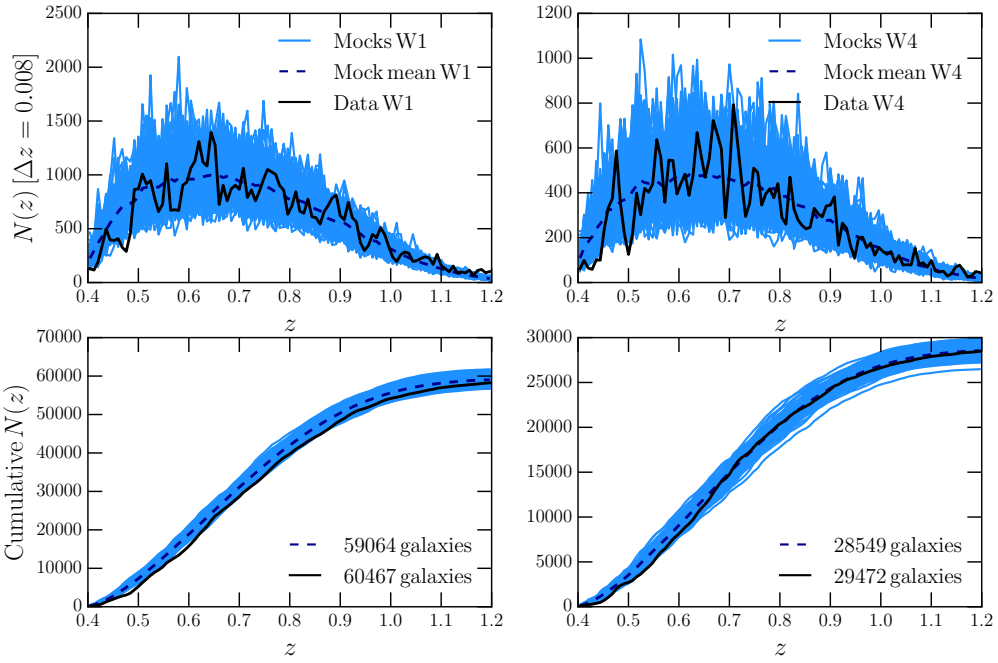

Figure 4.8: Top: comparison between the redshift distribution of VIPERS data and the realistic set of 153 independent mock catalogues. The left/right panel shows results for the W1/W4 field. In order to highlight the excellent agreement between data and mocks, the mean value is plotted as the blue dashed line. Bottom: cumulative redshift distribution of the VIPERS dataset and the 153 mock samples. The legend shows also the excellent agreement between the total number of galaxies between the two realisations (data and mock average).

appending neighbour circular sectors coming from different snapshots of the simulation.

All the radial and angular selection criteria are applied to the resulting mocks, in order to fully reproduce the geometrical properties of the VIPERS data. Further details about how the VIPERS mocks have been realised can be found in de la Torre et al. (2013). The resulting redshift distribution of these set of mocks is plotted in Figure 4.8, where it is also compared to the corresponding radial profile of the VIPERS dataset, showing a good agreement between data and simulations over the full redshift range probed by the survey. At the same time, the mean number of objects populating the mocks is close to the expected number of galaxies observed by VIPERS. In addiction to this realistic set of VIPERS-like mocks, the team has also constructed a parallel set of mocks that does not feature the VIPERS target selection, and which are typically referred to as parent mocks. The main reason at the basis of this choice is that in this way we can test and quantify the impact

of several systematic errors affecting both the measurements obtained with VIPERS (like the target selection, which is the central part of the next section) and the theoretical models that try to give an approximated description of a still not fully understood physical effect such as redshift-space distortions (as already described in the previous chapter).

Chapter 5

MEASURING THE 2PCF FROM THE VIPERS DATASET

5.1 Handling of the angular selection function

As explained in the previous section, the angular distribution of the VIPERS dataset is the results of the combination among multiple angular selection functions. In detail, the target selection can be summarised in the following three steps:

1) Redshifts are collected in a well-defined pattern produced by the combination of multiple VIMOS pointings (288 whereof 192 make up W1 and 96 make up W4) with the particular footprint of a VIMOS exposure. The surface scanned by the observations is not a pure montage of rectangular quadrants though, since the probability of targeting an object falling within a VIMOS quadrant with a high signal-to-noise ratio rapidly falls down as long as we approach the boundaries of the channel. The main motivation of this technical bias can be attributed to the presence of hot and black pixels nearby the edges of the CCDs, affecting the quality of the deduced light signal within those spots.

2) A fraction of the total number of targets potentially ends up within bad photometric regions, most of them corresponding to a line of sight that is already covered by a luminous star. This stellar component is tracked using cross-shaped polygons with a central core that corresponds to the region where the signal is completely saturated. Subtracting these bad quality regions from the mosaic described in the previous step leads to the definition of the effective surface where observations have been carried out.

3) Among the remaining potential targets, only a $\sim 40\%$ fraction is actually put a slit and targeted for spectroscopy. This fraction is usually referred to as Target Sampling Rate (TSR), and is defined as the ratio between the number of collected spectra over the one of total targets. TSR can be defined independently for different VIMOS quadrants, since by construction the ratio is mostly sensible to the underlying projected galaxy density field, which can experience variations among the different pointings. Of the measured redshift, a non-negligible fraction is assigned a spectroscopic flag, marking the quality of data reduction, that does not lay above a preselected critical threshold. This fraction is assigned the name of Spectroscopic Success Rate (SSR), and can be numerically defined as the fraction of observed sources whose corresponding redshifts have a good quality flag. This last selection firstly accounts for any failure in the insertion of the slits and for any similar technical anomaly which leads to the loss of a consecutive slice of data. In addiction, it also takes care of the statistical uncertainty in measuring redshifts through galaxy emission lines. This clearly makes the SSR a strong function of galaxy morphological features, like colour and magnitude, and of the redshift itself.

The mixture of these different selections cannot be neglected, but must be properly taken into account. This turns out to be essential if one wishes to perform a statistical analysis using a dataset whose members have undergone the full selection pipeline described so far.

The survey effective area can be easily identified thanks to the help of a binary mask (in/out) that closely follows the distribution of VIMOS pointings across the W1 and W4 field. The non-uniform sensibility of the pixels nearby the edges of the CCDs is also considered in a proper way. For this issue, the team has worked out a specific detection algorithm that adjusts the geometry of each panel simply by following the borders of the illuminated area. The presence of bright stars along the line of sight can be included in the analysis after the application of a second binary mask, which accounts for any defect inside the photometric sample. The combination of these masks ultimately leads to the construction of a peculiar mosaic pattern (as shown in Figure 4.4), that represents the effective sky area of the survey. The resulting window function can be taken into account fairly easily, simply by applying the same binary masks to the random sample used to estimate the two-point correlation function (see Section 2.2).

In a statistical sense, and more precisely looking to the amplitude of the correlation function, the most important difference among the previous three points is that, whereas 1) and 2) are responsible for a global selection effect that can be replicated in the random sample with a in/out strategy, the

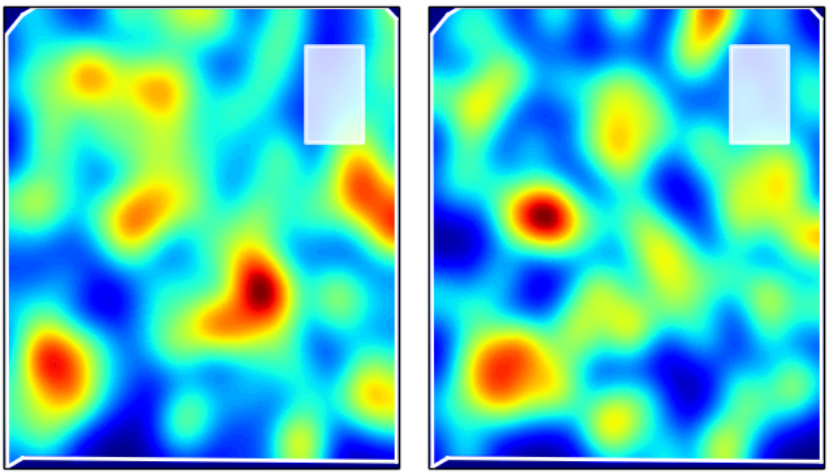

Figure 5.1: Comparison between the reconstructed projected density field on the sky of one of the VIMOS quadrant. High- and low-density regions are marked by redder and bluer colors respectively. The white border mark the reconstructed boundaries of the considered quadrant. White rectangles represent the angular mask adopted to compute the local TSR (as the following sections will properly explain).

impact of 3) on the clustering turns out to be definitely more ambiguous. As a matter of fact, in this case the selection of targets within a single VIMOS quadrant cannot be applied directly to the random sample since the selection is applied to single targets rather than on a common portion of volume. In addiction, the selection of targets applied by VIMOS is not able to provide a galaxy sample which faithfully reproduces the true distribution of sources within W1 and W4. Figure 4.6 shows the distribution of slits across the quadrants of one of the typical VIMOS pointings. As one can observe, slits are placed in a way that maximises the total number of objects within the quadrant. Unfortunately, side effect of this choice is not to fully maintain the angular clustering of the underlying galaxy field (as shown in Figure 5.1).

The resulting angular selection function leads to the suppression of the clustering amplitude (in the full set of n-points statistics, like correlation functions, power spectra, etc). Figure 5.1 shows the impact of the angular selection function on the amplitude of the real-space two-point correlation function when using the mean value of the 153 mock samples. The blue line shows measurements once 1) and 2) are applied to the parent mocks, whereas the purple line does the same considering all three kinds of selection. As for the first selection, we do not observe any deviation from the predictions obtained with the parent mocks (the blue line is fully compatible with 0 given the size of the errorbars), but unfortunately the same is not true once the third effect is included. Indeed, although most of the damping is located

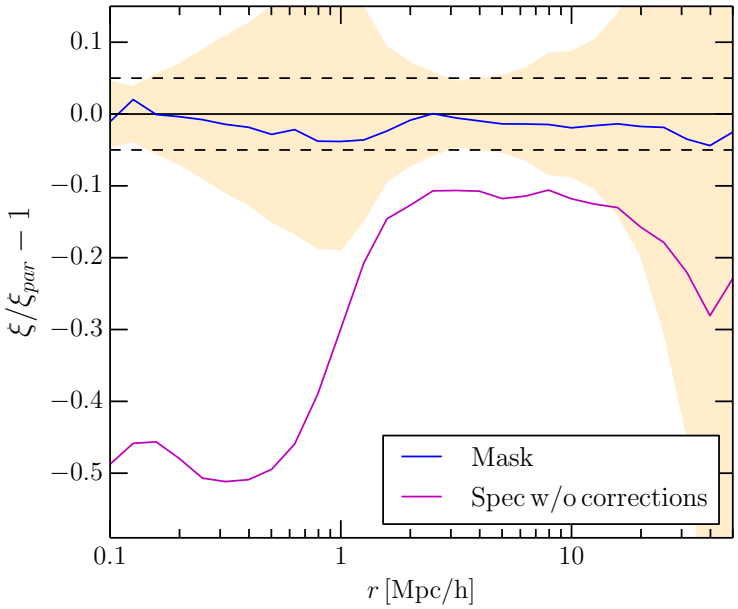

Figure 5.2: Systematic fractional error on the real-space two-point correlation function. The correlation function of the parent sample (black solid line) is used as reference. The blue solid line represents the systematic error on the masked sample (points 1) and 2) in our classification) once both binary masks are applied to the random sample. This correction is able to recover completely the underlying signal on the overall scale range. The same is not true for the selected sample (point 3) also added), whose correlation function is represented by the magenta solid line. The shaded area corresponds to the intrinsic rms noise of the parent signal.

below $1h^{-1}$Mpc, at larger scales we can still observe a systematic shift of about 10%. This is a very unsuitable feature, since it is right above these scales that we want to carry out cosmological tests and fits of the growth rate. For this reason, it is of vital importance to give a full characterisation to the dynamics of such damping, in particular if one wishes to perform high-precision cosmology with the current dataset.

Therefore, the selection of targets inside quadrants requires more attention. In the next subsections we focus on both getting a better understanding of these selection effects and finding a good correction capable of recovering the correct clustering signal.

5.1.1 Small-scale incompleteness

VIPERS is designed to target galaxies in a very broad redshift range using a single-pass observing strategy. Candidate targets are assigned slits

by an automatized algorithm, SSPOC, which maximises the number of slits in a given quadrant. This operation is not completely free, since typically multiple slits are placed along the same columns. This limitation is required to facilitate the subtraction of the residual sky background from the galaxy spectra during the data reduction.

Given that the slits have an average physical dimension of $w = 7$ arcsec, and that the spectrum of a target galaxy cannot be placed on top of a second target (because of the overlapping of the two spectra), two close-ranged objects on the sky cannot be both targeted for spectroscopy (a problem very similar to fiber collision in modern CCDs equipped with optical fibers instead of slits). Figure 4.5 shows one of the typical footprint of a VIMOS exposure, with slits and spectra represented by blue rectangles.

The previous effect can be recast saying that there is an angular scale defined by the typical width of the slit and the height of a spectrum within which most of the clustering amplitude is lost. This effect is unavoidable and is responsible for the damping of the correlation function amplitude on very small angular scales ($<\sim 1$ arcmin).

In order to validate our hypothesis, we perform a simple test able to isolate the spectra masking effect. We have built up a toy model, randomly populating with galaxies a spherical surface surrounding a candidate target placed at $z = 0.8$ (which roughly corresponds to the median redshift of the observations). Then we compute the fraction of galaxies laying on the spherical surface that are obscured by the shadow of the spectrum of the central target. This quantity is a strong function of the position of the object on the sphere (we can define an angle θ between the line of sight and the radius vector, as depicted in the left plot of Figure 5.3), as the geometry of the galaxy spectrum will be more likely to obscure galaxies with $\theta \sim 0$. Not only, but equatorial pairs will be less affected by the masking effect than azimutal ones. We perform this simple test using two different radii for the sphere, i.e. 1 and 10 Mpc, in order to establish if the masking effect is responsible not only for the small-scale damping but also for the large-scale uncompleteness. The right plot of Figure 5.3 shows these results: we compare data computed from the mock samples with theoretical predictions for the fraction of lost pairs due to the masking effect of the targeted galaxy spectrum. The top panel shows the results for the 1 Mpc radius sphere, whereas the bottom panel focuses on a 10 Mpc radius sphere. A quick analysis of the plot makes clear how the galaxy pair count for the large sphere is insensitive to the *shadow* of the spectrum, while this effect becomes definitely more important at smaller scales, where we observe a damping of the count of pairs which are aligned with the line of sight.

A more quantitative understanding of the spectra masking effect can be

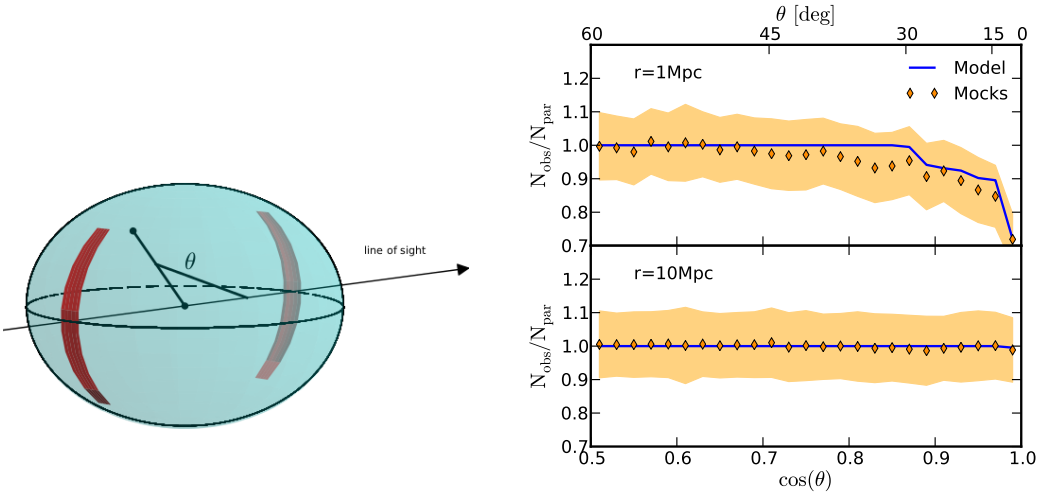

Figure 5.3: On the left: sketch of the toy model we have built up to characterise the spectrum masking effect. Red stripes mark the regions obscured by the spectrum of the central object. θ represents the angle between the line of sight and the pair separation vector (where the central galaxy is a fixed member of the pair). On the right: comparison between the number of lost pairs predicted from the simple spherical surface toy-model and measured from the mean signal of the mock samples. The top and bottom panels show results respectively for spheres of radii 1 and 10 Mpc.

achieved observing how the angular correlation function is modified as soon as the target selection is applied to the parent mocks. The angular correlation can be defined in a similar way to the two-point one, with the only difference being the use of an angular separation rather than a physical one (see Section 2.2). The usefulness of working with angular quantities is twofold: first, we do not have to worry about converting angular coordinates in a comoving frame using a fixed cosmological model, and secondly, we can observe the true angular clustering also for the actual dataset, since only angular coordinates are required. These quantities are ready to be used inside the photometric catalogue. Figure 5.4 illustrates the impact of the target selection on the recovered angular clustering. In the top panel of the left plot, we show the angular correlation functions of both the parent and the spectroscopically selected catalogue. Some first comments can be made on this plot: the selection of targets does not affect the amplitude of the angular correlation function above an approximated separation of $\theta \sim 150\,\mathrm{arcsec}^2$, that roughly corresponds to the height of the VIMOS projected spectra. On the contrary, angular scales below this separation have a lower clustering amplitude, since some of the underlying galaxy pairs start to be obscured by the shadow of the target spectra. Eventually, the scale we are probing will become smaller than the typical width of the slit ($w \sim 7\,\mathrm{arcsec}^2$) and the angular clustering

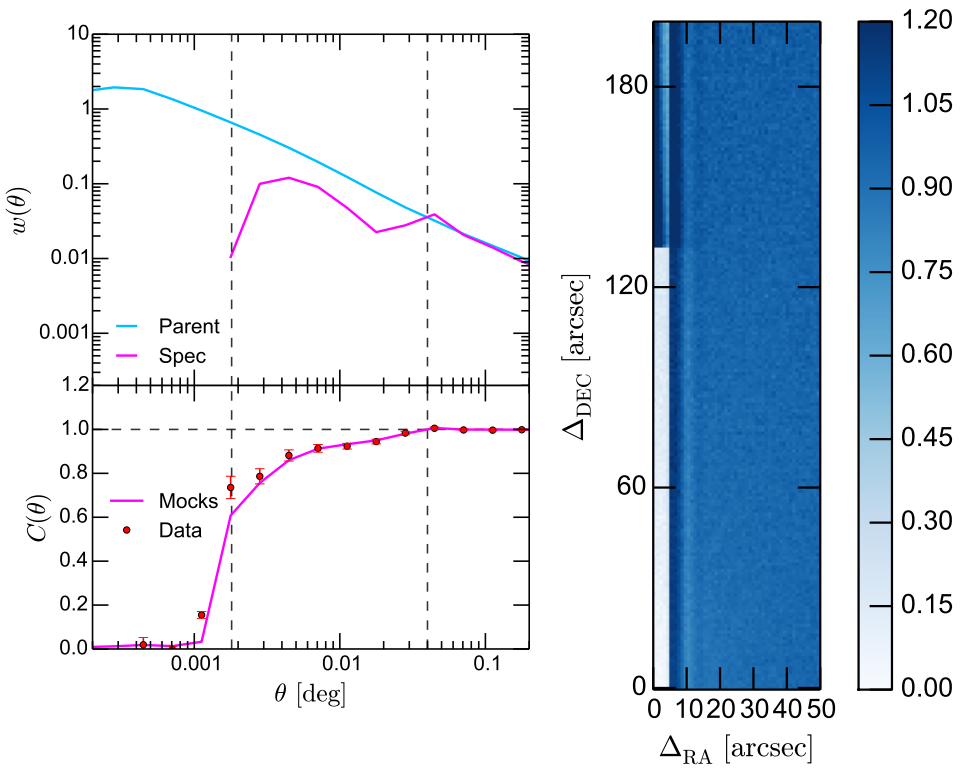

Figure 5.4: Top left: comparison between the angular correlation function of the parent and selected mocks catalogues (the mean value is plotted to increase the signal to noise ratio). The two vertical dashed lines represent the angular size of the slit (left one) and the height of the spectra (right one). Bottom left: one-dimensional angular completeness, defined as the ratio between the number of pairs of the selected and the parent sample. The horizontal dashed line simply marks the 100% completeness. Red markers show the corresponding function computed directly on the VIPERS dataset. Right: two-dimensional angular completeness, as a function of the RA and Dec angular separation. The white rectangle at small separations highlights the shadow of the target spectra. The increase of correlation at small separations in RA and large separations in Dec shows the preferential selection of targets along the same columns.

will vanish almost completely (there are still some few pairs because targets are not necessarily at the center of the spectroscopic slits). The two dashed lines mark exactly the scales corresponding to these values. In the bottom panel, we plot the one-dimensional completeness function, defined as

$$C(\theta) = \frac{1 + w_s(\theta)}{1 + w_p(\theta)}, \tag{5.1}$$

where $w_p(\theta)$ and $w_s(\theta)$ are the usual angular correlation functions of the photometric and the selected sample. This function simply makes more visible

the masking effect of the spectra, and can be used to correct for part of the missing power at small separations (below $\sim 1\,h^{-1}\,\mathrm{Mpc}$). The right panel of Figure 5.4 shows the two-dimensional completeness function $C(\mathrm{RA}, \mathrm{Dec})$, deprojected along the orthogonal axes identified by RA and Dec. In this case, we can recognise the imprint of the target spectra on the angular correlation as the quasi-zero complete white rectangle in the bottom left corner of the plot. In addiction, given the preferential disposition of multiple slits along common columns (as previously described) we notice an apparent excess of completeness right above the shadow of the spectra.

The approach used to partially correct for this masking effect has been already used in precedent works, such as for the 2dFGRS (Hawkins et al. 2003), BOSS (e.g. Reid et al. 2014), WiggleZ (Blake et al. 2008, 2010) and the first public data release of VIPERS (de la Torre et al. 2013). The method consists in a galaxy pair upweighting, based on the measured one-dimensional completeness. Namely, for each galaxy-galaxy pair, we can calculate the pair angular separation θ_{ij} as

$$\theta_{ij} = \frac{\boldsymbol{r}_i \cdot \boldsymbol{r}_j}{\|\boldsymbol{r}_i\| \, \|\boldsymbol{r}_j\|}, \tag{5.2}$$

where $\boldsymbol{r}_i$ and $\boldsymbol{r}_j$ correspond to the separation vector between the observer and the i-th and j-th galaxy. Subsequently, we can upweight the galaxy pair by the inverse of the corresponding value of completeness, that is

$$w_{ij}^{A} = \frac{1}{C(\theta_{ij})}. \tag{5.3}$$

Note that inside Equation 5.2 we do not require perfect knowledge of the radial distance of targets, since the latter can be factorised out and simplified between numerator and denominator.

It has been proven that this approach is capable of recovering a large fraction of the missing clustering signal coming from the 1-halo contribution of the two-point correlation function, and therefore we have tested its application to the VIPERS final measurements. Moreover, the computation of the angular completeness function does not require any information on the underlying cosmological model, and thus it can be applied without biasing our results towards a particular cosmology. Clearly, there could be an intrinsic dependence of $C(\theta)$ on redshift, but we are not considering it, since a precedent test performed in de la Torre et al. (2013) showed no significant improvement respect to using the redshift-averaged completeness, at the expense though of introducing additional noise to the measurements.

5.1.2 Large-scale uncompleteness

A complementary effect of having a physical limitation like the shadow of the spectra during the targeting of a subset of sources is that the selection function becomes strongly density-dependent. This happens because high-density peaks of the projected galaxy density field are undersampled with respect to low-density regions. Indeed, it is definitely more likely to target objects that are separated from their neighbours by more than the limiting separation (the width of the slit), rather than objects that are tightly close together. This effect, if not carefully corrected for, is responsible for the almost constant suppression of the two-point correlation function amplitude on scales above $1\,h^{-1}\,\mathrm{Mpc}$ (see Figure 5.1). Given that a precise and accurate modelling of the one-halo term is still unrealisable (unless to employ fitting formulae that have previously been tuned to simulations, that regardless can suffer of uncertainties in the transition from matter particles to galaxies) and thus the fit of cosmological parameters using RSD is usually performed on scales above $1\,\mathrm{Mpc}/h$, the attention of this work has been particularly focused on the correction of this selection effect, rather than on the small-scale masking effect.

In order to isolate the non-homogenous sampling from the masking effect depicted above, we perform a simple test based on the depletion of the masked sample, that is, the one featuring only the mosaic of quadrants created by sticking together different VIMOS pointings (this corresponds to the blue line in Figure 5.1). The depletion is realised with two different prescriptions: in the first case, we simply remove galaxies randomly until we are left with the 40% of the original number, and in the second case, we repeat the process using the projected local density around each galaxy as a selection criterium to decide whether to keep or not the target. This second depletion mimics the global systematic effect introduced during the selection of targets, but allows for the presence of galaxy pairs with an angular separation smaller than the slit width. A proxy for the local density on the sky can be obtained simply counting the number of neighbours that fall within a fixed angular mask centered on the considered galaxy. Clearly, the size of the angular mask has an impact on the recovered clustering, but in this case we are interested only in understanding if the density-dependent selection is responsible for its suppression at large separations. Figure 5.5 shows the results for the real-space two-point correlation function. Measurements of $\xi(r)$ from the uniformly depleted sample show a perfect consistency with the original masked catalogue. The only difference is a significantly larger shot noise contribution to the signal, since we are using a statistically worse sample (by reducing the number of objects). On the contrary, once we con-

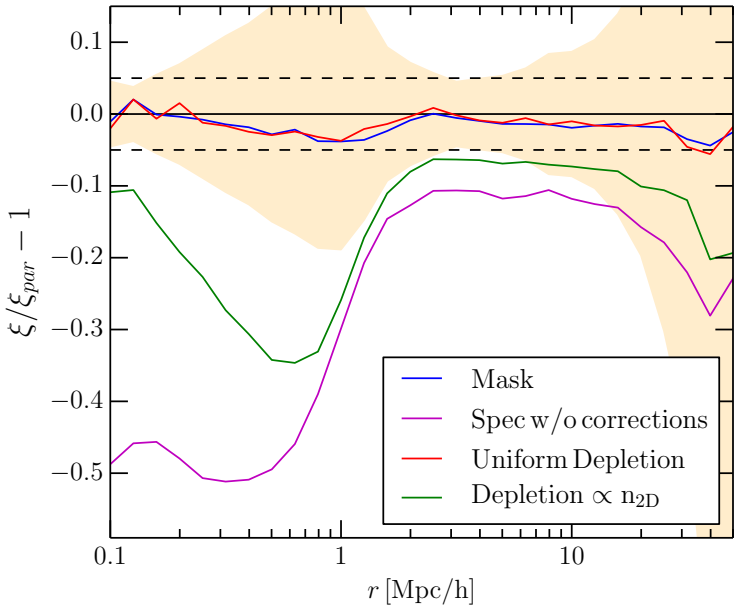

Figure 5.5: Systematic fractional error on the real-space two-point correlation function. In addiction to the lines already shown in Figure 5.1, here the two additional lines refer to the case of a uniform depletion and a density-dependent depletion of the sample featuring only the subdivision in the VIMOS quadrants. In both cases, the masked sample has been depleted leaving the 40% of the total galaxies, mimicking the selection effect undergone by the data. The plot shows immediately how the choice of a density-dependent depletion introduces the constant suppression of the clustering amplitude on scales above 1, h^{-1} Mpc.

sider the second subsample, we notice an overall suppression of the clustering amplitude above 1 h^{-1}Mpc, which resembles the one obtained using the spectroscopically selected sample. We impute the different height of the plateau to the selected size of the angular mask (a circle with radius $r = 50$ arcsec in this case). We can try to repeat the same procedure using a smaller mask, but in that case we introduce a larger noise. Nevertheless the overall trend of the height of the plateau is an increase of the systematics as long as smaller angular masks are selected to estimate the local projected density.

From this simple test, we have understood how the systematic effect on large scales is generated because of the different sampling between high- and low-density regions. The correction of this selection effect has been performed starting from the original approach used in de la Torre et al. (2013). The latter basically consisted in a galaxy upweighting based on the corresponding value of Target Sampling Rate (TSR), namely

$$w_i = \frac{1}{\mathrm{TSR_i}}, \tag{5.4}$$

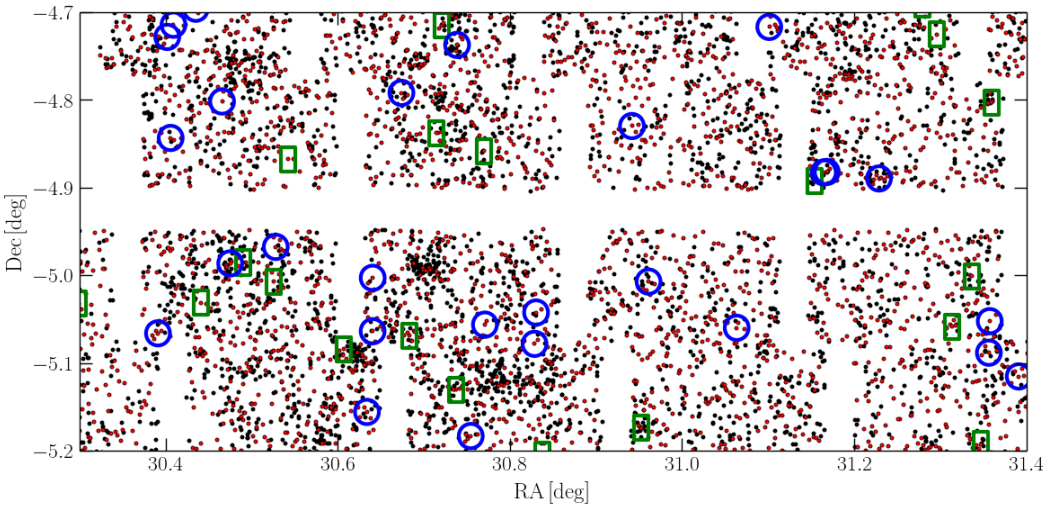

Figure 5.6: Simple sketch showing the method employed to compute a local TSR for each spectroscopically selected object through a portion of the W1 field. Around each spectroscopically selected (red points) we put an angular mask, either circular or rectangular, and compute the ratio between the projected density field integrated within the mask of the selected sample over the one of the total sample (that is, also adding the black points). The prescriptions used to have a proxy for the density field are two, a simple number counts and a tessellation of the discrete density field.

where TSR was considered to vary from quadrant to quadrant. In this way, all the targeted galaxies falling in a same quadrant would have been upweighted by the same quantity. Some of the results from de la Torre et al. (2013) showed that this procedure was recovering only a fraction of the total missing power, mainly because the sampling of targets starts to be relevant on scales well below the one of VIMOS quadrants. Our corrective approach is similar, but in this case we have defined a quantity, called local TSR, that accounts much more effectively for the inhomogeneity of the angular selection function. The raw approach for the computation of the local TSR consists in an evaluation of the local projected density field around each target, before and after having applied the target selection. If we call these quantities δ_i^p and δ_i^s, the definition of local TSR comes out quite intuitively as

$$\mathrm{TSR}_i = \frac{\delta_i^s}{\delta_i^p}. \tag{5.5}$$

We have employed small angular masks centered around each selected source in order to define a local properties which is different from target to target, similarly to what has been already used for the depletion test. Size and shape

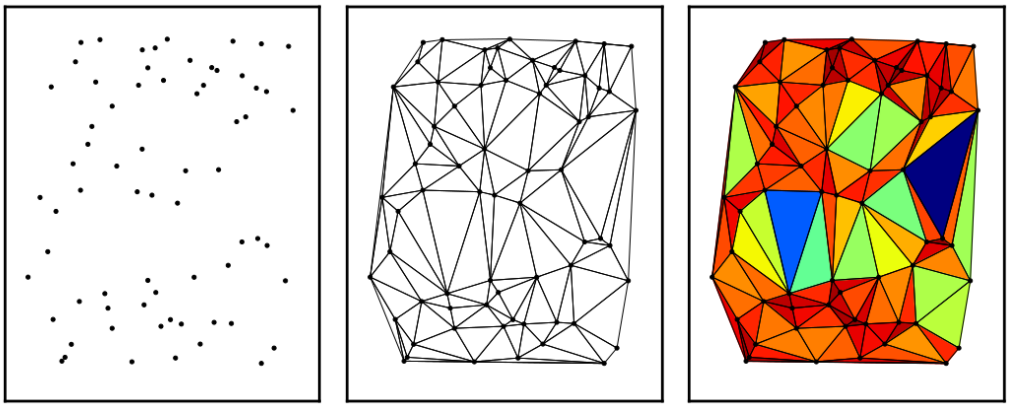

Figure 5.7: Scheme for the realisation of a Delaunay tessellation. The set points laying in a two-dimensional space (left panel) can be connected giving birth to a single triangulation (middle panel). Each of the original points can be assigned a density defined as the sum of the inverse of the area of the triangles having the considered point as vertex. Using a linear 2D interpolation, it is possible to estimate the density field continuously at each position in the two-dimensional space.

of the masks have an impact on the recovered local TSR, and for this reason we have tested different combinations using our mock catalogues. We have also tested two different proxies for the projected galaxy density field:

1) Number counts: the local density is just the number density of discrete points falling within the mask. Figure 5.6 shows a nice example of how this procedure is implemented.

2) Delaunay tessellation: a smoother estimate of the density field can be obtained, first performing a triangulation of the discrete set of points, and then assigning a density to each node depending on the areas of the triangles having the node as vertex (Figure 5.7). Subsequently, a linear interpolation is capable of producing a value of the density field continuously throughout the sky plane, and the integral of this function over the mask can be used as a proxy for δ.

Weights computed using the triangulation method are shown for the VIPERS dataset in Figure 4.4, where each observed source has been coloured according to its corresponding value of local TSR. It is possible to observe how single quadrants have a strong internal inhomogeneity in the sampling of galaxies, otherwise we should expect almost monochromatic quadrants.

A simple application to the mocks shows how both strategies are capable of recovering completely the clustering amplitude above $1\,h^{-1}\,\mathrm{Mpc}$, with the triangulation method introducing a slightly smaller noise in the recovered

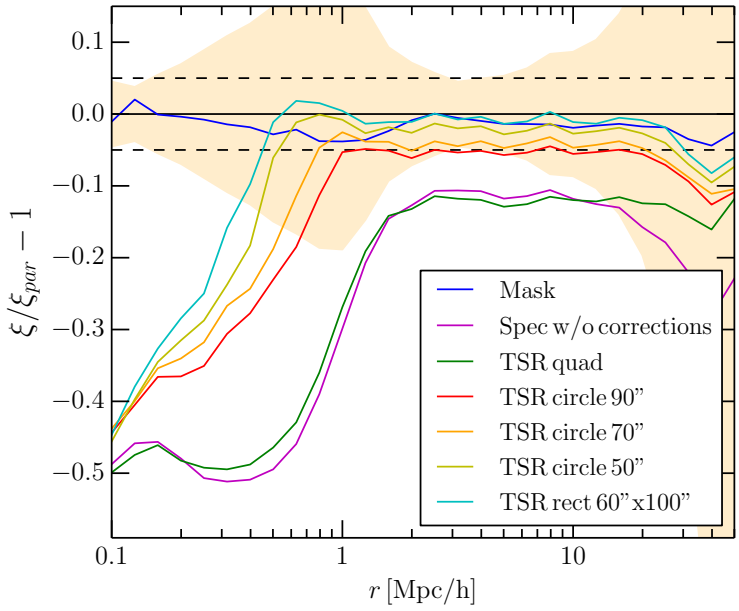

Figure 5.8: Systematic fractional error on the real-space two-point correlation function. In addiction to the lines already shown in Figure 5.1, here we show the results for different configurations of the mask geometry and size. The test is performed using three circular mask with radius $r = 90$, 70 and 50 arcsec, and one rectangular mask with size $60 \times 100\,\mathrm{arcsec}^2$. We also provide the output using the quadrant-averaged TSR, which shows no significant improvement on the scales we want to correct.

two-point correlation function (mostly due to the use of smooth quantities rather than discrete counts). Therefore we have decided to adopt this second approach to generate a catalogue of individual weights. Figure 5.8 shows results of the correction using different geometries and sizes for the galaxy masks. In detail, we test a circular and a rectangular aperture, with variable sizes. In each case, the recovery of the clustering amplitude is guaranteed above the correlation length, with a consistent improvement with respect to the quadrant-averaged TSR approach. We argue that a rectangular mask can account with much more efficiency to the angular anisotropy in the distribution of targets within a quadrant introduced by the particular shape of the target spectra (see Figure 4.6 and 5.4). Therefore, for the data analysis, we select the rectangular profile with size $60 \times 100\,\mathrm{arcsec}^2$ (a smaller aperture could still introduce shot noise, even using the method of triangulation). Figure 5.9 shows the impact of correcting the real-space power spectrum for the large-scale clustering suppression, as obtained in a parallel VIPERS analysis on the galaxy power spectrum (Rota et al. 2016). Also in

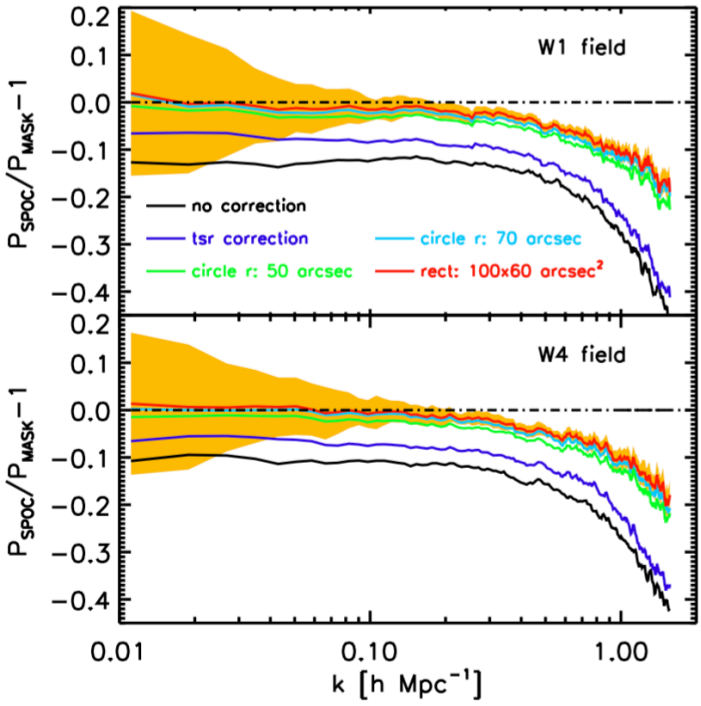

Figure 5.9: Systematic fractional error on the real-space power spectrum measured using the average signal collected from the VIPERS mock catalogues (Rota et al. 2016). In this plot we show results for the unweighted case (black line), and the ones weighted by the quadrant-averaged TSR (blue line) and the local TSR (green, cyan and red lines). The power spectrum measured from the masked sample (subdivision in pointings and quadrants only) is used in this case as a reference model, rather than the parent power spectrum. The orange shaded area shows the rms error of the reference spectrum. The two panels shows results independently for the W1 and W4 field.

this case, we can clearly recognise an almost perfect correction (few percent up to $k_{\rm max} \sim 0.25\,h\,{\rm Mpc}^{-1}$) when adopting the local TSR as a proxy for the projected galaxy density field.

As for the small-scale correction, angular positions are the only coordinates required to compute the weights. It follows that it is possible to perform the correction also on the VIPERS dataset, using the information coming from the photometric sample. This approach of correcting for the target selection looks similar to the one adopted to correct for fiber collisions in the BOSS survey (Anderson et al. 2012), in which the redshift of the nearest neighbour was assigned to the galaxies that were missing a measurement. Alternative approaches can be found, such as using the projected correlation function $w_p(r_p)$ to compute weights (White et al. 2011) or the presence

of overlapping plates to directly predict the correlation function of collided fibers (Guo et al. 2014).

5.1.3 Final correction of the angular selection

The final correcting scheme for the systematic bias introduce during the target selection can thus be recap saying that each galaxy is upweighted by its corresponding value of local TSR defined in Equations (5.4) and (5.5), and each galaxy-galaxy pair is upweighted by the angular weight defined in (5.3). This leads to the following prescriptions to compute the number counts required for the two-point correlation function,

$$GG(r) = \sum_{i=1}^{N_G} \sum_{j=i+1}^{N_G} w^A(\theta_{ij}) w_i^{TSR} w_j^{TSR} w_i^{SSR} w_j^{SSR} \Theta_{ij}(r), \tag{5.6}$$

$$GR(r) = \sum_{i=1}^{N_G} \sum_{j=1}^{N_R} w_i^{TSR} w_i^{SSR} \Theta_{ij}(r), \tag{5.7}$$

$$RR(r) = \sum_{i=1}^{N_R} \sum_{j=i+1}^{N_R} \Theta_{ij}(r), \tag{5.8}$$

where $\Theta_{ij}(r)$ is a simple step function that is unity if the distance modulus s_{ij} falls within $[r - \Delta r, r + \Delta r]$ and zero otherwise. The additional weight w^{SSR} is takes into account how the VIPERS redshifts have been collected with non-homogeneous quality (either different observing conditions and intrinsic galaxy properties). These weights are computed distributing galaxies within a three-dimensional parameter space (photometric redshift, absolute U magnitude and $U - V$ colour) and assigning to each bin of the parameter space a value of success rate (basically counting how many sources inside the bin were optimally observed with respect to the total number). This value can be inverted similarly to what has been done for the Target Sampling Rate, defining the corresponding SSR weights.

In order to validate our correcting scheme, we test the impact of the corrections directly in redshift-space, using the first two even multipoles of the expansion over the Legendre polynomials, $\xi^{(0)}(s)$ and $\xi^{(2)}(s)$. We separate our mock catalogues into the low and high redshift bin (respectively $0.5 < z < 0.7$ and $0.7 < z < 1.2$) and test separately the correction over the two redshift ranges. Results are shown in Figure 5.10. The combined correction (small-scale completeness and local TSR) is capable of recovering the amplitude of the monopole at the 2% down within the Mpc scale, producing an quasi-unbiased estimate of $\xi^{(0)}(s)$ on the comoving scales that we

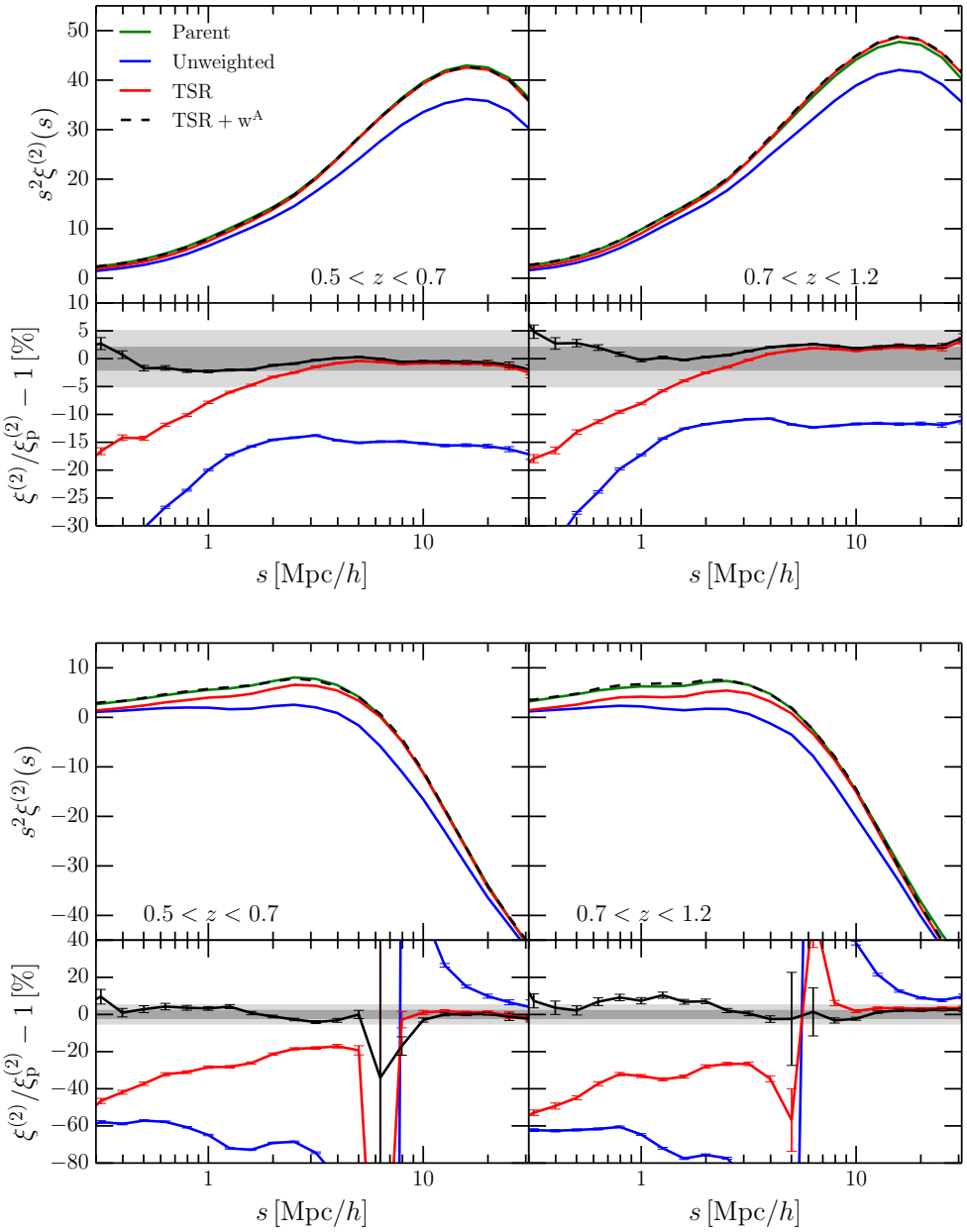

Figure 5.10: Systematic fractional error on the redshift-space two-point correlation function using the mean value of 153 mock samples. The top figure shows results for the monopole $\xi^{(0)}(s)$, while the bottom one does the same for the quadrupole $\xi^{(2)}(s)$. Left/right columns refer to the low($0.5 < z < 0.7$)/high($0.7 < z < 1.2$) redshift bin. The light/dark grey bands of the bottom panels show respectively the 5%/2% systematic deviation from the fiducial value.

wish to use for the RSD fitting. As for the quadrupole, we are able to have a reliable measurement of $\xi^{(2)}(s)$ (5% deviation from the fiducial value at maximum) down to some Mpc. This is an encouraging results, given that the contribution of the quadrupole to the anisotropic correlation function is by construction strongly asymmetric. Indeed, although $\mathcal{L}_2(\mu)$ goes like μ^2, we are capable of recovering most of the lost signal (from $\sim 60\%$ to below 5% in terms of fractional deviation) using only the signal projected on the sky.

5.2 The VIPERS 2PCF

As shown in the previous section, angular selection effects can have a non-negligible bias on the recovered 2PCF amplitude, if not properly taken into account. Unfortunately, some of the corrections for angular selection biases do have an effect also on the redshift distribution. Figure 5.11 shows the effect of correcting for the TSR and SSR on the observed redshift distribution of the VIPERS data. While the TSR does not introduce a significant redshift dependence (being mostly a function of the projected density on the sky), the application of the SSR boosts the expected number of galaxies in the distant ($z > 1$) part of the sample. This clearly reflects the increased inefficiency to measure redshifts for more and more distant objects. To be fully consistent with the data, then, the random samples used for the clustering analyses will have to be weighted accordingly.

Once all the previous corrections have been implemented, we finally measure the two-point correlation function using the actual VIPERS dataset. Figure 5.12 shows the measurement of the anisotropic correlation function $\xi(r_p, \pi)$ obtained from the full VIPERS data at $0.5 < z < 0.7$ and $0.7 < z < 1.2$. These are ultimately the bins that we will use to obtain measurements of the growth rate (in this case, though, we will use the first two even multipoles rather than the full shape of $\xi(r_p, \pi)$). A bin size $\Delta s = 0.5\,h^{-1}\,\mathrm{Mpc}$ has been used in both r_p and π directions. We combine the results coming from the two VIPERS fields W1 and W4 simply by summing up the pair counts in each bin of separation and normalising for the total number of objects. This operation requires the random catalogues of the two field to be populated proportionally according to the actual number of galaxies among W1 and W4. As specified in the previous sections, we typically use random samples that are 30 times larger than the datasets. Plots are colour-coded according to the intensity of the clustering signal. Iso-contours are also displayed, so that the impact of RSD (large scale flattening + Fingers of God) on the clustering is made more visible.

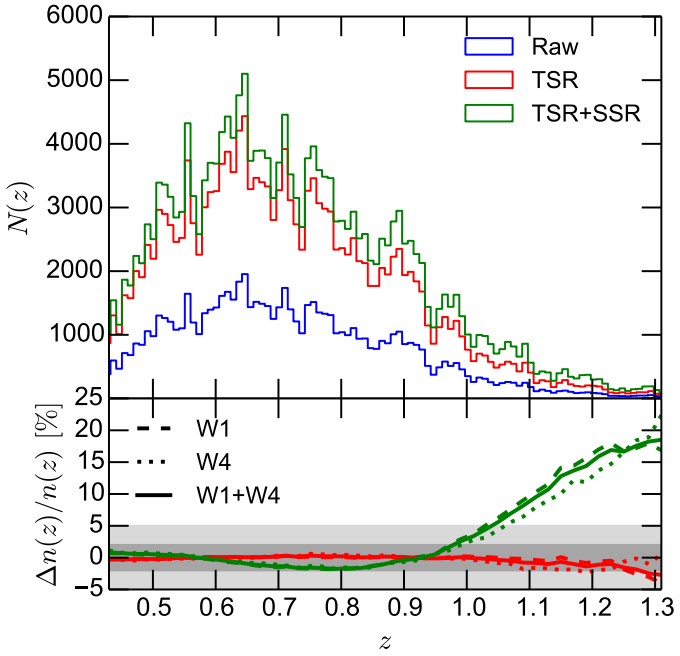

Figure 5.11: Impact of the Target Sampling Rate and the Spectroscopic Success Rate on the radial profile of the VIPERS galaxy samples. In the bottom panel we plot the relative difference of the $V_{\rm max}$ fits to the redshift distribution after applying the correction, to the same obtained from the observed histogram. Dashed, dotted and solid lines give the results for W1, W4 and the combined measurement, respectively. The smoothed radial profile is estimated using the $V_{\rm max}$ method. While the TSR does not affect the redshift distribution, the SSR enhances the number counts at $z > 0.95$.

As stated above, in the analysis presented here we shall analyse two redshift sub-samples of the whole survey (W1 + W4) in the ranges $0.5 < z < 0.7$ and $0.7 < z < 1.2$, including respectively 30 764 and 35 734 galaxies.

5.2.1 Covariance matrix and error estimation

The error estimation is performed directly on the multipoles of the two-point function, since we are not going to use directly the anisotropic 2PCF inside Figure 5.12, as already stated in the previous section.

Given the intrinsic correlation among different bins of the two-point correlation function (and consequently of its multipoles), we are forced to provide a reliable estimate of the covariance matrix to be used during the fitting procedure. This requires a further refinement of a more traditional error estimation based on the estimation of just the diagonal elements of the full

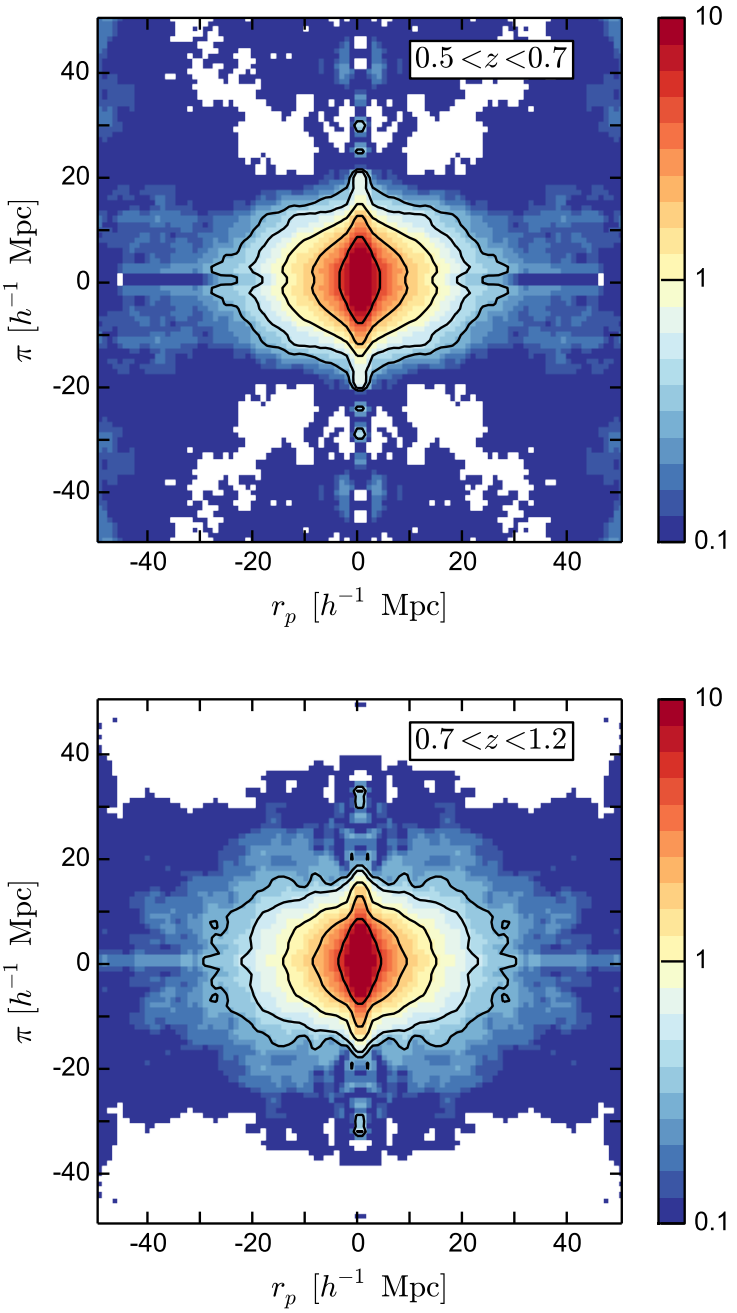

Figure 5.12: Final measurements of the anisotropic redshift-space correlation function, $\xi(r_p, \pi)$ from the final data of the VIPERS survey, within the two redshift ranges indicated by the labels. Solid contours correspond to iso-correlation levels of 0.3, 0.5, 1, 2, 5.

covariance matrix (corresponding to the intrinsic variance of the selected bins).

The classical definition of covariance between two stochastic events $\mathbf{X}$ and $\mathbf{Y}$ is

$$\mathrm{Cov}(\mathbf{X}, \mathbf{Y}) = \mathbf{E}\big((\mathbf{X} - \mathbf{E}(\mathbf{X}))(\mathbf{Y} - \mathbf{E}(\mathbf{Y}))\big), \tag{5.9}$$

where $\mathbf{E}(\mathbf{X})$ corresponds to the expected value of the variable $\mathbf{X}$. In our case, the covariance matrix C is organised in four blocks corresponding to the monopole-monopole, quadrupole-quadrupole and monopole-quadrupole cross covariance (two identical blocks in the latter case). The full monopole-quadrupole covariance matrix is estimated making use of the 153 mock realisations as

$$\hat{C}_{ij} = \frac{1}{N_s - 1} \sum_{k=1}^{N_s} \left(y_i^k - \bar{y}_i\right) \left(y_j^k - \bar{y}_j\right), \tag{5.10}$$

where $N_s = 153$ is the number of independent realisations used to estimate the covariance, y is the monopole-quadrupole vector, indices i, j run over the data points and index k runs over different realisations. The mean value $\bar{y}$ (corresponding to the expected value $\mathbf{E}$ in Equation 5.9) is estimated by averaging the measured values from different realisations, namely

$$\bar{y} = \frac{1}{N_s} \sum_{k=1}^{N_s} y^k. \tag{5.11}$$

Covariance matrices along with their correlation matrices $\hat{R}$ for the two redshift sub-samples are shown in Fig. 5.13. These matrices are obtained simply by renormalising $\hat{C}$ for its diagonal, namely

$$\hat{R}_{ij} = \frac{\hat{C}_{ij}}{\sqrt{\hat{C}_{ii}\hat{C}_{jj}}}. \tag{5.12}$$

The practical use of this normalisation is that in this way we have a transparent picture of how off-diagonal terms contribute to the one-point dispersion, that instead corresponds to the diagonal elements. We notice a strong auto-correlation among different s-bins (both for $\xi^{(0)}$ and $\xi^{(2)}$), but also a non-negligible cross correlation between the two multipoles, that can increase up to almost 40% of the diagonal amplitude. This clearly will impact the fitting procedure, both enlarging the derived constraints on the parameters and shifting the position of the best-fit measurements.

The error estimation will result an essential step during the fitting procedure. For that, we will require an inverse covariance that will replace the classical $(\sigma^2)^{-1}$ term in the χ^2 formalism. This topic will be treated with more focus during the next sections.

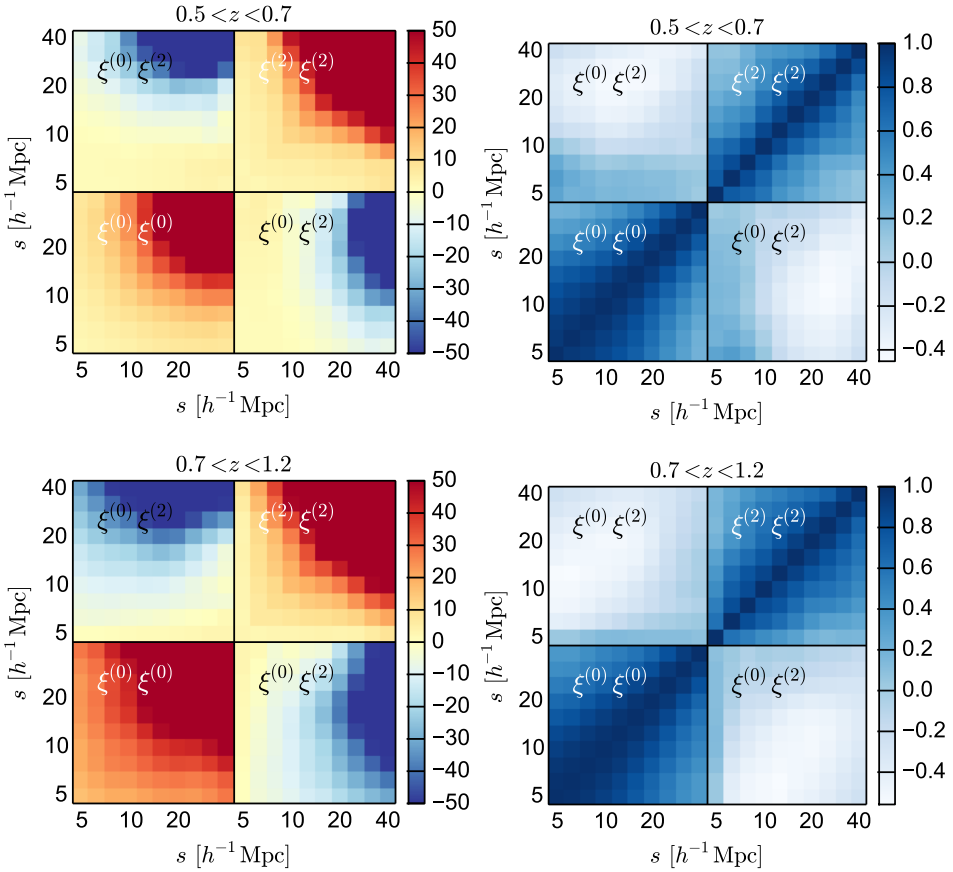

Figure 5.13: Correlation matrices for the combined monopole-quadrupole data vector, in the low (top) and high (bottom) redshift bin. Correlation matrices are computed as $R_{ij} = C_{ij}/\sqrt{C_{ii}C_{jj}}$, where C is the covariance matrix estimated from a set of 150 independent mock samples. The bottom left and top right squares correspond respectively to the auto-covariance of the monopole $s^2\xi^{(0)}$ and the quadrupole $s^2\xi^{(2)}$, while the remaining squares show the cross-covariance terms. The scales under consideration range from $s_{\mathrm{min}} = 5\,h^{-1}\mathrm{Mpc}$ to $s_{\mathrm{max}} = 50\,h^{-1}\mathrm{Mpc}$ (from left to right).

Chapter 6

GROWTH RATE MEASUREMENTS

In this section we combine all the informations collected in the previous chapters to create a model two-point correlation function capable of describing the clustering signal coming from the VIPERS dataset and from its mock catalogues. The latter are used as a reference testing ground in order to assess the impact of multiple systematic defects in the data processing and in the RSD modelling.

6.1 Fitting procedure

In all the introduced models, free parameters are identified by the tuple $(f, b, \sigma_{12}, \sigma_8)$, where f is the growth rate, b is the linear galaxy bias, $\sigma_{12} = \sigma_v$ is the nuisance parameter standing as a pairwise velocity dispersion inside non-linear structures, and σ_8 is the density rms fluctuations within spheres of 8 h^{-1}Mpc radius. Once the parameters are fixed and the RSD model is selected we can thus compute the corresponding model galaxy correlation function. The latter is used directly to compare with actual measurements and find the combination of parameters that minimises the difference between the two curves. In detail, the fit is carried out performing a maximum likelihood analysis of the data given the RSD model, that can be more easily described as the search throughout the parameter space of the position minimising the likelihood function $\mathcal{L}$ defined as

$$-2\ln\mathcal{L} = \sum_{i=0}^{N_b-1}\sum_{j=0}^{N_b-1}(y_i^d - y_i^m)\Psi_{ij}(y_j^d - y_j^m). \tag{6.1}$$

Here the observable $y = (\xi^0, \xi^2)$ is the monopole-quadrupole combined vector, $\Psi \equiv C^{-1}$ is the precision matrix (the inverse of the covariance matrix), N_b is the total number of data points, and indices d and m stand respectively for data and model.

The inversion of C is achieved using the singular value decomposition (SVD) method. The latter consists in a factorization of a given matrix as a product of two unitary matrices and one diagonal matrix containing the eigenvalues of the original matrix. In this way the inversion of C turns into the inversion of orthogonal and diagonal matrices, for which there safe prescriptions can be found in literature. Figure 6.1 shows the precision matrices of the two redshift bins, from an initial separation of $5\,h^{-1}$Mpc to a final one of $50\,h^{-1}$Mpc.

Given the large number of mock samples, the estimate and the inversion of the covariance matrices can be realised with good accuracy. However, the use of a finite number of mocks has two implications. Firstly, the estimated precision matrix obtained by taking the inverse of $\hat{C}$ is biased with respect to the true one, $\Psi = C^{-1}$, with the difference being well-represented by an inverse Wishart distribution. Furthermore, the precision matrix Ψ contains statistical errors that propagate to the parameter space, affecting the derived errors on the cosmological parameters. We follow Percival et al. (2014) and correct for these effects by applying two correction factors. In the first case, we can remove the systematic bias of the precision matrix by rescaling $\hat{C}^{-1}$ as

$$\Psi = \left(1 - \frac{N_b + 1}{N_s - 1}\right) \hat{C}^{-1}. \tag{6.2}$$

The latter correction factor involves the total number of data points N_b and realisations N_s. It takes into account the typical skewness characterising an inverse Wishart distribution and is capable of providing an unbiased estimate of the precision matrix (Hartlap et al. 2007). In the second case, the propagation of errors from the precision matrix to the derived parameters can be corrected by defining

$$A = \frac{2}{(N_s - N_b - 1)(N_s - N_b - 4)},$$

$$B = \frac{(N_s - N_b - 2)}{(N_s - N_b - 1)(N_s - N_b - 4)}, \tag{6.3}$$

and applying the correction factor

$$m_1 = \frac{1 + B(N_b - N_p)}{1 + A + B(N_p + 1)} \tag{6.4}$$

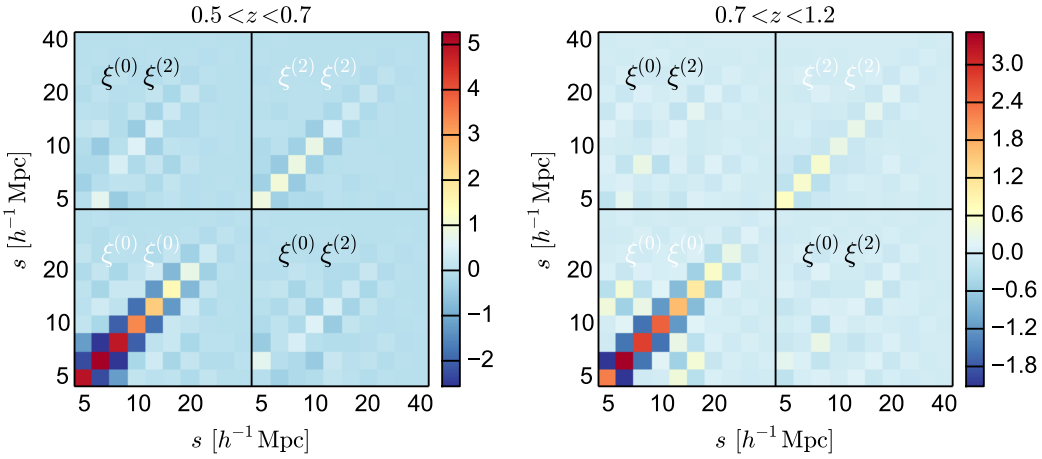

Figure 6.1: Precision matrices of the combined monopole+quadrupole observable, over the two redshift ranges $0.5 < z < 0.7$ and $0.7 < z < 1.2$. The inversion of C has been computationally achieved exploiting the SVD method.

to the estimated parameter covariance. In the previous equation, N_p is the total number of free parameters.

The fitting procedure is made much more robust than using a simple likelihood grid, by making use of a Markov Chain Monte Carlo (MCMC) approach. This is based on a likelihood-dependent sampling of the likelihood itself throughout the parameter space. Basically, at each iteration the code samples the likelihood at a position different from the current one, and moves to that position according to the measured likelihood (if the likelihood is larger, than the new position is more likely than the current one; on the contrary, the new position is accepted with a probability that is an exponential function of $\mathcal{L}$). In this way, we end up with a density map of the parameter space clearly showing where most of the occurrences are located. The best fitting values for each of the tested parameters are subsequently obtained by marginalising the multidimensional likelihood function over the remaining parameters. The output of the MCMC has been cross-checked with the independent MCMC code used in de la Torre et al. (2016), showing a percent agreement between the two different routines.

One of the most delicate aspects of the fit is the choice of priors for the full set of free parameters used in the modelling. We select flat priors using boundaries that allow a large set of late-time evolution cosmological models to be considered as possible alternatives to standard ΛCDM. Priors have been chosen flat so to prevent any tuning of the final measurement of the growth rate to a particular model. The full list of priors is shown in Table 6.1. After the MCMC has collected a sufficient number of points (iterations in the

Table 6.1: Adopted priors on the sampling parameters.

Parameters	Uniform prior
f	$[0.2, 1.8]$
σ_{12}	$[0, 8]$
b	$[0.5, 5]$
σ_8	$[0.2, 0.65]$

parameter space; the required number is based on how rapidly the MCMC converges to the minimum of the χ^2), chains are modified in order to obtain the derived parameters $f\sigma_8$ and $b\sigma_8$. Actually these are the combinations that are typically measured from galaxy surveys.

All the RSD models we test are constructed starting from Fourier space, and generating the real-power spectra (density and velocity) making use of CAMB and our fitting formulae. In detail, the linear matter power spectrum is generated fixing all the cosmological parameters to our fiducial cosmology (see Table 6.2). At each step in the MCMC the linear spectrum is renormalised by the current value of σ_8 and subsequently the non-linear spectra can be obtained as explained above. The first parameter to enter in the model is thus σ_8, that serves as a normalization of the linear power spectrum.

Then we build up the desired RSD model: first we construct the Kaiser term (that is different among the three RSD models), and secondly we multiply it by the selected damping factor. In this way the parameters f, b and σ_{12} are also employed in the construction of $P^s(k, \mu)$.

In the end, we measure the Fourier-space multipole moments as

$$P^{(\ell)}(k) = \frac{2\ell + 1}{2} \int_{-1}^{+1} P^s(k, \mu) \mathcal{L}_\ell(\mu) d\mu, \tag{6.5}$$

and convert them to their configuration space counterparts as

$$\xi^{(\ell)}(s) = i^\ell \int \frac{dk}{2\pi^2} k^2 P^{(\ell)}(k) j_\ell(ks), \tag{6.6}$$

where j_ℓ denotes the spherical Bessel functions.

Table 6.2: Cosmological parameters of the fiducial cosmology we select throughout our analysis.

Parameters	Uniform prior
Ω_m	0.30
Ω_b	0.045
Ω_Λ	0.70
h	0.7
n_s	0.96
σ_8	0.82

6.2 Systematic errors on the growth rate from the VIPERS mocks

We test in this section the RSD models introduced previously on our set of $N_s = 153$ mock catalogues. In practice, analysing each mock and averaging the measurements would be computationally infeasible, considering the large number of configurations to be tested. We thus chose to average the monopole and quadrupole measurements over the mocks, scale the covariance matrix properly, and fit the models to these average measurements. The aim is to reach a statistical uncertainty that is a factor $1/\sqrt{N_s}$ smaller than a single VIPERS survey, to be able to detect potential systematics as small as 1%. This process is more revealing and can show how well a given model performs in recovering the detailed shapes of the quadrupole and monopole correlation function.

We perform likelihood analyses of the mock mean measurements in different configurations, starting the ideal case and moving on to that in fully realistic conditions. We vary the minimum scale s_{min} of the fit to understand how to select the best fitting range for the VIPERS data – we expect all RSD models to fail at sufficiently small and non-linear scales. The maximum scale of the fit is fixed at $s_{max} = 50\,h^{-1}$Mpc, above which errors on the VIPERS measured monopole and quadrupole become too large.

6.2.1 Ideal case

We first study the ideal case that neglects the complex VIPERS angular selection by using the parent mocks. Here we consider mock measurements from the full redshift range probed by VIPERS, i.e. $0.5 < z < 1.2$, to avoid tuning the procedure towards small systematic deviations on the two red-

shift bins. The relative difference of the recovered $f\sigma_8$ with respect to the fiducial one is shown in the left panel of Figure 6.2. Redshift errors are not considered here to understand how different RSD models behave in the absence of any observational bias. Two types of small-scale damping factor $D(k\mu\sigma_{12})$ are tested: the Lorentzian (filled symbols) and Gaussian (dashed lines) forms. The overall trend of models using Lorentzian damping favours the TNS model: it yields almost unbiased measurements of the growth rate down to $s_{min} = 5\,h^{-1}\,\mathrm{Mpc}$. Some overestimation is however seen for minimum scales close to $s_{min} = 8\,h^{-1}\mathrm{Mpc}$, which in fact corresponds to the zero-crossing scale of the quadrupole $\xi^{(2)}(s)$. In this sense the raw output of the MCMC chains is self-explanatory: indeed, we notice that for those minimum separations that provide an overestimation of the combination $f\sigma_8$ the sampling parameter σ_8 is more likely to be selected outside of the corresponding prior (which is shown in Table 6.1). We consider this to be a manifestation of the high sensibility of the MCMC to the quadrupole zero-crossing. Actually, the marginalised best fit σ_8 falls well outside of the flat priors we have selected, in a region that is physically excluded by several other probes of the cosmological model.

In contrast with the Taruya model, both dispersion and Scoccimarro models consistently underestimate the growth rate with an error that fluctuates between 5–10%. Evidently, in all the cases the choice of a Lorentzian damping yields smaller systematic deviations than with a Gaussian damping. This is reflected by the trend of the dashed lines, which are close to the corresponding markers only when the minimum fitting separation s_{min} is larger than $\sim 15\ h^{-1}\mathrm{Mpc}$, while rapidly deteriorating when smaller separations are included in the fit. This is highlighted in the right panel of Figure 6.2, where the different best-fitting models for the monopole and quadrupole using $s_{\mathrm{min}} = 5\,h^{-1}\mathrm{Mpc}$ are directly compared to the mock data. Using a Gaussian damping, the model is no longer able to provide a good description of $\xi^{(0)}$ and $\xi^{(2)}$. Actually, the fit is mostly dominated by the small scales, whose data points have the smallest errors, and this explains why separations above $7\,h^{-1}\mathrm{Mpc}$ are apparently the ones giving the strongest deviation between model and data. This result is in close agreement with previous work on the subject (e.g Bianchi et al. 2012; de la Torre & Guzzo 2012), that showed how the choice of damping function has only a significant impact on the modelâĂŹs ability to handle small scales. Actually, the difference between the two damping terms diminishes with increasing s_{min}, given the similar asymptotic behaviour of the two functional forms.

It is important to note that for $s < 10\,h^{-1}\,\mathrm{Mpc}$, the accuracy with which the growth rate is recovered tends to deteriorate for all models (stable measurements of f are obtained only above this scale). This is plausibly associ-

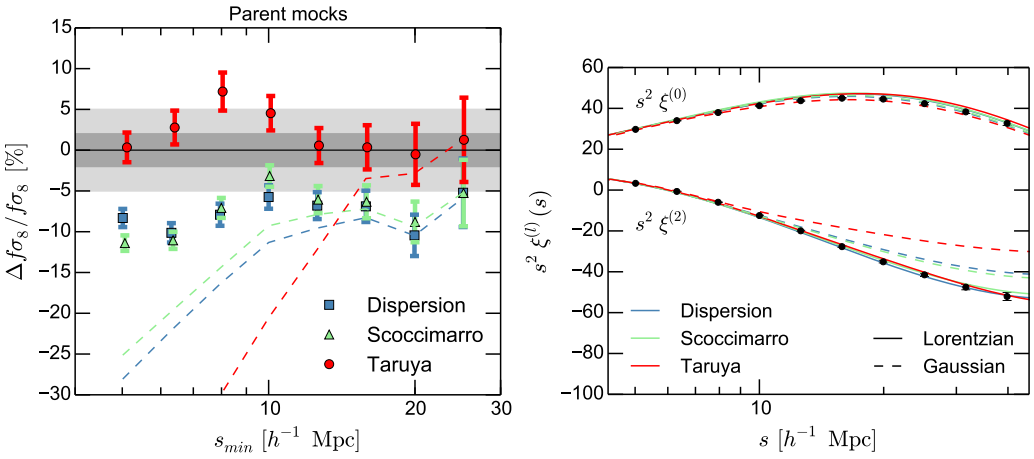

Figure 6.2: On the left: systematic errors on the measurement of the linear growth rate from the mean of 153 mock samples, using the three models discussed in the text. Here we used the parent mocks, to focus on the intrinsic performances of the models. Relative systematic errors are plotted as a function of the minimum fitting scale $s_{\rm min}$. $s_{\rm max}$ is always fixed at $50\,h^{-1}$Mpc. The filled symbols correspond to the use of a Lorentzian form for the non-linear damping factor in the models, whereas dashed lines to a Gaussian one. On the right: comparison between the best fit models for the monopole and quadrupole on the averaged parent mocks using different combinations of RSD models and damping factors. The fit uses down to $s_{\rm min} = 5\,h^{-1}$Mpc. The use of a Gaussian damping in the models clearly dramatically worsen the accuracy of the fit, in particular for the large-scale quadrupole signal.

ated with the increase of non-linearities in galaxy clustering. In this regime, the assumption of linear biasing breaks down and it becomes crucial to account for non-linearities to recover unbiased measurements of the growth rate. Nevertheless, given the expected statistical uncertainty of using one realisation only, we can push our analysis down to $5\,h^{-1}$ Mpc.

6.2.2 Case with redshift errors

So far no redshift error has been assumed in the mock samples. However, as already introduced at the end of Chapter 3, real VIPERS measurements have a non-negligible error, which clearly impact observed redshift-space distortions. We know from the multiple redshift measurements (Scodeggio et al. 2016) that the redshift error probability distribution for the VIPERS sample of reliable redshifts used here, is well described by a Gaussian with standard deviation $\sigma_z = 0.00054(1+z)$. This corresponds to a dispersion in galaxy peculiar velocity of $160\,{\rm km\,s^{-1}}$.

By applying random errors to mock galaxy redshifts following the VIPERS observed distribution, we can effectively see additional distortions. These are

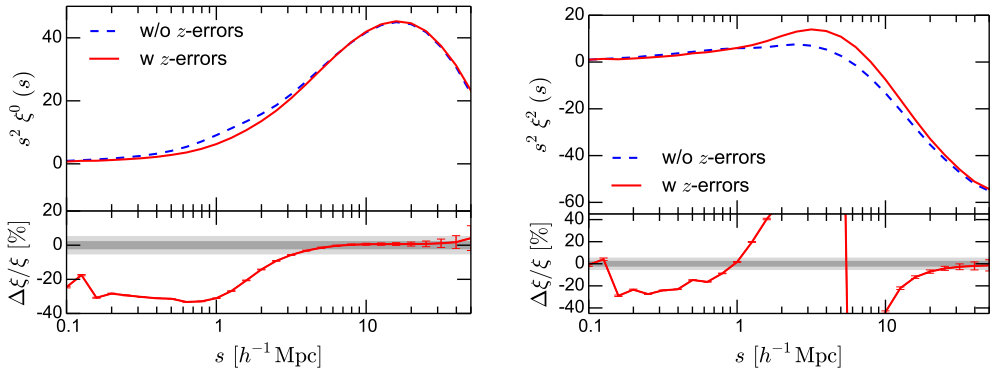

Figure 6.3: Effect of redshift errors on the recovered monopole and quadrupole from the galaxy mocks, obtained by adding to the mock redshifts a random Gaussian deviate with dispersion equal to the *rms* redshift error of the VIPERS.

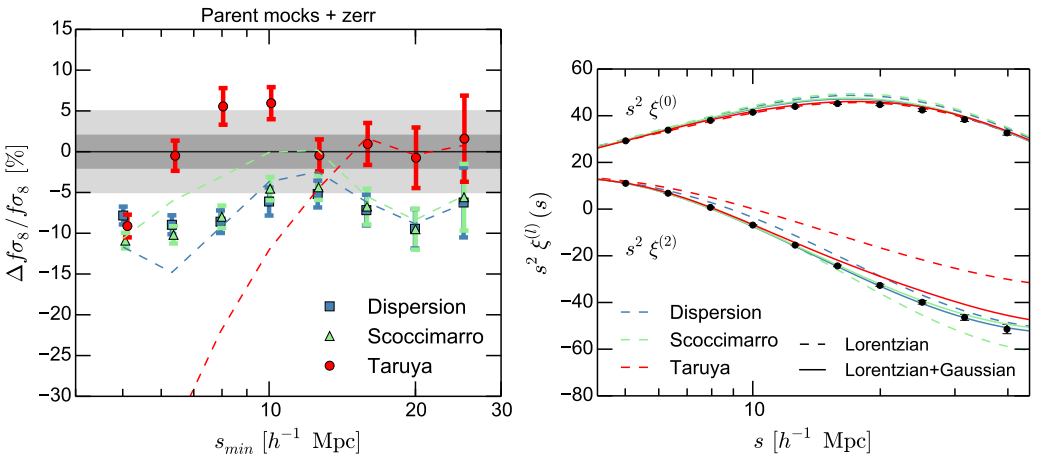

Figure 6.4: Same as Figure 6.2, but now including Gaussian redshift errors with dispersion equal to the *rms* value measured for the VIPERS data, added to the mock galaxy redshifts. Here the dashed lines correspond to the use of a Lorentzian damping only, which in Fig. 6.2 was found to perform at best. With redshift errors, this needs to be supplemented by a further Gaussian damping factor with dispersion fixed to the above *rms* error value, to yield the values described by the filled symbols.

shown in Fig. 6.3, where one can see how the shapes of the monopole $\xi^{(0)}(s)$ and the quadrupole $\xi^{(2)}(s)$ are affected. The imprint of redshift errors is similar to that of a small-scale damping of the power spectrum. While the monopole is damped below $4\,h^{-1}$Mpc, the quadrupole is corrupted over a range extending out to $\sim 20\,h^{-1}$Mpc. Clearly, this effect needs to be carefully handled or modelled, if one hopes to recover an unbiased value for the

growth rate. The consequences of not correcting for this effect are shown by the dashed lines in Figure 6.4, where we are repeating the tests of Figure 6.2, but now including redshift errors. As feared, there is a significant deviation from the values of $f\sigma_8$ previously measured with the models in the best configuration, i.e. with the Lorentzian damping.

Rather than correcting for redshift errors in the measurements, as performed for the angular selection selection, it is better to include it in the modelling. It is intuitive to supplement the models with a convolution by an extra Gaussian distribution with standard deviation fixed to the VIPERS *rms* value of $\sigma_z = 160$ km s^{-1}, which corresponds to

$$\sigma_\pi = \frac{c\sigma_z}{H(z)}, \tag{6.7}$$

in terms of line-of-sight comoving separation. The filled symbols in Figure 6.4 show how with this extra damping term we recover a performance similar to the more idealised case of Figure 6.2.

In this case, we notice that the Taruya model combined with a lorentzian-only damping (red dashed line in Figure 6.4) is the one performing the worst below a typical scale of $10\,h^{-1}$Mpc. As for the slight overestimation of $f\sigma_8$ at intermediate separations, we argue that the Taruya model, being also the most sophisticated among the models we test, is the one that can be affected by a non perfect description of non-linear scales the most. In any case, we can artificially remove most of the systematic deviation from the fiducial value, adopting an empirical damping as the one described above (lorentzian+gaussian), for which the TNS model provides almost unbiased measurements of $f\sigma_8$ down to very small scales.

We therefore adopt the TNS model with Lorentzian damping and Gaussian error damping, as our reference model for the final RSD analysis of the VIPERS data. However, we will also test for consistency the behaviour of the other two models on the actual data, to verify whether the trends seen in the mocks are confirmed.

6.2.3 Fully realistic case

We now turn to the case including fully realistic observing conditions. This means considering the target selection (masks, TSR, SSR, etc.) and limiting the samples to the same redshift ranges covered by the data and including redshift errors. The results that we obtain are shown in Figure 6.5. The trends of the systematic error as a function of s_{min} are less stable than in the previous case, although the general behaviour and relative performances

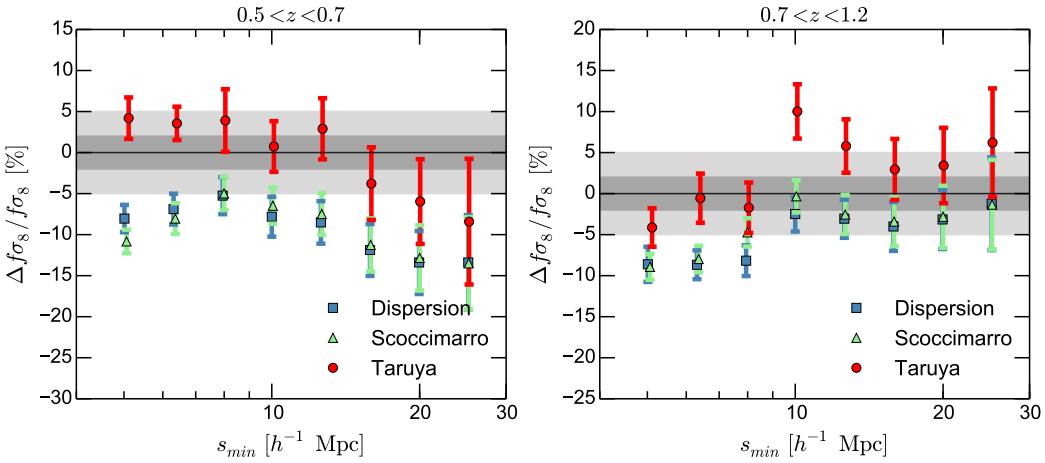

Figure 6.5: The same as Figure 6.4, but now using the fully realistic 'observed' mocks, on which all observational effects (masks, SPOC selection and redshift errors) have been included. As before, error bars correspond to the error on the average of the 153 samples. In this case, we show results independently for the two redshift ranges we probe, i.e. $0.5 < z < 0.7$ on the left and $0.7 < z < 1.2$ on the right.

of the models are the same. The variation gives us an idea of the impact of the selection function on samples this size.

Again, we see some instability in the TNS model (at least in the bin $0.7 < z < 1.2$) when the minimum scale of the fit is chosen around $s_{\rm min} \simeq 8\,h^{-1}$Mpc. When we look into the MCMC results in more detail, we see that in this case the Markov chain tends to drift towards unrealistic values of σ_8, which are outside of the prior range defined in Table 6.1. This seems to be related to the difficulty of TNS model to reach a stable fit in the region where the quadrupole crosses zero, something that has been already addressed in the previous sections. As soon as we include smaller scales (or we move away to larger ones), the regular trend is recovered. The recovery of similar trends using different mock samples is somewhat reassuring since this shows that we could expect similar trends also from the actual dataset. Nevertheless, we confirm the TNS model as the best performing one, with systematics $\lesssim 5\%$ down to the smallest probed minimum scales.

Overall, the different tests performed on the mock catalogues indicate that we can safely use the TNS model with the appropriate damping functions as well as a minimum fitting scale of $s_{\rm min} = 5\,h^{-1}$Mpc. This is the configuration that we adopt for the analysis of the VIPERS dataset. In the next chapter we will use the informations gathered in this chapter to directly obtain measurements of $f\sigma_8$ from the actual dataset. Clearly, statistical error will become definitely more important, as we will not consider any more the

averaged signal coming from a supermock with a volume ~ 150 times larger than the one of VIPERS.

6.3 RSD results from the VIPERS dataset

We present in this section the results of the RSD analysis of the VIPERS final dataset. We apply the methodology described in the previous sections to the VIPERS galaxy sample. In the likelihood analysis we impose rather broad uniform priors on the sampling parameters. These are reported in Table 6.1, and are selected to include a large fraction of possible alternatives to a ΛCDM. Since f and σ_8 are treated as separate parameters in the modelling, despite their intrinsic degeneracy, we need to impose sensible priors on them. In fact the most sensitive prior is that on σ_8, as it is the main parameter entering the non-linear modelling of RSD (non-linear spectra generated inside the MCMC are a strong function of σ_8). To define a sensible and realistic prior, while allowing room for deviations from GR, we base our choice on the Effective Field Theory of dark energy formalism (Gubitosi et al. 2013; Bloomfield et al. 2013; Gleyzes et al. 2013), which allows a description of various kinds of dark energy models and modifications of gravity to be expressed in a self-consistent framework that includes the growth rate of structure (Piazza et al. 2014; Perenon et al. 2015). The latter work shows that the range spanned by $\sigma_8(z)$ for stable theories can vary significantly, suggesting a range [0.2, 0.65] as appropriate to account for early- and late-time dark energy models at the redshifts covered by VIPERS (for definitions, see Perenon et al. (2016)). This excludes some more extreme modified gravity models, but avoids non-physical degeneracies that arise in the likelihood for some particular values of σ_8 outside of this range. This has been the case in the tests performed on the averaged mock sample (see the last chapter), where for a particular combination of RSD model and minimum fitting scale s_{min} the MCMC prefers extremely large values of σ_8.

The choice on the prior is corroborated by our parallel complementary analysis using the same data by de la Torre et al. (2016), in which the combination of RSD with galaxy-galaxy lensing constrains directly $\sigma_8(z)$, allowing a broader prior at the outset.

The $f\sigma_8$ measurements that we finally obtain using our standard configuraton and previously discussed parameter priors are $f\sigma_8(z = 0.60) = 0.55 \pm 0.12$ and $f\sigma_8(z = 0.86) = 0.40 \pm 0.11$. We consider these as our reference measurements in this work and discuss their cosmological implications in a short time. The measurements and best-fitting model monopole and quadrupole correlation functions obtained in the two considered red-

Table 6.3: Values of the growth rate and related parameters in the two redshift subsamples, obtained fitting the monopole and quadrupole correlation functions over the range $5\,h^{-1}$Mpc $<$ s $<$ $50\,\mathrm{h}^{-1}$Mpc, using the TNS model. Central values and 68% marginalized errors are reported, both on the sampling parameters f, b, σ_{12}, σ_8, and on derived parameters $f\sigma_8$ and $b\sigma_8$.

Parameters	$0.5 \leq z \leq 0.7$	$0.7 \leq z \leq 1.2$
Sampling parameters		
f	1.048 ± 0.199	0.742 ± 0.179
σ_{12}	4.996 ± 0.855	3.542 ± 0.784
b	1.423 ± 0.262	1.402 ± 0.234
σ_8	0.528 ± 0.076	0.539 ± 0.068
Derived parameters		
$f\sigma_8$	0.55 ± 0.12	0.40 ± 0.11
$b\sigma_8$	0.73 ± 0.03	0.74 ± 0.04

shift bins are shown in Figure 6.6. The corresponding best-fit values for the derived parameters are reported in Table 6.3.

It is interesting to verify a posteriori whether the trends and relative RSD model performances as a function of $s_{\min}$ established from the mock catalogues are similar to those seen in the real data. It is of course clear that any trend will be less significant, as the data are statistically equivalent to considering just one of the 153 mock catalogues. In the left panel of Figure 6.7, we show the result of this exercise, where the measured values of $f\sigma_8$ as a function of $s_{\min}$ are shown for the different tested models. To ease comparison, we have reported in the right panel and using the same scale, the corresponding results from the mock test for the realistic case (i.e. those of Figure 6.5). Apart from the different statistical errors, it is surprising to note how the three tested RSD models provide virtually identical results in the real data, as opposed to the behaviour seen in the mock catalogues. Moreover, it seems that in the data the variation of the $f\sigma_8$ measurements with minimum scale are not driven by the adequacy of the model down to those scales, but rather by statistical uncertainties in the measured galaxy correlation functions. The similarity in the results obtained from the different models is confirmed directly by the values of the reduced χ^2, which turn out to be very similar. By directly looking at the posterior likelihood distributions of the parameters obtained with the three models in Figure 6.8 (for both the low- and high-redshift bin), we can see that each model provides slightly different parameters degeneracies, although after marginalization, $f\sigma_8$ posterior likelihood distributions are almost identical

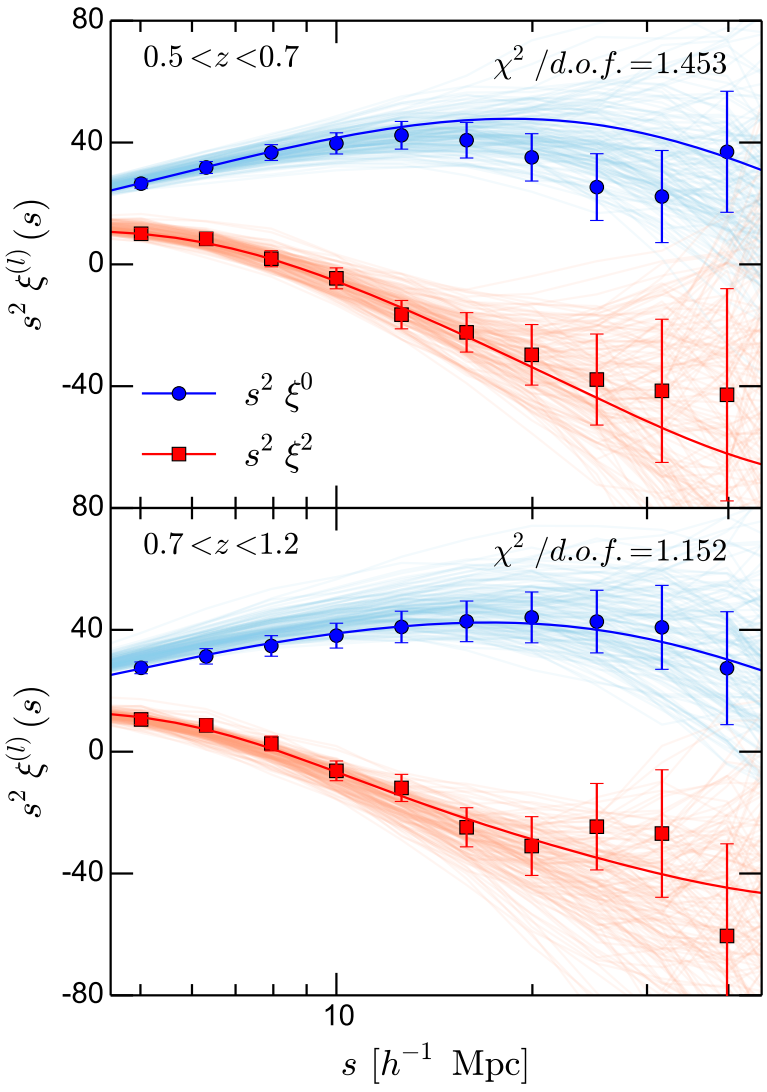

Figure 6.6: Monopole and quadrupole of $\xi(r_p, \pi)$ for the two redshift sub-sample of the final VIPERS dataset (solid points), together with the final best-fitting curves obtained using the TNS model, corresponding to the values reported in Table 6.3. The likelihood computation has used data down to $s_{\rm min} = 5\,h^{-1}$Mpc, as indicated by the tests. Error bars are $1-\sigma$ deviations, and correspond to the dispersion of the mock measurements. Each of these is also shown as a faint background line.

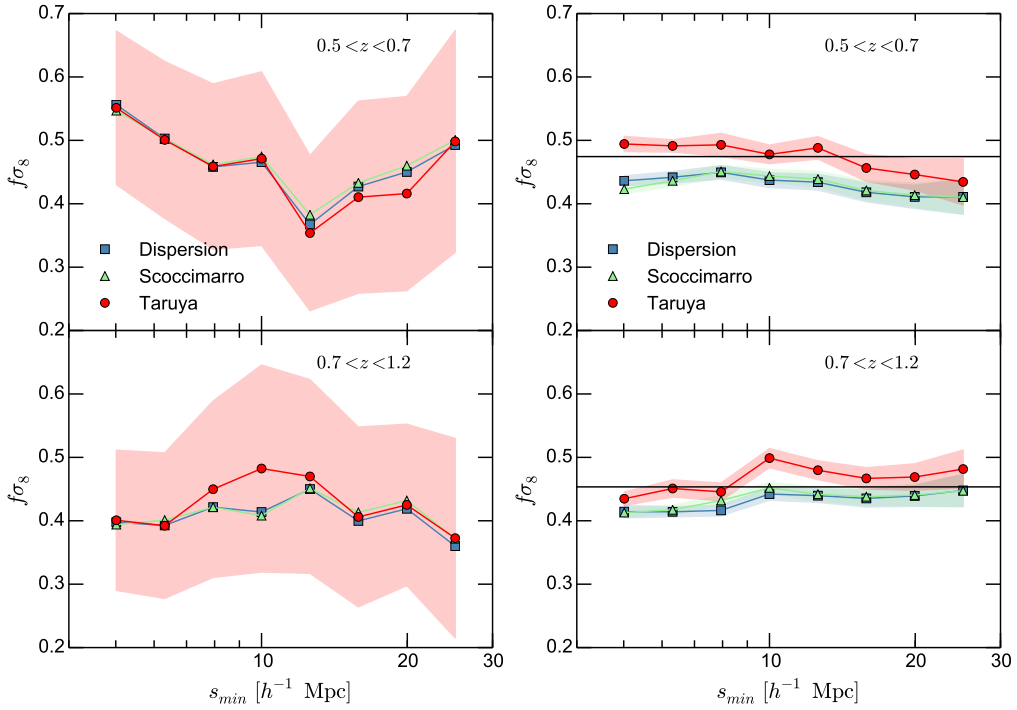

Figure 6.7: Left panels: the measured values of $f\sigma_8$ from the VIPERS survey in the two redshift bins, using the TNS model in its optimal set-up that we derived in Chapter 3 (double damping factor: free lorentzian + fixed gaussian), as a function of the minimum fitting scale $s_{\rm min}$. The maximum fitting scale $s_{\rm max}$ is always fixed at $50\,h^{-1}$Mpc. The shaded area gives the statistical error at each $s_{\rm min}$ for the TNS model, as derived from the mocks. Right panels: The same measurements performed on the average of the mocks, i.e. plotting the results of Figure 6.5 but showing explicitly the recovered values of $f\sigma_8$, to ease comparison to the data results on the left.

for the three RSD models, with only a slightly larger statistical uncertainty with the TNS model. However, some trends seen in the mock results are recognised in the data, as for example the preference of the TNS model in the high-redshift sample to deliver larger values of $f\sigma_8$ when $s_{\rm min}$ is close to the zero-crossing scale of the quadrupole.

Finally, it is important to emphasize the global non-linear approach to RSD that has been used in this analysis. We have used rather small non-linear scales in the fit, and by adopting a consistent modelling for the non-linearities in the real-space density and velocity divergence power spectra, we can obtain further cosmological insight. The level of non-linearity in our analysis is controlled by one single parameter, $\sigma_8(z)$, and we find that by letting this parameter vary, we can partly break the standard degeneracy that dominates on linear scales between f, σ_8, and b parameters. If we marginalise the posterior likelihood function over the σ_{12}, σ_8, b parameters, we obtain

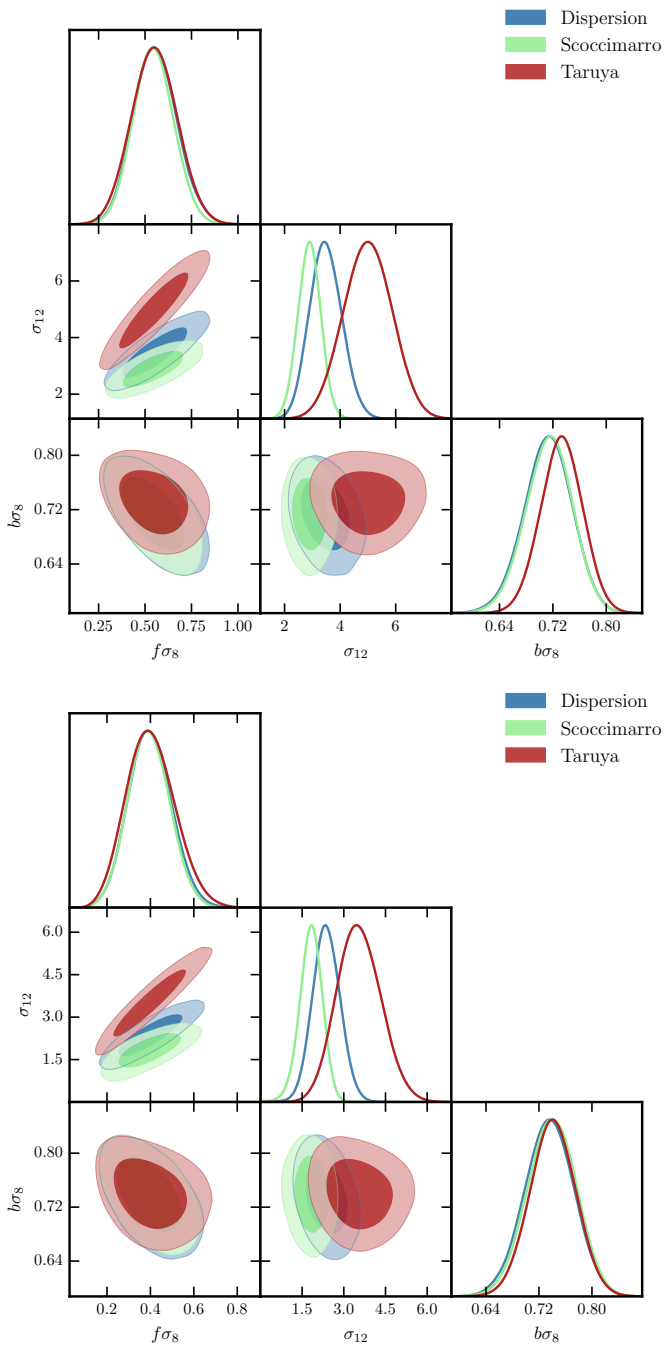

Figure 6.8: The one- and two-dimensional posterior likelihood distribution of the derived parameters $f\sigma_8$, $b\sigma_8$ and σ_{12} for the $0.5 < z < 0.7$ redshift bin. It corresponds to the result of the analysis of VIPERS data using dispersion, Scoccimarro, and Taruya model and $s_{\rm min} = 5\,h^{-1}$Mpc. The dark- and light-shaded areas correspond respectively to the 68% and 95% joint two-parameter confidence levels. The lower redshift sample shows comparable contours and shapes.

the following direct growth rate and σ_8 constraints: $[f(z = 0.6), \sigma_8(z = 0.6)] = [1.048 \pm 0.199, 0.528 \pm 0.076]$ and $[f(z = 0.86), \sigma_8(z = 0.86)] = [0.742 \pm 0.179, 0.539 \pm 0.068]$. A similar approach has been adopted in de la Torre et al. (2016), where this is strengthened by additional constraints from galaxy-galaxy lensing. In particular, the latter allows improving σ_8 constraints while keeping similar uncertainties on f. A detailed discussion of these results is given in de la Torre et al. (2016). Here, in Figure 6.9 we show one of the most immediate results obtained in that paper, that is, the strong degeneracy between f and σ_8, and its removal when galaxy-galaxy lensing is included in the analysis. In this case, as already stated, we notice a definitely better constraint on σ_8, and a basically unaltered constraint on the growth rate. Nevertheless, the cross-correlation between two different cosmological observables (RSD and g-g lensing in this case) is a valuable tool that will acquire more and more statistical power as soon as large galaxy dataset are obtained. Overall, these findings demonstrate the additional constraining power encapsulated in quasi-linear scales, which can be used to break degeneracies and further improve the precision of measurement of the growth rate of structure.

The measured values of the growth rate are confronted in Figure 6.10 with different measurements, including results from other surveys, the VIPERS earlier PDR-1 dataset, and parallel works analysing with complementary techniques analogous subsets of the VIPERS PDR-2 dataset. It may look surprising that there is no appreciable improvement in the error bars between the former measurement from the PDR-1 (red circles, de la Torre et al. (2013)) and the new PDR-2 estimate in a comparable redshift bin, despite a $\sim 30\%$ increase in the sample size. As discussed in de la Torre & Guzzo (2012), this is essentially a price to pay for the more sophisticated treatment of nonlinear effects through the TNS model, which increases the degrees of freedom.

A potentially significant fraction of systematics can be produced by the assumption of having a fixed redshift-distance relation, i.e. having fixed the cosmological parameter. Indeed, a wrong cosmological model would imply a measured real-space correlation function not perfectly isotropic. These geometrical distortions would finally sum up with redshift-space distortions causing a systematic error on the measured growth rate. The Alcock-Paczynski effect can be accounted for by adding two free parameters during the fit, that can be considered as scaling factors for the directions along and orthogonal to the line of sight. In this work, the AP effect has not been corrected for, given that adding two more degrees of freedom would have significantly enlarged errorbars on the recovered parameters. Nevertheless, we rely on a test performed in de la Torre et al. (2013), where two different fiducial cosmologies

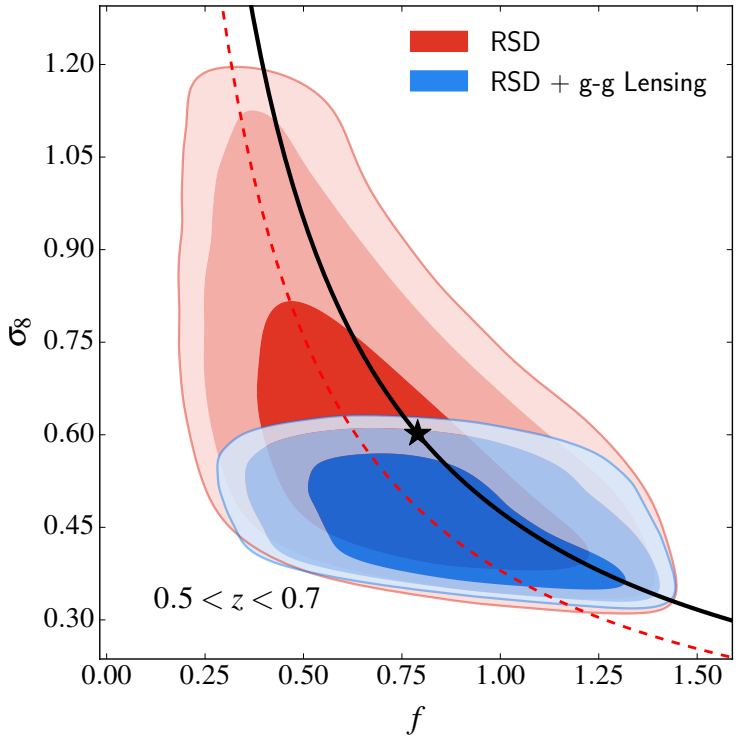

Figure 6.9: Two-dimensional marginalized posterior likelihood contours for f and σ_8 at $0.5 < z < 0.7$ as obtained in de la Torre et al. (2016). The plot shows the impact of the additional galaxy-galaxy lensing constraint on the $f - \sigma_8$ degeneracy. The black curve shows the region of constant $f\sigma_8$ associated with Planck Collaboration et al. (2015) ΛCDM + GR best-fit, while the combined (f, σ_8) constraint is marked with the star.

(i.e. a WMAP- and a Planck13-like cosmology) have been tested showing no significant deviation on the fitted growth rate (0.2% difference switching from one cosmology to the other one).

The parallel PDR-2 results include measurements obtained from the combination of RSD with galaxy-galaxy lensing (de la Torre et al. 2016) or using the void-galaxy cross-correlation (Hawken et al. 2016). In forthcoming papers, we shall additionally present further pieces of this combined approach, using specific colour-selected subsamples (Mohammad et al. 2017) or the linearised density field in Fourier space (Wilson et al. 2017), to minimise the need for non-linear corrections. All these papers represent complementary approaches towards understanding the current limitations we face in our ability to extract in practice the value of these parameters from the modelling of RSD.

The values measured by these different techniques on the same VIPERS data as well as from other surveys at similar redshifts are virtually all com-

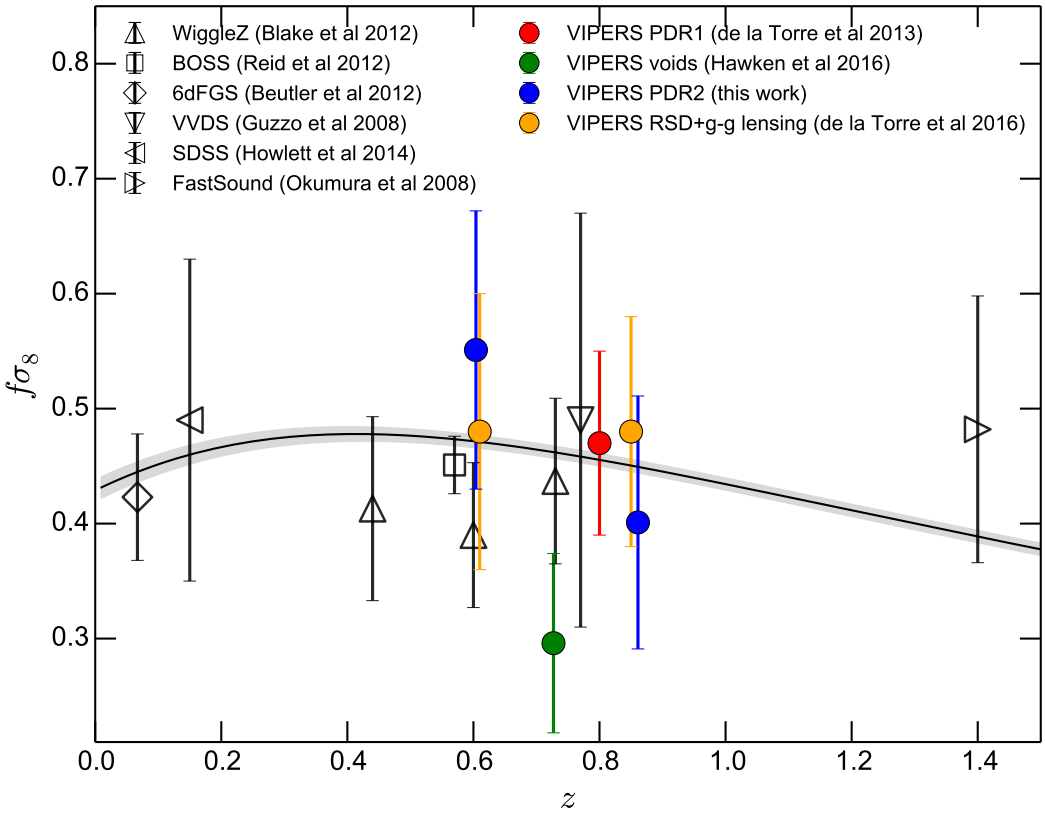

Figure 6.10: Plot of $f\sigma_8$ versus redshift, showing the VIPERS results together with a compilation of recent measurements. The previous results from 2dFGRS (Hawkins et al. 2003), 2SLAQ (Ross et al. 2007), VVDS (Guzzo et al. 2008), SDSS LRG (Cabré & Gaztañaga 2009; Samushia et al. 2012), WiggleZ (Blake et al. 2011), BOSS (Reid et al. 2012), and 6dFGS (Beutler et al. 2012) surveys are shown with the different symbols (see inset). The solid curve and associated error correspond to the prediction for General Relativity in a ΛCDM model set to Planck 2015 cosmological parameters (Planck Collaboration et al. 2015).

patible within 1-σ and agree with the predictions of a ΛCDM model governed by Einstein gravity. But on a larger sample, with much smaller statistical errors, greater care would be needed to test for possible systematic biases that might still be hidden in one or more of the analyses. The application of such a variety of approaches to VIPERS has been made possible by the specific properties of the survey, in particular its dense sampling and rich content of information. With a sparse sampled survey, which is the approach of most of the cosmologically-oriented surveys, it would have been impossible to characterise accurately the density field and apply the clipping linearisation technique of Wilson et al. (2017), or reliably detect cosmic voids such as those used in Hawken et al. (2016). At the same time, a survey with limited imag-

ing information would not permit investigation of the selection of optimal sub-populations (or the combination of different ones), as we are pursuing in Mohammad et al. (2017), or exploit the combination of RSD with lensing, as we have done in de la Torre et al. (2016) and which should be exploited to the fullest by Euclid mission (Laureijs et al. 2011) in the next decade. We therefore believe that the detailed investigation of the properties of RSD within VIPERS should serve as a valuable foundation for next-generation studies of greater statistical power.

Chapter 7

CONCLUSIONS

In this work I have performed a redshift-space distortions analysis exploiting the full statistical power of the VIPERS final dataset. The latter corresponds to the second Public Data Release (PDR-2), that has become available to public use in November 2016. Given the outstanding radial extension achieved by the survey, we have decided to split the full dataset in two redshift bin, i.e. $0.5 < z < 0.7$ ($z_{eff} = 0.60$) and $0.7 < z < 1.2$ ($z_{eff} = 0.86$). Globally, the two data samples contain 30764 and 35734 good-quality redshifts, respectively.

We have measured the anisotropic two-point clustering measuring the first two multipoles of the galaxy correlation function. To do that, we have constructed random samples 30 times larger than the actual datasets featuring the same selection function of the survey. Although most of precedent works on RSD used directly the anisotropic two-point function to obtain constraints on the growth of structures, it has become common practice to work with its multipoles, mostly to avoid the size of covariance matrices (not largely employed in the previously cited works) to explode. We performed tests to understand the impact of using a full covariance matrix rather than just its diagonal. The main discrepancy is clearly the different uncertainty on estimated parameters, but we also find out a non-negligible systematic on the central value.

Unfortunately, a significant fraction of the systematic bias introduced during the selection of targets (that is mostly density-dependent) cannot be corrected directly applying the same selection on the random catalogue. In order to account to the inhomogeneous sampling of targets (which is responsible for an almost constant suppression of the two-halo term of the two-point function) across a VIPERS quadrant we have developed a proper pipeline: each galaxy is upweighted by a local quantity, called Target Sampling Rate (TSR), that is obtained as the ratio between the local projected density field

of the observed sample and the one of the photometric sample (i.e. all candidate targets satisfying the survey selection criteria).

At the same time, the strong limitation of having a fixed physical size under which two galaxies cannot be targeted simultaneously turns into a strong damping of the two-point function, and in particular of the one-halo term. In this case, the TSR correction is not capable of perfectly recovering the amplitude of the two-point function. We have adopted the correction described in de la Torre et al 2013, based on the pair upweighting by the ratio between the angular correlation functions (once again, of the observed and photometric samples).

This approach, together with the TSR upweighting can recover the amplitude of both monopole and quadrupole within few percents from the fiducial value down within the Mpc scale. This result is outstanding, in particular if we consider the good quality of the quadrupole correction; indeed, we are capable of recovering its amplitude with systematics $< 5\%$ within the Mpc scale using only a partial information that comes from the projected density field. In this sense, if the almost perfect correction of the monopole is somewhat pushed by our correcting scheme, the same for the quadrupole is not guaranteed.

The inhomogeneous quality of redshift measurements is accounted with an additional weight, called Spectroscopic Success Rate (SSR), that is applied to the galaxy sample similarly to what is done with the TSR. This is a strong function of both magnitude and redshift, and thus it has a non-negligible impact on the recovered redshift distribution. This effect is easily taken into account by constructing a random sample that features the SSR-weighted redshift distribution, rather than the raw one.

In the end, I have obtained an almost unbiased measurement of monopole and quadrupole over the separation range that we use during the RSD analysis. The correction of residuals systematic biases in the measurement of the two-point function is essential if one wishes to provide robust results on the growth of structures. Indeed, next-generation redshift surveys will target hundreds of millions galaxies, reducing statistical fluctuations below the percent level, and this clearly will make the good estimate of the clustering signal a leading topic in cosmological measurements. The potential of our correcting scheme can also be exploited by different surveys, since its only requirement is a photometric redshift catalogue whence spectroscopic sources are selected.

Making use of reliable VIPERS-like mock catalogues, we have tested the efficiency of several RSD models that can be found in literature and that are still largely employed in many parallel RSD analysis. In detail, we have investigated the goodness of the dispersion model, the Scoccimarro model

and the Taruya model in the recovery of the growth rate. The latter so far can be considered as one of the best description of RSD down to the mildly non-linear regime, but its reliability has been checked directly over our simulated catalogues.

To do that, I have adapted a pre-existing MCMC pipeline (written in C) by writing a proper RSD likelihood. Our strategy consists in the derivation of a RSD model in Fourier space (where the observable is the power spectrum), and subsequently in the conversion of the $P(k)$ multipoles in their counterparts in configuration space. The latter are directly compared to the measured $\xi^{(0)}$ and $\xi^{(2)}$ to obtain constraints on the growth rate. This choice, of deriving the model in Fourier space, is related to the definitely simpler implementation of any of the RSD model we test. As a matter of fact, the application of a damping factor in front of the Kaiser term is just a multiplication in Fourier space, while it becomes a convolution (involving thus an integral) in configuration space.

My RSD likelihood has required the inclusion of an external routine capable of computing the non-linear matter power spectrum using HALOFIT prescriptions. This empirical approach is motivated by the necessity of having a good description of the non-linear spectrum up to $k_{max} \sim 1\,h\,\mathrm{Mpc}^{-1}$. Indeed, given the particularly fuzzy geometry of VIPERS, that targets galaxies over an outstanding radial rage at the expense of the angular surface, large scales cannot be probed with sufficient precision. This implies a strong effort in properly model mildly and strong non-linear scales, where most of the VIPERS clustering signal is enclosed.

For the same reason, we have developed accurate fitting functions for the velocity power spectra, that are required in the construction of the Scoccimarro and Taruya models. These functions can describe the velocity power spectra (auto- and cross-) up to $k_{max} \sim 0.8\,h\,\mathrm{Mpc}^{-1}$ with an accuracy of few percents requiring only two free parameters, and are thus much more fit to be used to model the underlying VIPERS velocity spectra. In addition, our fitting formulae are cosmology independent and can thus be adapted to the VIPERS dataset without tuning the growth rate measurements towards a preferred cosmology. At the same time, their universality makes such functions really fit to be used in other contexts, as in other RSD analysis on different galaxy samples. Given the importance of this topic, such functions, along with a comparison with PT predictions and pre-existing fitting templates, will be properly presented in an individual paper (Bel, Pezzotta et al., in preparation)

We have developed a complete C++ code capable of computing the additional Taruya terms to the redshift-space power spectrum for a given cosmology. The code has been cross-checked with an independent pipeline de-

veloped by Dr. Sylvain de la Torre and with the Taruya public code, showing a percent agreement on each correcting factor.

Tests on systematic defects of the recovered growth rate from its fiducial value are performed to understand the impact of different RSD models on the final measurement. This topic is similar to what has been already addressed during the estimation of the 2PCF. Indeed, any RSD models is obtained under precise assumptions. Each of these ansatz can lead to a systematic bias between the measured growth rate and underlying value. Thus, it becomes essential to check the amplitude of this bias using mock samples, for which we know a priori the input growth rate.

From the mocks, we confirm how the Taruya model is the one providing the most unbiased result, once compared with the dispersion and the Scoccimarro model. In all three cases, though, the values of $f\sigma_8$ progressively become more unstable as soon as smaller separations are included into the fit. This result is confirmed by previous works on the same subject. This is a direct evidence of how non-linear effects and their approximated description impacts any clustering measurement inside the non-linear regime. We notice a non-negligible degeneracy between σ_8 and the combination $f\sigma_8$ when the minimum fitting scale falls close to the scale where the quadrupole changes sign. The latter is particularly significant for the Taruya model, that is the one possessing the largest number of degrees of freedom. The degeneracy is the result of having let free the amplitude of the linear power spectrum (σ_8) inside the MCMC. This is necessary in the implementation of the Taruya model, since the latter cannot be parametrised only in terms of the derived parameter $f\sigma_8$. Nevertheless, our approach (which is similarly employed when implementing the dispersion and the Scoccimarro model) allows for more degrees of freedom, and thus, does not tune our measurements to the particular case where the amplitude of the spectrum is fixed to the one of a Planck-like ΛCDM.

We test two different damping factor (i.e. lorentzian and gaussian) in order to empirically account for the non-linear damping introduced by RSD at small separations. In the case where redshift errors are not considered, we find a lorentzian damping to reproduce much more faithfully the trend observed in the mocks. This result is confirmed by the analysis produced in de la Torre & Guzzo 2012. Though, as soon as errors are included in the analysis, neither of them provide sufficiently accurate measurements. We propose a mixed damping term where the gaussian factor is fixed to the redshift dispersion observed in the VIPERS data. In this way, the lorentzian component constrains the effect of RSD, while the gaussian one takes into account the additional damping generated by the uncertainty on measured redshifts. With this approach we are able to recover much more faithfully

the shape of the two-point function than with a single damping factor. This topic will be particularly significant for the scientific analysis of the Euclid survey, where current forecast on redshift errors are significantly larger than VIPERS's.

Using our final scheme, we are capable to recover an almost unbiased measurement of $f\sigma_8$ down to $5\,h^{-1}\,\mathrm{Mpc}$, which is the minimum fitting scale that we select for the data analysis. The maximum scale is fixed to $s_{max} = 50\,h^{-1}\,\mathrm{Mpc}$.

We repeat the previous tests on the VIPERS dataset, and surprisingly we notice a strong coherence of the three models, that provide almost equivalent results over the different minimum scales tested in this work. Although statistical fluctuations could in part be responsible for this trend, we speculate that the particular fitting procedure adopted in this work can have a non-negligible impact on the recovered $f\sigma_8 - s_{min}$ dependency that we observe in the actual data. Indeed, the implementation of both the dispersion and the Scoccimarro model have been realised assuming a fourth degree of freedom, in addition to the classical parameter set (f, b, σ_{12}), that is the amplitude of the matter power spectrum σ_8. If the Taruya model requires the four parameters to be fitted separately, the same is not valid for the two previous models, that could be easily parametrised in terms of $(f\sigma_8, b\sigma_8, \sigma_{12})$. We argue that the apparent coherence among the output of the three models is partially related to the implementation we have performed. Also, when looking to the two-dimensional posterior distributions of the parameters, we notice how best fits from different models are actually separated. The strong coherence of the results is an effect of having derived marginalised constraints on the $f\sigma_8$ parameter.

We obtain consistent values of the growth rate, $f\sigma_8 = 0.55 \pm 0.12$ and 0.40 ± 0.11 at effective redshifts of $z = 0.60$ and $z = 0.86$ respectively. Independent measurements of the same quantity exploiting different cosmological probes (see the companion papers of the VIPERS collaboration) all provide a coherent value of $f\sigma_8$, with a deviation that is less than 1-σ from the value obtained in this work. All these results are in agreement with standard cosmology predictions assuming Einstein gravity in a ΛCDM background. At the same time, they do not exclude a variety of cosmological models assuming the modification of gravity on cosmic scales. Results on the growth rate are reported in a paper that is currently submitted to *A&A*. The paper can now be found on arXiv as Pezzotta et al. 2016 (arXiv:1612.05645).

As already mentioned, the full potential of RSD in constraining the underlying cosmological model will be achievable only with next-generation galaxy surveys, that will collect redshift catalogues one order of magnitude larger than current ones. In this context, my work assumes a twofold relevance.

Indeed, this work not only stands as a leading project of the VIPERS collaboration, but also provides important hints for the scientific analysis that will be produced in the next decade.

Bibliography

Abazajian, K. N., Adelman-McCarthy, J. K., Agüeros, M. A., et al. 2009, , 182, 543

Alpher, R. A. & Herman, R. 1988, Physics Today, 41, 24

Anderson, L., Aubourg, E., Bailey, S., et al. 2012, , 427, 3435

Bernardeau, F., Colombi, S., Gaztañaga, E., & Scoccimarro, R. 2002, , 367, 1

Beutler, F., Blake, C., Colless, M., et al. 2012, , 423, 3430

Bianchi, D., Chiesa, M., & Guzzo, L. 2015a, , 446, 75

Bianchi, D., Gil-Marín, H., Ruggeri, R., & Percival, W. J. 2015b, , 453, L11

Bianchi, D., Guzzo, L., Branchini, E., et al. 2012, ArXiv e-prints

Blake, C., Brough, S., Colless, M., et al. 2011, , 415, 2876

Blake, C., Brough, S., Colless, M., et al. 2010, , 406, 803

Blake, C., Collister, A., & Lahav, O. 2008, , 385, 1257

Bloomfield, J. K., Flanagan, É. É., Park, M., & Watson, S. 2013, JCAP, 1308, 010

Bondi, H. & Gold, T. 1948, , 108, 252

Cabré, A. & Gaztañaga, E. 2009, , 393, 1183

Carbone, C., Petkova, M., & Dolag, K. 2016, , 7, 034

Carlson, J., White, M., & Padmanabhan, N. 2009, , 80, 043531

Carroll, S. M., Duvvuri, V., Trodden, M., & Turner, M. S. 2004, , 70, 043528

Castorina, E., Carbone, C., Bel, J., Sefusatti, E., & Dolag, K. 2015, , 7, 043

Chan, K. C., Scoccimarro, R., & Sheth, R. K. 2012, , 85, 083509

Clifton, T. 2011, Progress in Particle and Nuclear Physics, 66, 181

Colless, M., Dalton, G., Maddox, S., et al. 2001, , 328, 1039

Colless, M., Peterson, B. A., Jackson, C., et al. 2003, ArXiv Astrophysics e-prints

Coupon, J., Ilbert, O., Kilbinger, M., et al. 2009, , 500, 981

Crocce, M. & Scoccimarro, R. 2006, , 73, 063519

Davis, M. & Peebles, P. J. E. 1983, , 267, 465

de la Torre, S. & Guzzo, L. 2012, , 427, 327

de la Torre, S., Guzzo, L., Peacock, J. A., et al. 2013, , 557, A54

de la Torre, S. et al. 2016, submitted

Desjacques, V., Jeong, D., & Schmidt, F. 2016, ArXiv e-prints

Dvali, G., Gabadadze, G., & Porrati, M. 2000, Physics Letters B, 485, 208

Efron, B. 1982, The Jackknife, the Bootstrap and other resampling plans

Efstathiou, G., Sutherland, W. J., & Maddox, S. J. 1990, , 348, 705

Eisenstein, D. J. & Hu, W. 1998, , 496, 605

Fisher, K. B. 1995, , 448, 494

Friedmann, A. 1922, Zeitschrift fur Physik, 10, 377

Friedmann, A. 1924, Zeitschrift fur Physik, 21, 326

Garilli, B., Guzzo, L., Scodeggio, M., et al. 2014, , 562, A23

Garilli, B., Le Fèvre, O., Guzzo, L., et al. 2008, , 486, 683

Gil-Marín, H., Wagner, C., Verde, L., Porciani, C., & Jimenez, R. 2012, , 11, 029

Gleyzes, J., Langlois, D., Piazza, F., & Vernizzi, F. 2013, JCAP, 1308, 025

Gubitosi, G., Piazza, F., & Vernizzi, F. 2013, JCAP, 1302, 032, [JCAP1302,032(2013)]

Guo, H., Zheng, Z., Zehavi, I., et al. 2014, , 441, 2398

Guzzo, L., Pierleoni, M., Meneux, B., et al. 2008, , 451, 541

Guzzo, L., Scodeggio, M., Garilli, B., et al. 2014, , 566, A108

Hahn, O., Angulo, R. E., & Abel, T. 2015, , 454, 3920

Haines, C. P., Iovino, A., Krywult, J., et al. 2016, ArXiv e-print 1611.07050

Hamilton, A. J. S. 1992, , 385, L5

Harrison, E. R. 1974, , 191, L51

Hartlap, J., Simon, P., & Schneider, P. 2007, , 464, 399

Hawken, A. J., Granett, B. R., Iovino, A., et al. 2016, ArXiv e-print 1611.07046

Hawkins, E., Maddox, S., Cole, S., et al. 2003, , 346, 78

Heitmann, K., Higdon, D., White, M., et al. 2009, , 705, 156

Hinshaw, G., Larson, D., Komatsu, E., et al. 2012, accepted, ArXiv e-print 1212.5226

Hogg, D. W. 1999, ArXiv Astrophysics e-prints

Hoyle, F. 1948, , 108, 372

Hubble, E. 1929, Proceedings of the National Academy of Science, 15, 168

Hubble, E. 1937, , 97, 506

Hubble, E. P. 1936, Yale University Press

Ilbert, O., Arnouts, S., McCracken, H. J., et al. 2006, , 457, 841

Jackson, J. C. 1972, , 156, 1P

Jain, B. & Khoury, J. 2010, Annals of Physics, 325, 1479

Jennings, E. 2012, , 427, L25

Jennings, E., Baugh, C. M., Angulo, R. E., & Pascoli, S. 2010, , 401, 2181

Jennings, E., Baugh, C. M., & Pascoli, S. 2011, , 410, 2081

Kaiser, N. 1984, , 284, L9

Kaiser, N. 1987, , 227, 1

Kerscher, M., Szapudi, I., & Szalay, A. S. 2000, , 535, L13

Lahav, O., Lilje, P. B., Primack, J. R., & Rees, M. J. 1991, , 251, 128

Laureijs, R., Amiaux, J., Arduini, S., et al. 2011, ArXiv e-print 1110.3193

Le Fèvre, O., Saisse, M., Mancini, D., et al. 2003, in , ed. M. Iye & A. F. M. Moorwood, Vol. 4841, 1670–1681

Le Fèvre, O., Vettolani, G., Paltani, S., et al. 2004, , 428, 1043

Lewis, A., Challinor, A., & Lasenby, A. 2000, , 538, 473

Liddle, A. R. 1999, in High Energy Physics and Cosmology, 1998 Summer School, ed. A. Masiero, G. Senjanovic, & A. Smirnov, 260

Lilje, P. B. & Efstathiou, G. 1988, , 231, 635

Lilly, S. J., Le Brun, V., Maier, C., et al. 2009, , 184, 218

Linder, E. V. & Cahn, R. N. 2007, Astroparticle Physics, 28, 481

Longair, M. S. 2008, Galaxy Formation

Matsubara, T. 2008, , 77, 063530

Mo, H., van den Bosch, F. C., & White, S. 2010, Galaxy Formation and Evolution

Mo, H. J., Jing, Y. P., & White, S. D. M. 1996, , 282, 1096

Mohammad, F. et al. 2017, in preparation

Navarro, J. F., Frenk, C. S., & White, S. D. M. 1997, , 490, 493

Norberg, P., Baugh, C. M., Gaztañaga, E., & Croton, D. J. 2009, , 396, 19

Okumura, T. & Jing, Y. P. 2011, , 726, 5

Oort, J. H. 1932, , 6, 249

Peacock, J. A., Cole, S., Norberg, P., et al. 2001, , 410, 169

Peacock, J. A. & Dodds, S. J. 1994, , 267, 1020

Peebles, P. J. E. 1980, The large-scale structure of the universe (Princeton University Press, 1980. 435 p.)

Penzias, A. A. & Wilson, R. W. 1965, , 142, 419

Percival, W. J., Ross, A. J., Sánchez, A. G., et al. 2014, , 439, 2531

Perenon, L., Marinoni, C., & Piazza, F. 2016

Perenon, L., Piazza, F., Marinoni, C., & Hui, L. 2015, JCAP, 1511, 029

Perlmutter, S., Aldering, G., Goldhaber, G., et al. 1999, , 517, 565

Piazza, F., Steigerwald, H., & Marinoni, C. 2014, JCAP, 1405, 043

Planck Collaboration, Ade, P. A. R., Aghanim, N., et al. 2015, ArXiv e-print: 1502.01589

Prada, F., Klypin, A., Yepes, G., Nuza, S. E., & Gottloeber, S. 2011, ArXiv e-prints

Reid, B. A., Samushia, L., White, M., et al. 2012, , 426, 2719

Reid, B. A., Seo, H.-J., Leauthaud, A., Tinker, J. L., & White, M. 2014, , 444, 476

Riebe, K., Partl, A. M., Enke, H., et al. 2013, Astronomische Nachrichten, 334, 691

Riess, A. G., Filippenko, A. V., Challis, P., et al. 1998, , 116, 1009

Ross, N. P., da Ângela, J., Shanks, T., et al. 2007, , 381, 573

Rota, S., Granett, B. R., Bel, J., et al. 2016, ArXiv e-print 1611.07044

Samushia, L., Percival, W. J., & Raccanelli, A. 2012, , 420, 2102

Samushia, L., Reid, B. A., White, M., et al. 2013, , 429, 1514

Sanchez, A. G., Scoccimarro, R., Crocce, M., et al. 2016, ArXiv e-prints

Saunders, W., Rowan-Robinson, M., & Lawrence, A. 1992, , 258, 134

Scoccimarro, R. 2004, , 70, 083007

Scoccimarro, R., Couchman, H. M. P., & Frieman, J. A. 1999, , 517, 531

Scoccimarro, R. & Frieman, J. 1996, , 105, 37

Scodeggio, M., Franzetti, P., Garilli, B., Le Fèvre, O., & Guzzo, L. 2009, The Messenger, 135, 13

Scodeggio, M., Franzetti, P., Garilli, B., et al. 2005, , 117, 1284

Scodeggio, M., Guzzo, L., Garilli, B., et al. 2016, ArXiv e-print 1611.07048

Smith, R. E., Peacock, J. A., Jenkins, A., et al. 2003, , 341, 1311

Takahashi, R., Sato, M., Nishimichi, T., Taruya, A., & Oguri, M. 2012, , 761, 152

Taruya, A. & Hiramatsu, T. 2008, , 674, 617

Taruya, A., Nishimichi, T., & Saito, S. 2010, , 82, 063522

Taruya, A., Nishimichi, T., Saito, S., & Hiramatsu, T. 2009, , 80, 123503

Uhlemann, C., Kopp, M., & Haugg, T. 2015, , 92, 063004

Vargas-Magaña, M., Bautista, J. E., Hamilton, J.-C., et al. 2013, , 554, A131

Weinberg, D., Bard, D., Dawson, K., et al. 2013, ArXiv e-prints

Weinberg, S. 1993, 224

White, M., Blanton, M., Bolton, A., et al. 2011, , 728, 126

Wilson, M. et al. 2017, in preparation

Yang, X., Mo, H. J., van den Bosch, F. C., Zhang, Y., & Han, J. 2012, , 752, 41

York, D. G., Adelman, J., Anderson, J. J. E., et al. 2000, , 120, 1579

Zehavi, I., Weinberg, D. H., Zheng, Z., et al. 2004, , 608, 16

Zhang, P., Liguori, M., Bean, R., & Dodelson, S. 2007, Physical Review Letters, 99, 141302

Zwicky, F. 1933, Helvetica Physica Acta, 6, 110